UPPSALA
UNIVERSITET

*Digital Comprehensive Summaries of Uppsala Dissertations*
*from the Faculty of Science and Technology* 1729

# Theoretical and Computational Studies of Strongly Correlated Electron Systems

## *Dynamical Mean Field Theory, X-ray Absorption Spectroscopy and Analytical Continuation*

JOHAN SCHÖTT

ACTA
UNIVERSITATIS
UPSALIENSIS
UPPSALA
2018

ISSN 1651-6214
ISBN 978-91-513-0471-7
urn:nbn:se:uu:diva-362834

Dissertation presented at Uppsala University to be publicly examined in Polhemsalen, Ångströmlaboratoriet, Lägerhyddsvägen 1, Uppsala, Friday, 30 November 2018 at 13:15 for the degree of Doctor of Philosophy. The examination will be conducted in English. Faculty examiner: Professor Tim Wehling (Institute for Theoretical Physics, University of Bremen).

**Abstract**

Schött, J. 2018. Theoretical and Computational Studies of Strongly Correlated Electron Systems. Dynamical Mean Field Theory, X-ray Absorption Spectroscopy and Analytical Continuation. *Digital Comprehensive Summaries of Uppsala Dissertations from the Faculty of Science and Technology* 1729. 112 pp. Uppala: Acta Universitatis Upsaliensis. ISBN 978-91-513-0471-7.

This thesis encompasses theoretical and computational studies of strongly correlated electron systems. Understanding how electrons in solids interact with each other is of great importance for future technology and other applications. From a fundamental point of view, the Coulomb interaction in a solid leads to a very challenging many-body problem, encapsulating many physical phenomena, e.g. magnetism. Treating this interaction, with a focus on local contributions, is the subject of this thesis. Both models and materials have been investigated, to obtain insight on the mechanisms determining the macroscopic properties of matter. This thesis is divided in four parts, each corresponding to a different project or topic.

In the first project a many body method called dynamical mean field theory (DMFT) is used to study the paramagnetic phase of the Hubbard model. A stochastic version of the exact diagonalization technique is developed for solving the effective impurity model arising in DMFT and generating real frequency spectral functions. In the next project, by combining density functional theory (DFT) with a static solution of the DMFT equations (DFT+$U$), magnetic exchange interactions in transition metal oxides (TMOs) are investigated. The spin dependence of the functional is shown to be important for mapping magnetic excitations form the quantum mechanical system to a classical model.

The next topic in this thesis concerns the x-ray absorption spectroscopy of TMOs. Spectral functions, in good agreement with experimental data, are calculated by combining DFT with multiplet ligand field theory (MLFT). The effects of the presence of a core-hole are studied in detail for NiO, as well as double counting issues related to higher order terms of the multiple expansion of the Coulomb interaction. A strained induced linearly polarized spectrum is obtained for $CaTiO_3$. Lastly, charge disproportionation is seen in Mo doped $LaFeO_3$.

Finally, a critical step in DMFT, called analytical continuation, to obtain physical observables of interest is investigated. Analytical continuation means a transformation of a function in the complex plane. Several methods for performing this transformation are explained, and in particular steps for improving the robustness and accuracy of the Padé approximant method are described.

*Johan Schött, Department of Physics and Astronomy, Materials Theory, Box 516, Uppsala University, SE-751 20 Uppsala, Sweden.*

© Johan Schött 2018

ISSN 1651-6214
ISBN 978-91-513-0471-7
urn:nbn:se:uu:diva-362834 (http://urn.kb.se/resolve?urn=urn:nbn:se:uu:diva-362834)

# List of papers

This thesis is based on the following papers, which are referred to in the text by their Roman numerals.

I **Signatures of coherent electronic quasiparticles in the paramagnetic Mott insulator**
M. Granath and J. Schött
*Phys. Rev. B* ***90****, 235129 (2014)*

II **Electronic structure, magnetism, and exchange integrals in transition-metal oxides: Role of the spin polarization of the functional in DFT+$U$ calculations**
S. Keshavarz, J. Schött, A. Millis, and Y. Kvashnin
*Phys. Rev. B* ***97****, 184404 (2018)*

III **Theory of $L$-edge spectroscopy of strongly correlated systems**
J. Lüder, J. Schött, B. Brena, M. Haverkort, P. Thunström, O. Eriksson, B. Sanyal, I. Di Marco, and Y. Kvashnin
*Phys. Rev. B* ***96****, 245131 (2017)*

IV **Doping induced site-selective Mott insulating phase in LaFeO$_3$**
S. Jana, S. K. Panda, D. Phuyal, B. Pal, A. Dutta, P. Anil Kumar, D. Hedlund, J. Schött, P. Thunström, Y. Kvashnin, H. Rensmo, M. Venkata Kamalakar, P. Svedlindh, K. Gunnarsson, S. Biermann, O. Eriksson, O. Karis, and D. D. Sarma
*Submitted to Nature Communications*

V **Analytic continuation by averaging Padé approximants**
J. Schött, I. L. M. Locht, E. Lundin, O. Grånäs, O. Eriksson, and I. Di Marco
*Phys. Rev. B* ***93****, 075104 (2016)*

VI **A comparision between methods of analytical continuation for bosonic functions**
J. Schött, E. G. C. P. van Loon, I. L. M. Locht, M. I. Katsnelson, and I. Di Marco
*Phys. Rev. B* ***94****, 245140 (2016)*

VII **A GPU code for analytic continuation through a sampling method**
J. Nordström, J. Schött, I. Locht, and I. Di Marco
*SoftwareX 5, 178-182 (2016)*

Reprints were made with permission from the publishers.

## Additional publications

Papers not included in this thesis:

- **A charge self-consistent LDA+DMFT study of the spectral properties of hexagonal NiS**
  S. K. Panda, P. Thunström, I. Di Marco, J. Schött, A. Delin, I. Dasgupta, O. Eriksson, and D. D. Sarma
  *New Journal of Physics 16 , 093049 (2014)*

## The author's contributions to the publications

In all the papers listed above, I participated in discussions and contributed to the writing process. In paper I, I performed the quantum Monte Carlo (QMC) calculations, parallelized the distributional exact diagonalization (DED) program and did many of the simulations. In paper II, I contributed primarily in the data analysis. In paper III, I continued the project started by J. Lüder and had the main responsibility of writing the paper. I improved and generalized the original approach, including developments of the discretizing of the hybridization function. I also performed all calculations included in the final manuscript. In paper IV, I did the x-ray absorption spectroscopy (XAS) calculations using the combined approach of density functional theory (DFT) and multiplet ligand field theory (MLFT) established in paper III. In paper V, I did the method development, the code implementation, most of the data analysis, and was main responsible of writing the paper. In paper VI, I did most calculations, the implementation of the analytical continuation methods maximum entropy method (MEM) and Tikhonov regularization, and had the main responsibility of writing the paper. In paper VII, I guided a Bachelor student in the graphics processing unit (GPU) implementation of the stochastic optimization method (SOM) for analytical continuation, and participated in analyzing the results and writing the paper.

# Contents

1 Introduction 7
  1.1 Ab initio electronic structure 9
    1.1.1 Bloch theorem 10
    1.1.2 Density functional theory 10
  1.2 Hubbard model 13
    1.2.1 Atomic and non-interacting limits 14
    1.2.2 Beyond density functional theory 16
  1.3 Green's functions 16
    1.3.1 Two operator propagator 16
    1.3.2 Single-particle Green's function 20

2 Dynamical mean field theory 23
  2.1 Single impurity Anderson model 23
  2.2 Self-consistency conditions 25
  2.3 Bethe lattice 26
  2.4 Distributional exact diagonalization 26
  2.5 DFT+DMFT 30
    2.5.1 Projection to localized basis 31
    2.5.2 Coulomb expansion 32
    2.5.3 Double counting 34
    2.5.4 Charge self consistency 34
    2.5.5 DFT+$U$ 35
    2.5.6 Exchange integrals 36
  2.6 Exchange integrals using L(S)DA+U of transition metal oxides 37

3 X-ray absorption spectroscopy 40
  3.1 Dipole transition operator 41
  3.2 Green's function 45
  3.3 Transition metal oxides: MnO, FeO, CoO and NiO 46
  3.4 Atomic-plane resolution of strained $CaTiO_3$ 53
  3.5 Mo doped $LaFeO_3$ 57

4 Analytical continuation 58
  4.1 Fredholm equation 59
    4.1.1 Kernels 60
    4.1.2 Imaginary frequency 60
    4.1.3 Imaginary time 61
    4.1.4 Legendre polynomials 62

4.1.5 Complex decomposition ... 63
4.2 Least squares ... 63
4.3 SVD and Tikhonov regularization ... 67
4.3.1 SVD ... 67
4.3.2 Condition number ... 68
4.3.3 Truncated SVD ... 69
4.3.4 Tikhonov regularization ... 69
4.4 Maximum entropy method ... 71
4.5 Stochastic optimization method ... 74
4.6 Padé approximants ... 77
4.6.1 Thiele's reciprocal difference method ... 77
4.6.2 Square matrix formulation ... 78
4.6.3 Zero-pole pairs ... 79
4.6.4 LS Padé ... 80
4.6.5 Averaging ... 81
4.6.6 Mirror symmetry ... 81
4.6.7 Inversion precision ... 83
4.6.8 Summary of method development ... 84
4.7 A comparision between methods for bosonic functions ... 84
4.8 Correlation ... 85
4.8.1 Binning analysis ... 85
4.8.2 Covariance matrix ... 86

5 Summary and outlook ... 89

6 Populärvetenskaplig sammanfattning ... 91

7 Acknowledgements ... 93

Appendices ... 94

A Matsubara summation ... 95

B Lanczos algorithm ... 97

References ... 99

# 1. Introduction

Technology and material design have been very important for the global development. For instance, since the industrial revolution about 200 years ago the number of people living in extreme poverty has dropped from 85% to 9% [1–3], permanent magnets have allowed us to transform mechanical and electrical energy, and in recent decades both the total global information storage and the transistor density in computers have doubled in less than every second year [4, 5]. But despite these and other remarkable achievements, new advances in material science are necessary in order to sustainably exploit the earth's limited resources and at the same time facilitate a high standard of living for everyone [6–8]. One pressing issue in materials science is that the size of transistors is approaching a length scale of a few nano meters ($10^{-9}$ m), prohibiting the impressive development mentioned above to continue. The problem is that classical mechanics is not applicable at these length scales. In this domain, quantum mechanics, introduced in the 20th century, dictates the rules of nature. Hence, for smaller transistors and more efficient electronics, we need to master the laws of quantum physics. In general, an important goal in material science is to be able to predict properties of solids from the basic rules of quantum mechanics. However, even though the equations governing the behaviour of the electrons are known, solving them is hard. Approximate theoretical methods exist for solving these equations numerically, exploiting the large computational power of todays supercomputers. Thus, simulations allow us to understand materials, predict their properties and find new materials. In many materials, these approximate and computationally fast methods are accurate enough to describe and predict the reality. The perhaps most successful theoretical method is the Nobel prize awarded density functional theory (DFT) [9, 10]. Nevertheless, for a group of materials, where the electrons interact strongly with each other, DFT fails. This PhD thesis deals with understanding and modeling the physics of strongly correlated electron systems. The latter show a vast amount of remarkable phenomena, including superconductivity, magnetism and metal to insulator transitions. This rich physics may be utilized in many future technological applications, e.g. for improving energy efficiency [11]. There are many methods to describe strongly correlated systems. This thesis is focused on the combination of approximate ab initio electronic structure methods, such as DFT, with model Hamiltonian methods, such as dynamical mean field theory (DMFT).

The thesis is organized as follows:

**Chapter 1**: The ab initio electronic structure problem is discussed, focusing on how to approximately solve the problem within a single particle approach. The introduction chapter also introduces the Hubbard model Hamiltonian, which incorporates the important local electronic interaction, as well as Green's function formalism, which will be useful in the later chapters.

**Chapter 2**: In this chapter DMFT is presented, which is a method for solving the Hubbard model in a many body fashion. A crucial step in DMFT is the solution of an effective impurity problem. A stochastic method called distributional exact diagonalization (DED) is presented in section 2.4 and applied in paper I for the insulating phase of the Hubbard model on the Bethe lattice. Section 2.5.6 and paper II discuss magnetic exchange between atomic spins in various transition metal oxides (TMOs). In particular, the role of the spin polarization of the DFT functional is analyzed, as well as the mapping of the electronic structure to a effective classical Heisenberg model.

**Chapter 3**: Theory of x-ray absorption spectroscopy (XAS) and simulated results of several TMOs, which stem from three separate projects, are contained in this chapter. In the first project the methodology for calculating $L$-edge x-ray absorption (XA) spectra is established and applied to MnO, FeO, CoO and NiO. This work was published in paper III. The second project is about atomic-plane resolution of Ti $L$-edges. Calculations show that strain induces a linear polarization dependence, which results in changes in the $L$-edge line shapes as a function of spatial coordinates on an atomic scale. Experimentally, one can obtain this atomic plane information by measuring the electron energy loss spectroscopy (EELS) signal. The third project presented in this chapter, and in paper IV, is about Mo doped $LaFeO_3$, which shows interesting coexistence of metallicity, anti-ferromagnetism and charge disproportionation. To see if we could verify the experimental findings, Fe $L$-edges were calculated for two different doping concentrations. This chapter ends with a section describing the on-going project on the development of projecting the momentum dependent representation of the XAS dipole transition operator, and how it can be generalized beyond the dipole approximation.

**Chapter 4**: The problem of analytical continuation is discussed in this chapter. In finite temperature Green's function formalism one employs imaginary times and energies. Analytical continuation becomes necessary to transform observables from imaginary variables to the physically relevant real variables. Several different methods for performing analytical continuation are introduced and results from papers V,VI and VII are discussed.

**Chapter 5**: Short summaries and outlooks of the papers are contained in this chapter.

## 1.1 Ab initio electronic structure

For studying electrons in condensed matter physics, it is common to treat the much heavier nuclei as stationary [12]. Using this Born-Oppenheimer approximation the non-relativistic many-body Hamiltonian operator for $N$ electrons is in first quantization

$$\tilde{H} = \sum_{i=1}^{N} \left( -\frac{1}{2}\tilde{\nabla}_i^2 + V_{\text{ext.}}(\tilde{\boldsymbol{r}}_i) \right) + \sum_{i=1}^{N} \sum_{j>i}^{N} \frac{1}{|\tilde{\boldsymbol{r}}_i - \tilde{\boldsymbol{r}}_j|}, \tag{1.1}$$

where the external potential from the assumed stationary nuclei at positions $\boldsymbol{R}_k$ and atomic numbers $Z_k$ is given by

$$V_{\text{ext.}}(\tilde{\boldsymbol{r}}) = -\sum_k \frac{Z_k}{|\boldsymbol{R}_k - \tilde{\boldsymbol{r}}|}, \tag{1.2}$$

with $k$ running over all atomic nuclei. Hartree atomic units are used throughout the thesis unless explicitly said otherwise, thus $\hbar = m_e = e = 1$. Operators in first (second) quantization are indicated by a $\tilde{}$ ($\hat{}$) on top of the variable. The time-independent Schrödinger equation

$$\tilde{H}|\Psi\rangle = E|\Psi\rangle \tag{1.3}$$

contains all information necessary to calculate every property of the electrons. In Eq. (1.3), $\Psi(\boldsymbol{r}_1, \boldsymbol{r}_2, \boldsymbol{r}_3, ..., \boldsymbol{r}_N)$ is the many electron wave function and $E$ its corresponding energy. Solving the Schrödinger Eq. (1.3) for the Hamiltonian in Eq. (1.1) is a great challenge because of the exponential growth of the Hilbert space with the number of particles $N$ [13]. Typically a finite single particle basis set is chosen when treating Eq. (1.1). Let us denote these functions with indices $(i, \sigma)$, where $i$ labels the orbital character of the wavefunction $\psi_{i,\sigma}$, and let $L$ be the number of basis functions. This allows us to write the Hamiltonian operator in Eq. (1.1) in second quantization notation as [13–15]

$$\hat{H} = \sum_{ij,\sigma} t_{ij} \hat{c}_{i,\sigma}^{\dagger} \hat{c}_{j,\sigma} + \frac{1}{2} \sum_{ijkl,\sigma\sigma'} U_{ijkl} \hat{c}_{i,\sigma}^{\dagger} \hat{c}_{j,\sigma'}^{\dagger} \hat{c}_{k,\sigma'} \hat{c}_{l,\sigma}, \tag{1.4}$$

where the $\hat{c}_{i,\sigma}$ operator annihilates an electron with spin $\sigma$ from orbital $\psi_i$. For orthonormal basis functions, the operator $\hat{c}_{i,\sigma}^{\dagger}$ creates an electron with spin $\sigma$ at orbital $\psi_i$ [13]. The matrix elements are given by integrals over the basis functions together with the single- and two-particle Hamiltonian terms respec-

$$U_{ijkl}\hat{c}^{\dagger}_{i,\sigma}\hat{c}^{\dagger}_{j,\sigma'}\hat{c}_{k,\sigma'}\hat{c}_{l,\sigma} =$$

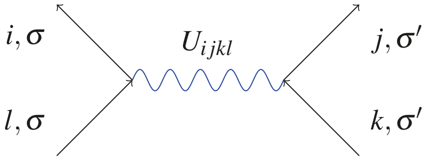

*Figure 1.1.* Feynman diagram of the Coulomb interaction.

tively:

$$t_{ij} = \int d^3r \psi_i^*(\boldsymbol{r}) \left(-\frac{1}{2}\nabla^2 + V_{\text{ext.}}(\boldsymbol{r})\right) \psi_j(\boldsymbol{r}) \tag{1.5}$$

$$U_{ijkl} = \int\int d^3r d^3r' \psi_i^*(\boldsymbol{r})\psi_j^*(\boldsymbol{r}') \frac{1}{|\boldsymbol{r}-\boldsymbol{r}'|} \psi_k(\boldsymbol{r}')\psi_l(\boldsymbol{r}). \tag{1.6}$$

The $t_{ij}$ can be thought of as a hopping magnitude between the basis orbital functions and the electron-electron interaction can be visualized with a Feynman diagram, see Fig. 1.1.

### 1.1.1 Bloch theorem

Finding the groundstate energy of Eq. (1.4) is in general not possible. However, there are strategies and cases where it is possible. If the electron-electron interaction in the system of interest is very weak ($U \approx 0$) the electrons are independent of each other and the problem reduces to a single-particle problem with hopping $t_{ij}$. For a periodic crystal the eigenstates are single particle Bloch functions $\phi_{\boldsymbol{k},n,\sigma}(\boldsymbol{r}) = e^{i\boldsymbol{k}\cdot\boldsymbol{r}}u_{n,\boldsymbol{k}}(\boldsymbol{r})$ with quantum numbers $\boldsymbol{k}$, $n$, $\sigma$ for respectively lattice momentum, band-index and spin [16]. The non-interacting Hamiltonian in this representation is diagonal:

$$\hat{H} = \sum_{\boldsymbol{k},n,\sigma} \varepsilon_{\boldsymbol{k},n,\sigma}\hat{n}_{\boldsymbol{k},n,\sigma}, \tag{1.7}$$

where $\hat{n}_{\boldsymbol{k},n,\sigma} = \hat{c}^{\dagger}_{\boldsymbol{k},n,\sigma}\hat{c}_{\boldsymbol{k},n,\sigma}$ is the occupation operator and $\varepsilon_{\boldsymbol{k},n,\sigma}$ the band energy. Due to the lattice periodicity of the function $u(\boldsymbol{r})$ the solution can be obtained and studied inside only one primitive lattice cell, which greatly simplifies the calculations. Note that certain phenomena, e.g. magnetism, can reduce the symmetry in the system and hence require a bigger unit cell than the primitive lattice cell [17].

### 1.1.2 Density functional theory

When interaction is present, famous approximations can be formulated for solving the many-body problem in Eq. (1.4), by mapping it to a single-particle problem with an effective potential. Both the Hartree-Fock (HF) method and DFT belong to this category. In the HF approximation one assumes independent electrons, by making an ansatz on the many-body wave function to be a single Slater determinant, which is then used to minimize the total energy.

In principle DFT is an exact theory for ground state properties [9]. The key idea is to describe the ground state in terms of the charge density instead of the many body wave function. Kohn and Sham showed [10] how to find the ground state density by working with an auxiliary non-interacting system of particles, having the same charge density $n(\boldsymbol{r})$ as the system with interacting electrons. The Kohn-Sham Hamiltonian and the corresponding eigenvalue problem for these quasiparticles are

$$\tilde{H}_{\text{KS}} = -\frac{1}{2}\tilde{\nabla}^2 + V_{\text{ext.}}(\tilde{\boldsymbol{r}}) + \int d^3r' \frac{n(\boldsymbol{r}')}{|\tilde{\boldsymbol{r}}-\boldsymbol{r}'|} + \frac{\delta E_{\text{xc}}[n]}{\delta n(\tilde{\boldsymbol{r}})} \tag{1.8}$$

$$\tilde{H}_{\text{KS}}|\phi\rangle = \varepsilon|\phi\rangle. \tag{1.9}$$

In Eq. (1.8) the first term is the kinetic energy of non-interacting electrons, the second the external potential from the nuclei, the third the Hartree potential (which is the classical electrostatic term) and the forth is the exchange-correlation term (which is unknown and has to be approximated). $\langle\boldsymbol{r}|\phi\rangle$ is the single-particle Kohn-Sham eigenstate wavefunction, with the corresponding eigenenergy $\varepsilon$. After choosing an appropriate single-particle basis, $\{|\psi\rangle\}$, the hopping matrix reads

$$t_{ij}^{KS} = \int d^3r \psi_i^*(\boldsymbol{r}) H_{\text{KS}} \psi_j(\boldsymbol{r}). \tag{1.10}$$

Notice the similarity to Eq. (1.5). By expanding the eigenstates in this basis, i.e. $|\phi\rangle = \sum_i b_i|\psi_i\rangle$, Eq. (1.9) becomes a generalized eigenvalue problem:

$$\sum_j t_{ij}^{KS} b_j = \varepsilon \sum_j S_{ij} b_j, \tag{1.11}$$

with the overlap matrix $S_{ij} = \int dr^3 \psi_i^*(\boldsymbol{r})\psi_j(\boldsymbol{r})$ being the identity matrix in case of an orthonormal basis.

In a periodic lattice the Bloch theorem reduces the problem to a single unit cell and in the KS-eigenvalue basis the many-body Hamiltonian looks the same as Eq. (1.7). Nevertheless, the KS eigenenergies include the Hartree term and approximate exchange and correlation terms from the Coulomb interaction in a mean field fashion. Since the KS Hamiltonian depends on the charge density, which can be calculated from the KS wavefunctions, Eq. (1.9) has to be solved iteratively until the charge density is converged.

### Functionals

The drawback of DFT is that the unknown universal exchange-correlation functional must be approximated. The commonly used local density approximation (LDA) assumes that the functional solely depends on the value of the charge density at each point in space. This limits the applicability of DFT to weakly correlated systems where the density is almost homogeneous in space, such as normal metals, band insulators and semiconductors. But for strongly correlated systems, such as many compounds containing $3d$ transition metals, lanthanides or actinides, DFT fails in predicting the material properties [18]. One of the problems with the LDA functional (and many other approximate DFT functionals) is that the electron in an orbital interacts spuriously with its own charge density [19]. Another popular functional worth mentioning is called the generalized gradient approximation (GGA), which takes into account not only the density at a given point, but also its gradient. This offers a way to include some effects associated to less homogenous densities, although many correlated materials are still insufficiently described. To study magnetism, spin polarized functionals have been developed, such as the local spin density approximation (LSDA) [20].

**DFT basis**

The choice of basis functions matters and the number of orbitals in the basis should be kept as low as possible for computational reasons but big enough for accurate calculations. The shape of the orbitals preferably should be tailored to the system of study, e.g. plane waves for free electron like systems and atomic centered orbitals for molecules and atoms. For electrons in a solid neither of these two basis types are ideal since some electrons are localized, some are delocalized and some are something in between. This is why more complicated basis sets are often used for solids. Another approach is to not treat all electrons, by replacing inner fully localized shells with a pseudo-potential and simulate only the valence electrons with e.g. a plane wave basis.

In papers II, III and IV we have used the Relativistic Spin Polarized Toolkit (RSPt) code [21] which is an all-electron full-potential linear muffin-tin orbital (FP-LMTO) method [22, 23]. In this method, the space is divided into two regions, spheres around the atoms and the interstitial space between these spheres. This division is motivated by the observation that the potential close to the nuclei is almost spherical, while far away the potential is almost flat. The LMTO basis consists of solutions to the Schrödinger equation with a spherical potential inside the muffin-tin (MT) spheres, augmented with free electron solutions expressed in radial coordinates (i.e. Bessel and Neumann functions) in the interstitial region. At the boundary of the MT sphere the two solutions are matched by smoothness conditions. The radial part of the basis functions inside the MT sphere depend on the energy, $f = f(r,\varepsilon)$, and for computational efficiency a linearizing Taylor expansion is used around a given energy $\varepsilon_\nu$, thus $f(r,\varepsilon) \approx f(r,\varepsilon_\nu) + \frac{\partial f}{\partial \varepsilon}(r,\varepsilon_\nu)(\varepsilon - \varepsilon_\nu)$. Since the basis functions are solutions to the Schrödinger equation and depend on the potential, their shapes are modified during charge self-consistency. Fig. 1.2 shows basis functions inside the MT in NiO, at the beginning (having an atomic density) and at the end of the DFT self-consistency cycle. Two advantages with this DFT basis are its

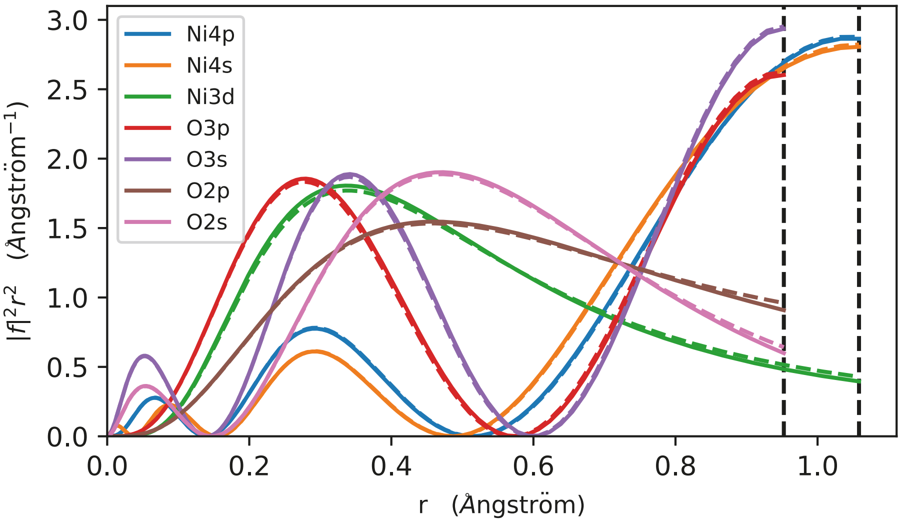

*Figure 1.2.* Radial part of the RSPt basis functions inside the MT spheres for NiO. Notice that oxygen and nickel have different MT radii. The solid (dashed) lines represent basis functions for a converged (atomic) charge density. Normalization is such that $\int |f(r)|^2 r^2 dr = 1$.

compactness and that no approximation of the potential is needed. However, compared to e.g. the linearized augmented plane wave (LAPW) method, with the LMTO basis it is hard to systematically increase the number of basis functions to check if sufficient completeness has been obtained. Actually, the most commonly used DFT codes of today give very similar results, at least for the equation of state of many elemental crystals [24]. For more information about the RSPt basis, please see Refs. [17, 22, 25–29].

## 1.2 Hubbard model

To model a solid where electrons experience a strong Coulomb interaction, Hubbard proposed a simple model which today is known as the Hubbard model [30]. It captures the competing processes of delocalization, favoured by the hopping term $t$, and localization, induced by the electron-electron interaction $U$. Starting either directly from the Schrödinger equation or from DFT, a few approximations lead to the Hubbard model and will be outlined here. The difference between the two starting points is what is included in the hopping term, either one uses Eq. (1.5) or Eq. (1.10). In the latter case a double counting term is also needed, as described in section 2.5.3.

The Hubbard model is used to study localized $d$ or $f$ electrons. Let us use an atom centered orbital basis and introduce the orbital super index notation $i = \{\boldsymbol{R}_i, \boldsymbol{\tau}_i, a_i\}$, to denote unit cell, atom within unit cell, and atomic orbital index.

The index $a$ can for example include the angular momentum projected on the $z$-axis if the basis functions are expressed in terms of spherical harmonics. Of all interaction processes the intra-atomic ones are typically the strongest for systems with localized wavefunctions. Neglecting all inter atomic interactions means:

$$U_{ijkl} \approx \delta_{\boldsymbol{R}_i,\boldsymbol{R}_j,\boldsymbol{R}_k,\boldsymbol{R}_l} \delta_{\boldsymbol{\tau}_i,\boldsymbol{\tau}_j,\boldsymbol{\tau}_k,\boldsymbol{\tau}_l} U_{\boldsymbol{\tau},a_i a_j a_k a_l} \tag{1.12}$$

This approximation gives a multi-band Hubbard model, namely

$$\begin{aligned} \hat{H} = & \sum_{i,j,\sigma} t_{i,j} \hat{c}^{\dagger}_{i,\sigma} \hat{c}_{j,\sigma} \\ & + \frac{1}{2} \sum_{\substack{\boldsymbol{R},\boldsymbol{\tau},\sigma\sigma' \\ a_i a_j a_k a_l}} U_{\boldsymbol{\tau},a_i a_j a_k a_l} \hat{c}^{\dagger}_{\boldsymbol{R},\boldsymbol{\tau},a_i,\sigma} \hat{c}^{\dagger}_{\boldsymbol{R},\boldsymbol{\tau},a_j,\sigma'} \hat{c}_{\boldsymbol{R},\boldsymbol{\tau},a_k,\sigma'} \hat{c}_{\boldsymbol{R},\boldsymbol{\tau},a_l,\sigma}, \end{aligned} \tag{1.13}$$

where no restriction is done on the hopping. To illustrate the physical meaning of this model we will perform a few further simplifications. Let us assume the studied system only has one atom per unit cell and consider a basis with only one orbital per atomic site. With these great simplifications, the original problem has been reduced to a single-band model and the indices $\boldsymbol{\tau}$ and $a$ can be dropped. The interaction is then intra-orbital and is usually denoted as $U = U_{iiii}$. Rewriting the creation and annihilation operators into occupation operators and excluding processes removing two electrons from the same state, the interaction term simplifies to $U \sum_{\boldsymbol{R}} \hat{n}_{\boldsymbol{R},\uparrow} \hat{n}_{\boldsymbol{R},\downarrow}$. For localized orbitals the hopping $t_{ij} = t_{\boldsymbol{R}\boldsymbol{R}'}$ is approximately either within the same unit cell or to the nearest neighbours:

$$t_{\boldsymbol{R}\boldsymbol{R}'} \approx (\delta_{\boldsymbol{R},\boldsymbol{R}'} + \delta_{\langle \boldsymbol{R}\boldsymbol{R}' \rangle}) t_{\boldsymbol{R}\boldsymbol{R}'}, \tag{1.14}$$

where $\langle\ \rangle$ means nearest neighbours. The local hopping is reduced to counting the number of electrons and can be treated as a part of the chemical potential. Let us also assume hopping is the same to all nearest neighbours. The single-band Hubbard model thus reads

$$\hat{H} = -t \sum_{\langle \boldsymbol{R}\boldsymbol{R}' \rangle,\sigma} (\hat{c}^{\dagger}_{\boldsymbol{R}\sigma} \hat{c}_{\boldsymbol{R}'\sigma} + \hat{c}^{\dagger}_{\boldsymbol{R}'\sigma} \hat{c}_{\boldsymbol{R}\sigma}) + U \sum_{\boldsymbol{R}} \hat{n}_{\boldsymbol{R},\uparrow} \hat{n}_{\boldsymbol{R},\downarrow}, \tag{1.15}$$

with hopping parameter $t = -\delta_{\langle \boldsymbol{R}\boldsymbol{R}' \rangle} t_{\boldsymbol{R}\boldsymbol{R}'}$. This problem is much easier to solve than the original problem but still captures the competition between the hopping (favoring delocalization) and the local Coulomb interaction (favoring localization), which is behind many important phenomena, such as the Mott metal to insulator transition. In Chapter 2 we will solve Eq. (1.15) using DMFT. Fig. 1.3 illustrates the Hubbard model on a square lattice.

### 1.2.1 Atomic and non-interacting limits

Here we briefly discuss two important limits of the single orbital Hubbard model in Eq. (1.15). In the limit of no interaction ($U \to 0$), the eigenstates are

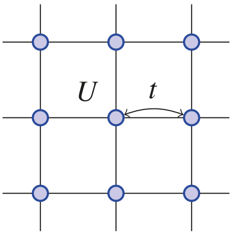

*Figure 1.3.* The Hubbard model on a square lattice with hopping parameter $t$ and local interaction parameter $U$.

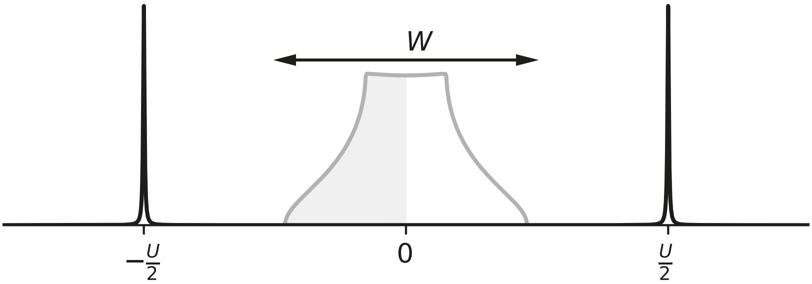

*Figure 1.4.* Schematic picture of the atomic (black) and non-interacting (grey) spectral function of the single-band Hubbard model at half-filling. A cubic lattice geometry is used in the non-interacting case. Figure inspired by [31].

delocalized Bloch waves with eigenenergies $\varepsilon_{\boldsymbol{k}} = -t\sum_{\langle \boldsymbol{R},\boldsymbol{0}\rangle} e^{-i\boldsymbol{k}\cdot\boldsymbol{R}}$ (obtained by Fourier transforming the hopping term). The width, $W$, of the band is proportional to the hopping strength $t$ and the system is metallic for any site occupation between 0 and 2. In Fig. 1.4 the density of states, $\rho(\omega) = \sum_{\boldsymbol{k}} \delta(\omega - \varepsilon_{\boldsymbol{k}})$, is shown (grey line) for a system of cubic lattice geometry at half filling.

In the atomic limit the hopping goes to zero ($t \to 0$). From bandpicture one might then expect to have a narrow band and metallic behavior at partial occupation. However, the $U$ term dominates in the atomic limit and favors localization, i.e. the four Fock states of a single site, $|0\rangle, |\uparrow\rangle, |\downarrow\rangle$ and $|\uparrow\downarrow\rangle$, are eigenstates. Corresponding discrete eigenenergies are 0, $\mu$, $\mu$ and $U + 2\mu$, respectively, where the chemical potential $\mu$ for a half-filled system is $-U/2$. This results in an insulating spectral function (a definition of the spectral function is given in section 1.3) with peaks at $\pm U/2$, see the black line in Fig. 1.4. The double occupancy $\langle \hat{n}_\uparrow \hat{n}_\downarrow \rangle = 0$ ($\neq \langle \hat{n}_\uparrow \rangle \langle \hat{n}_\downarrow \rangle = \frac{1}{2}\frac{1}{2}$), indicates that correlations are present. A Mott transition is an interaction driven phase transition between a metal and an insulator, and occurs roughly when $U \approx W$.

### 1.2.2 Beyond density functional theory

Due to the failure of DFT to describe partially occupied localized states (many $3d$, $4d$, $5d$, $4f$ and $5f$ systems), a popular strategy is to improve upon the KS system, by using it as a starting point and adding the local intra atomic Coulomb interaction from the Hubbard model for a subset of all the orbitals in the system, e.g. only the $3d$ orbitals. This is preferable compared to starting from the Schrödinger Eq. (1.4) and approximating the Coulomb interaction to be local, as in the Hamiltonian in Eq. (1.13). This can be understood by the fact that this would cut away much of the long-ranged interaction, such as the Hartree interaction. Instead, using the KS system as a starting point the Hartree interaction is included in the hopping $t_{ij}^{\mathrm{KS}}$. Two such approaches are DFT+U [32–38] and DFT+DMFT [15, 39–42], where the former can be seen as a static approximation to the latter. Due to its simplicity and computational speed, DFT+$U$ has been used for many insulating systems where pure DFT fails. In paper II and section 2.5.6 DFT+U is used to study various insulating $3d$ systems, and comparing the LDA functional with the LSDA functional. In Chapter 3 a simplified DFT+DMFT approach is used to study x-ray absorption spectroscopy of strongly correlated systems.

## 1.3 Green's functions

Green's functions are mathematical tools for solving differential equations. However in many-body theory Green's functions act as propagators and are sometimes also referred to as correlation functions. They are defined as time dependent expectation values of products of operators. There are many different flavours of Green's functions and one can find various relations among them. A short overview will be given here of some basic Green's function concepts but for a more complete description please consider the text-books [43–45].

### 1.3.1 Two operator propagator

The imaginary time two operator Green's function is defined in the Heisenberg picture as

$$G_{A,B}(\tau,\tau') = -\langle T_{\tau,\tau'}\hat{A}(\tau)\hat{B}(\tau')\rangle. \tag{1.16}$$

By choosing the operator $\hat{A}$ and $\hat{B}$ to be fermionic annihilation and creation operator respectively, $G$ is a fermionic one particle Green's function. For $\hat{A}$ and $\hat{B}$ each consisting of pairs of fermionic creation and annihilation operators, $G$ is a bosonic two particle Green's function, e.g. the charge-charge correlation function [45]. Imaginary time is introduced to formulate a finite temperature theory, and corresponds to substituting $it$ by $\tau$, where $i$ is the imaginary number and $t$ is the time. The operators as functions of imaginary time in the

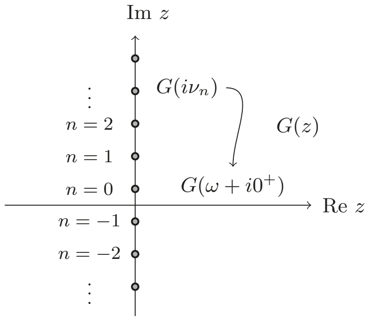

*Figure 1.5.* Analytical continuation in the complex plane from Matsubara frequencies $i\nu_n$ to points distanced $i0^+$ above the real axis.

Heisenberg picture are of the form $\hat{A}(\tau) = e^{\tau\hat{H}}\hat{A}e^{-\tau\hat{H}}$. The time ordering super operator $T$ in Eq. (1.25) reorders the operators by moving the later time to the left. If the Hamiltonian for the system does not explicitly depend on the time, the Green's function only depends on the relative time difference $\tau = \tau - \tau'$, which can easily be shown using the cyclic properties of the trace. The Green's function $G(\tau)$ is defined for $\tau \in (-\beta, \beta]$ and cyclic permutations inside the trace give an anti-periodic (periodic) property for fermionic (bosonic) fields

$$G(\tau) = \mp G(\tau + \beta) \tag{1.17}$$

for $-\beta < \tau < 0$ [46], where the upper (lower) sign is for fermions (bosons). The Green's function can formally be periodically repeated from $\tau \in (-\beta, \beta]$ and hence expressed by a Fourier series expansion

$$G(\tau) = \frac{1}{\beta} \sum_{n=-\infty}^{\infty} e^{-i\nu_n\tau} G_n \tag{1.18}$$

with Fourier coefficients

$$G_n = \frac{1}{2} \int_{-\beta}^{\beta} d\tau e^{i\nu_n\tau} G(\tau) \tag{1.19}$$

and $\nu_n = \frac{\pi n}{\beta}$. However, coefficients for even (odd) $n$ are zero due to the anti-periodicity (periodicity) in Eq. (1.17) for fermions (bosons) and the ones for odd (even) $n$ simplifies to

$$G_n = \int_{0}^{\beta} d\tau e^{i\nu_n\tau} G(\tau). \tag{1.20}$$

For an easier notation of the non-zero coefficients, we redefine $\nu_n$ as

$$\nu_n = (2n+1)\pi/\beta \text{ for fermions} \tag{1.21}$$
$$\nu_n = 2n\pi/\beta \text{ for bosons,} \tag{1.22}$$

with $n \in \mathbb{Z}$, and call them the fermionic and bosonic Matsubara frequencies respectively. The corresponding values in Eq. (1.20) are called the Matsubara Green's function. Given the set of infinitely many $G_n$ values, there exists a corresponding unique function $\rho$, called the spectral function, having the property:

$$G_n = \int_{-\infty}^{\infty} d\omega \frac{1}{i\nu_n - \omega} \rho(\omega). \tag{1.23}$$

This equation can be generalized by replacing the points on the imaginary axis in the complex plane, $i\nu_n$, by a general complex number $z$, hence

$$G(z) = \int_{\infty}^{\infty} d\omega \frac{1}{z - \omega} \rho(\omega). \tag{1.24}$$

Given a set of $G_n$, by solving Eq. (1.23) for $\rho$, $\rho$ can be used in Eq. (1.24) to calculate $G(z)$ in the upper and lower complex plane. On the real axis $G(z)$ has a branch cut with a discontinuity of $-2\pi i \rho(\omega)$. The unique mapping in the complex plane from $G(i\nu_n) = G_n$ to $G(z)$ is an example of analytical continuation, see Fig. 1.5. The proof of the uniqueness by Maym and Mermin [47] uses the Carleman's theorem [48]. How to numerically perform the analytical continuation is one of the main topics of this thesis and will be discussed in Chapter 4. The Green's function $G(\tau)$ can directly be related to the spectral function by using its Fourier representation, i.e. Eq. (1.18), together with Eq. (1.23). However, to reach a compact expression, a summation over the Matsubara points is needed, see Appendix A. Finally one gets

$$G(\tau) = \int_{-\infty}^{\infty} d\omega \frac{-e^{-\tau\omega}}{1 \pm e^{-\beta\omega}} \rho(\omega), \text{ for } 0 < \tau < \beta. \tag{1.25}$$

Analytical properties can be obtained by expressing the imaginary time Green's function in terms of all the (many-body) eigenstates of the system. For $0 < \tau < \beta$

$$\begin{aligned} G(\tau) &= -\frac{1}{Z} \mathrm{Tr}[e^{-\beta\hat{H}} e^{\tau\hat{H}} \hat{A} e^{-\tau\hat{H}} \hat{B}] && (1.26) \\ &= -\frac{1}{Z} \sum_n \langle n | e^{-\beta\hat{H}} e^{\tau\hat{H}} \hat{A} \underbrace{\hat{I}}_{\sum_m |m\rangle\langle m|} e^{-\tau\hat{H}} \hat{B} | n \rangle && (1.27) \\ &= -\frac{1}{Z} \sum_{n,m} e^{-\beta E_n} \langle n | \hat{A} | m \rangle \langle m | \hat{B} | n \rangle e^{\tau(E_n - E_m)}, && (1.28) \end{aligned}$$

where $Z = \sum_n e^{-\beta E_n}$ is the partition function and $E_n$ is the eigenenergy for the eigenstate $|n\rangle$. By Fourier transforming Eq. (1.28) and replacing $i\nu_n \to z$ we get

$$G(z) = \frac{1}{Z} \sum_n \sum_m (e^{-\beta E_n} \pm e^{-\beta E_m}) \langle n | \hat{A} | m \rangle \langle m | \hat{B} | n \rangle \frac{1}{z - (E_m - E_n)}. \tag{1.29}$$

The Lehmann representation of the spectral function

$$\rho(\omega) = \frac{1}{Z}\sum_{n,m}(e^{-\beta E_n} \pm e^{-\beta E_m})\langle n|\hat{A}|m\rangle\langle m|\hat{B}|n\rangle\delta(\omega - (E_m - E_n)), \qquad (1.30)$$

corresponds to Eq. (1.29) by satisfying Eq. (1.24) together with the uniqueness property.

**Common operator case: $\hat{A} = \hat{B}^\dagger$**

Note that the spectral function in general is complex valued, but if $\hat{A} = \hat{B}^\dagger$, we get:

$$\rho(\omega) = \frac{1}{Z}\sum_{n,m}(e^{-\beta E_n} \pm e^{-\beta E_m})|\langle m|\hat{B}|n\rangle|^2\delta(\omega - (E_m - E_n)) \qquad (1.31)$$

which is clearly a real quantity and obeys the relations

$$\rho(\omega) \geq 0\ , \text{ for fermions} \qquad (1.32)$$

$$\rho(\omega)/\omega \geq 0\ , \text{ for bosons.} \qquad (1.33)$$

Also, the imaginary part of the Green's function evaluated just above the real axis is actually directly related to the spectral function. This is easily seen from Eq. (1.24) and by exploiting the fact $\rho \in \mathbb{R}$. We get

$$\mathrm{Im}[G(\omega + i\delta)] = \int_{-\infty}^{\infty} d\omega' \frac{-\delta}{(\omega - \omega')^2 + \delta^2}\rho(\omega') \underset{\delta \to 0^+}{\to} -\pi\rho(\omega). \qquad (1.34)$$

The Green's function evaluated in the limit of $\delta \to 0^+$ is called the retarded Green's function. Let us define it as $G^{\mathrm{ret}}(\omega) = G(\omega + i0^+)$. Hence

$$\rho(\omega) = -\frac{1}{\pi}\mathrm{Im}[G^{\mathrm{ret}}(\omega)] = -\frac{1}{\pi}\mathrm{Im}[G(\omega + i0^+)]. \qquad (1.35)$$

There exists an important mirror symmetry for the Green's function, namely

$$G(z) = G(z^*)^* \qquad (1.36)$$

which can be obtained from Eq. (1.24) and by using $\rho \in \mathbb{R}$. For one of the analytical continuation methods, the Padé approximant method, discussed in section 4.6, explicitly enforcing this mirror symmetry of the Green's function sometimes significantly improvs its accuracy.

In the following a special Green's function will be studied, namely the single-particle Green's function, and in Chapter 3 a two-particle Green's function is investigated.

## 1.3.2 Single-particle Green's function

The single-particle Green's function is physically important not only for its relation with experimental observables but also for its fundamental significance. Let us consider a system with several single-particle orbitals, and let us denote them with orbital index $i$ and spin index $\sigma$. The single-particle Green's function corresponds to setting $A = c_{i,\sigma}$ and $B = c^{\dagger}_{j,\sigma'}$. Hence its imaginary time definition is

$$G_{i\sigma,j\sigma'}(\tau) = -\langle T_{\tau}(\hat{c}_{i,\sigma}(\tau)\hat{c}^{\dagger}_{j,\sigma'}(0))\rangle. \tag{1.37}$$

The spectral function $\rho_{i\sigma,j\sigma'}(\omega)$ is a hermitian matrix (visible from Eq. (1.30)), for a fixed energy $\omega$. This means $\rho \in \mathbb{C}$ on the off-diagonal ($i \neq j$ or $\sigma \neq \sigma'$) and $\rho \in \mathbb{R}$ on the diagonal ($i = j$ and $\sigma = \sigma'$). Another important property of the spectral function, easily obtained using the Lehmann representation and the fermionic commutation rules [43], is the following property:

$$\int_{-\infty}^{\infty} d\omega \rho_{i\sigma,j\sigma'}(\omega) = \delta_{\sigma\sigma'}\delta_{ij}. \tag{1.38}$$

For a non-orthogonal orbital basis, the normalization above becomes equal to $\delta_{\sigma\sigma'}(S^{-1})_{ij}$ [13], where $S$ is the overlap matrix. In the following an orthonormal basis is assumed.

### Diagonal elements

The diagonal elements of the single particle Green's functions are arguably the most important in electronic structure calculations and they also have many symmetry properties. First note that the spectral function property in Eq. (1.38) for diagonal elements simply states that the spectral function should be normalized to integrate to one, which is advantageous to enforce when doing analytical continuations. Another important property, exploited when performing analytical continuations, is the non-negativeness in Eqs. (1.32), (1.33), which enables us to interpret the spectral functions as a probability distribution. For clarity, let us explicitly write down the diagonal single particle functions:

$$\rho_{i\sigma,i\sigma}(\omega) = \frac{1}{Z}\sum_{n,m}(e^{-\beta E_n} + e^{-\beta E_m})|\langle m|\hat{c}^{\dagger}_{i\sigma}|n\rangle|^2 \delta(\omega - (E_m - E_n)) \tag{1.39}$$

$$G_{i\sigma,i\sigma}(z) = \frac{1}{Z}\sum_{n,m}(e^{-\beta E_n} + e^{-\beta E_m})|\langle m|\hat{c}^{\dagger}_{i\sigma}|n\rangle|^2 \frac{1}{z - (E_m - E_n)} \tag{1.40}$$

$$G_{i\sigma,i\sigma}(\tau) = -\frac{1}{Z}\sum_{n,m} e^{-\beta E_n}|\langle m|\hat{c}^{\dagger}_{i\sigma}|n\rangle|^2 e^{\tau(E_n - E_m)}, \text{ for } 0 < \tau < \beta. \tag{1.41}$$

From the spectral function many quantities can be calculated, e.g. the occupation for that orbital. The occupation is equal to the imaginary time Green's

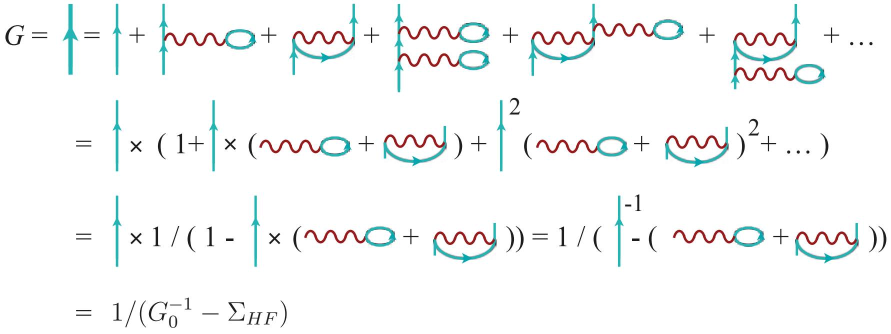

*Figure 1.6.* Green's function expressed by Feynman diagrams in the Hartree-Fock approximation [46].

function at $\tau = 0^-$. By using its Fourier transform and Cauchy's integral formula the occupation is given by [45]

$$\langle \hat{c}^\dagger_{i\sigma} \hat{c}_{i\sigma} \rangle = G(\tau = 0^-) = \int_{-\infty}^{\infty} d\omega n_F(\omega) \rho(\omega), \tag{1.42}$$

where $n_F(z) = 1/(e^{\beta z} + 1)$ is the Fermi-Dirac distribution.

**Non-interacting Green's function**

The ab initio electronic structure Hamiltonian (see Eq. (1.4)) consists of two terms, a non-interacting term and an interacting term. Such separation is also done for the Hubbard model (see Eq. (1.15)) and is in fact a common situation for other models as well. In these cases, it is useful to introduce the Green's function for only the non-interacting Hamiltonian. This is called bare, non-interacting or undressed Green's function, and is typically denoted by $G_0$. For a lattice system, using the Bloch theorem the hopping/non-interacting Hamiltonian is diagonal in the basis of lattice momentum $\boldsymbol{k}$, band index $n$ and spin $\sigma$, as seen in Eq. (1.7). The imaginary time Green's function is [45, 46]

$$G_{0,(\boldsymbol{k},n,\sigma)}(\tau) = (n_F(\varepsilon_{(\boldsymbol{k},n,\sigma)}) - 1) e^{-\tau \varepsilon_{(\boldsymbol{k},n,\sigma)}} \text{ ,for } 0 < \tau < \beta, \tag{1.43}$$

with Fourier transform

$$G_{0,(\boldsymbol{k},n,\sigma)}(i\nu_n) = 1/(i\nu_n - \varepsilon_{(\boldsymbol{k},n,\sigma)}). \tag{1.44}$$

From Eq. (1.35) the corresponding spectral function is

$$\rho_{0,(\boldsymbol{k},n,\sigma)}(\omega) = \delta(\omega - \varepsilon_{(\boldsymbol{k},n,\sigma)}), \tag{1.45}$$

which has Dirac-delta peaks at the band energy $\varepsilon_{(\boldsymbol{k},n,\sigma)}$. When the interaction is slowly turned on, the electrons become Fermi-Liquid quasi-particles. It is reflected in the interacting spectral function by a broadening of the Dirac-delta peaks, due to a finite life-time, and an energy shift, due to a mass enhancement. For stronger interaction non quasi-particle features arise and are contained in the spectral function. Experimentally the spectral function can be measured with angle-resolved photoemission spectroscopy [49].

**Self-energy and Dyson's equation**

The Dyson equation is the link between the non-interacting and the interacting Green's function:

$$G(z)^{-1} = G_0(z)^{-1} - \Sigma(z), \tag{1.46}$$

where $\Sigma(z)$ is called self-energy. The self-energy is responsible for the changes of the spectral function described just above, when the interaction is turned on. The meaning of Dyson's equation can be illustrated by using Feynman diagrams. The interacting Green's function is viewed as a propagator and is expressed as a sum of diagrams describing all possible interaction events between an electron and all the other electrons in the system. The contributing diagrams can be written as a geometrical sum of irreducible diagrams. The self-energy is the sum of all the irreducible diagrams [46]. In practice, calculating all irreducible diagrams is usually infeasible. However approximating the self-energy with only a few irreducible diagrams is common, such as the Hartree-Fock approximation, where the self-energy is a sum of a ring and an open oyster diagram, see Fig. 1.6. Instead of using a partial summation of all irreducible self-energy diagrams one can device other approximations. For example, one can approximate the self-energy to be local in space. It is one of the key ideas behind dynamical mean field theory (DMFT), which is the topic of the next chapter [27].

# 2. Dynamical mean field theory

Dynamical mean field theory (DMFT) is a method for obtaining a proper many-body solution of a system of interacting electrons on a lattice. Historically its development started by studying the Hubbard model, in Eq. (1.15), on a hyper-cubic lattice of $d$ dimensions, when $d$ goes to infinity [39]. It was realized that taking this limit simplified the calculations but still lead to non-trivial physics. A second breakthrough in the DMFT development was made when the Hubbard model was mapped onto a self-consistent impurity problem [40]. The mapping is exact for $d \to \infty$ with the lattice self-energy $\Sigma(\boldsymbol{k}, z)$ becoming momentum independent [15, 41, 42], thus

$$\Sigma(\boldsymbol{k}, z) \underset{d \to \infty}{\to} \Sigma(z). \tag{2.1}$$

By Fourier transforming Eq. (2.1), the self-energy in real space becomes local, which is another way of expressing the limit of $d \to \infty$. For finite dimensional systems, the locality of the self-energy is an approximation. Despite this approximation, DMFT has been applied with great success to many-body problems such as the Mott metal to insulator transition, doping of Mott insulators and phase separation, and improved the simulation accuracy for properties like spectral satellites, spin exchange, bulk modulus and lattice constants for various materials [15, 41, 42, 50–54]. Actually, DMFT is also exact in two other limits, the non-interacting and the atomic limits, see section 1.2.1.

## 2.1 Single impurity Anderson model

The single impurity Anderson model (SIAM) contains an interacting impurity site, a bath of non-interacting sites and a coupling between the impurity site and the bath:

$$\hat{H}_{\text{SIAM}} = \hat{H}_{\text{imp}} + \hat{H}_{\text{bath}} + \hat{H}_{\text{coupling}}. \tag{2.2}$$

As for the Hubbard model in Eq. (1.15), let us consider a single-orbital model. The impurity term $\hat{H}_{\text{imp}}$ contains an energy level $\varepsilon_0$ and the same interaction term as for one site in the Hubbard model, namely

$$\hat{H}_{\text{imp}} = \varepsilon_0(\hat{n}_\uparrow + \hat{n}_\downarrow) + U\hat{n}_\uparrow\hat{n}_\downarrow, \tag{2.3}$$

where $\hat{n}_\uparrow$ ($\hat{n}_\downarrow$) is the number operator for the spin up (down) impurity level. The chemical potential for the SIAM can conveniently be included in $\varepsilon_0$. The bath is described by

$$\hat{H}_{\text{bath}} = \sum_{b,\sigma} \varepsilon_b \hat{n}_{b,\sigma}, \tag{2.4}$$

with bath energy levels $\varepsilon_b$ and their occupation operator $\hat{n}_{b,\sigma}$. The coupling between bath and impurity is described by hopping elements and reads

$$\hat{H}_{\text{coupling}} = \sum_{b,\sigma} V_b(\hat{c}^\dagger_{b,\sigma}\hat{c}_\sigma + \hat{c}^\dagger_\sigma \hat{c}_{b,\sigma}), \tag{2.5}$$

where $V_b$ are the hopping strengths from bath to impurity (and vice versa), while $\hat{c}_{b,\sigma}$ and $\hat{c}^\dagger_{b,\sigma}$ are the annihilation and creation operators for the bath sites. The non-interacting Green's function for the impurity site is obtained by neglecting the Coulomb term in Eq. (2.3), and becomes [55]

$$g_0(z)^{-1} = z - \varepsilon_0 - \Delta(z). \tag{2.6}$$

Notice that the lower case letter $g$ is used to label *impurity* Green's functions and to distinguish them from lattice Green's functions, which we will introduce later. $\Delta(z)$ is the hybridization function which incorporates all the effects of the bath on the impurity site. In terms of the coupling and bath parameters, $\Delta$ is expressed as

$$\Delta(z) = \sum_b \frac{|V_b|^2}{z - \varepsilon_b}. \tag{2.7}$$

The SIAM is fully defined by $\Delta(z)$, $\varepsilon_0$ and $U$. There are many different numerical methods, called impurity solvers, for solving the SIAM and obtaining the self-energy $\Sigma_{\text{imp}}(z)$ at the impurity site. Using the Dyson equation and Eq. (2.6), the interacting Green's function for the impurity reads

$$g(z)^{-1} = g_0(z)^{-1} - \Sigma_{\text{imp}}(z) = z - \varepsilon_0 - \Delta(z) - \Sigma_{\text{imp}}(z). \tag{2.8}$$

Various QMC algorithms are used as impurity solvers. Most of them require working with Matsubara Green's functions for a finite temperature. Analytical continuation is therefore necessary in order to obtain dynamical quantities, such as the spectral function. An explicit parameterization of the Hamiltonian is unnecessary in QMC, since the impurity is formulated through its action which contains $\Delta$, not the parameters $V_b$ and $\varepsilon_b$. This is an advantage compared to other methods, such as exact diagonalization (ED), where one has to approximate the hybridization function $\Delta$, by representing it with a *few* bath sites:

$$\Delta(z) \approx \Delta_{\text{ED}}(z) = \sum_{b=1}^{n_b} \frac{|V_b|^2}{z - \varepsilon_b}. \tag{2.9}$$

As $n_b \to \infty$, this approximation becomes exact but due to the exponential scaling of the Hilbert space, only a few bath states are currently computationally feasible. After this discretization, an explicit form of the SIAM Hamiltonian is obtained and can be numerically diagonalized. Once the many-body states are found, the Green's function $g(z)$ is evaluated using the Lehmann representation in Eq. (1.40). QMC and ED are not the only solvers available, but are those mostly related to this thesis. Many other techniques can be found in the literature, as discussed in Ref. [42].

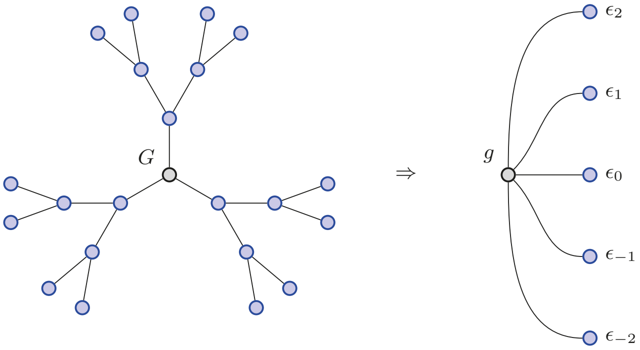

*Figure 2.1.* The mapping of the Bethe lattice with a coordination number of three to a SIAM with a finite number of bath states.

## 2.2 Self-consistency conditions

So far the connection between the impurity problem and the lattice problem has not yet been discussed. This is achieved by using the locality of the self-energy, see Eq. (2.1). The interacting lattice Green's function for a local self-energy can be written as

$$G(\boldsymbol{k},z)^{-1} = z + \mu - \varepsilon_{\boldsymbol{k}} - \Sigma(z). \tag{2.10}$$

Here and in the following, the upper case letter $G$ is used to indicate a *lattice* Green's function. Since the momentum dependence only enters through the dispersion energy $\varepsilon_{\boldsymbol{k}}$, the interacting local Green's function for the site at the origin becomes [31]

$$G(z) = \sum_{\boldsymbol{k}} e^{i\boldsymbol{k}\cdot\boldsymbol{0}} G(\boldsymbol{k},z) = \int d\omega \frac{D_0(\omega)}{z - \Sigma(z) + \mu - \omega}, \tag{2.11}$$

where the non-interacting density of states of the lattice is denoted by $D_0(\omega)$. The Dyson equation for the local lattice Green's function can hence be written [56]

$$G(z) = G_0(z - \Sigma(z)). \tag{2.12}$$

The mapping of the lattice problem in Eq. (1.15) to the impurity problem in Eq. (2.2) can be derived by a cavity construction for the action [31,41] or by showing that the two systems have the same local dressed skeleton diagrams in the limit of $d \to \infty$ [56]. The mapping states that the local lattice self-energy is the same as the impurity self-energy if the local Green's function is equal to the impurity Green's function [56], thus we seek

$$\Sigma(z) = \Sigma_{\text{imp}}(z) \tag{2.13}$$

$$G(z) = g(z). \tag{2.14}$$

Please note that this does not at all imply that $G_0(z)$ is equal to $g_0(z)$. Instead, $g_0(z)$ and the dynamical mean field $\Delta(z)$ have to be determined by the self-consistency Eqs. (2.13) and (2.14), while $G_0$ is fixed and determined by the lattice dispersion $\varepsilon_{\boldsymbol{k}}$. The set of equations in DMFT are usually solved by fixpoint iteration [31]. Given the non-interacting lattice Green's function $G_0(z)$ and a starting guess for the self-energy $\Sigma(z)$, the following steps provide a converged $\Delta$:

1. Calculate the impurity Green's function by $g(z) = G_0(z - \Sigma(z))$
2. Evaluate the non-interacting impurity Green's function $g_0^{-1}(z) = g^{-1}(z) + \Sigma(z)$ and the hybridization function $\Delta(z) = z - \varepsilon_0 - g_0^{-1}(z)$.
3. Use an impurity solver to provide a new impurity Green's function $g(z)$.
4. With the help of $g_0(z)$ and the new $g(z)$, calculate a new self-energy by $\Sigma_{\text{imp}} = g_0^{-1}(z) - g^{-1}(z)$.
5. Obtain a new value for the lattice self-energy by $\Sigma(z) = \Sigma_{\text{imp}}(z)$.

The steps are repeated until the dynamical mean field $\Delta(z)$ is converged within a chosen tolerance. Note, if the the impurity problem is solved only once, the impurity to lattice feedback is missing, i.e. the mean-field $\Delta(\omega)$ is not updated, and the translational invariance of the lattice breaks [41].

## 2.3 Bethe lattice

In the example above, DMFT is exact for $d = \infty$, but in general it is the number of neighbours in the lattice, $\acute{d}$, that has to reach this limit. The Bethe lattice (Cayley tree) is another commonly studied system in the DMFT community. This lattice, depicted in Fig. 2.1, has in the limit $\acute{d} \to \infty$ the non-interacting semicircular density of states

$$D_0(\omega) = \frac{2}{\pi}\sqrt{1-\omega^2}, \tag{2.15}$$

for $|\omega| < 1$ and zero otherwise. The non-interacting DOS $D_0$ is illustrated in Fig. 2.2. The Bethe lattice is often studied because $D_0$ has a finite bandwidth, like real materials, and Eq. (2.11) can be integrated analytically. At half-filling we get

$$G_0(z) = 2z\left(1 - \sqrt{1 - z^{-2}}\right), \tag{2.16}$$

leading to the simplified self-consistency loop [55]

$$\Delta(z) = \frac{1}{4}G(z). \tag{2.17}$$

## 2.4 Distributional exact diagonalization

As we pointed out in the previous sections, there are several techniques to solve the SIAM. Distributional exact diagonalization (DED) is a stochastic

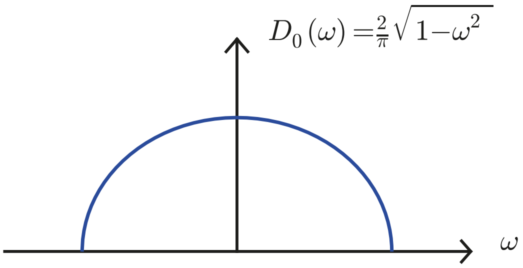

*Figure 2.2.* The non-interacting density of states for the Bethe lattice for $\acute{d} = \infty$.

and non-perturbative quantum impurity solver and will be briefly described in this section. In ED the hybridization is approximated with a *finite* number of bath states, as shown in Eq. (2.9). In standard ED one has to obtain the best possible set of hybridization parameters $V_b$ and $\varepsilon_b$ to satisfy the Eq. (2.9). This can be done by minimizing a deviation measure between $g_0(z)$ from Eq. (2.6) and its discretized counterpart $g_{0,\text{ED}}^{-1}(z) = z - \varepsilon_0 - \Delta_{\text{ED}}$, e.g. [57]

$$\chi^2 = \sum_n |g_{0,\text{ED}}(i\nu_n)^{-1} - g_0(i\nu_n)^{-1}|^2. \tag{2.18}$$

Once all the parameters in the Hamiltonian of the SIAM are determined, a many-body basis is chosen and the Hamiltonian is expressed as a matrix. After finding the eigenstates of the Hamiltonian, the Lehman representation is used to calculate $g(z)$. For $n_b$ bath sites and one impurity orbital, the dimension of the Hilbert space is $4^{n_b+1}$. This exponential growth as a function of $n_b$ hinders a big $n_b$ in brute force computations. Symmetries of the system, such as conservation of particles and spin, can be used to block diagonalize the matrix to gain computational speed and reduce memory usage. Despite these tricks, the feasibility of ED calculations for multi-orbital systems is limited to a few bath states. This may not be enough for systems with a complex hybridization function. DED tries to circumvent the exponential growth of the Hilbert space by considering an ensemble of $N$ SIAMs, instead of one SIAM. The bath parameters for each SIAM are determined stochastically. The resulting self-energies are averaged over the ensemble and the average is assumed to be local lattice self-energy, closing the DMFT loop. DED was applied in paper I (Ref. [58]) to study the Mott insulating state of the half-filled paramagnetic Hubbard model on the Bethe lattice. The DED method is briefly described in this context, even though its applicability extends to more general types of lattices and fillings. The particle-hole symmetry at half-filling gives $\varepsilon_0 = -U/2$. Given the non-interacting impurity Green's function $g_0(z)$, we want to represent it with a finite number of poles, like in ED. For DED it is technically convenient to have $g_0$ particle-hole symmetric, so we redefine it as

$$g_0(z)^{-1} = z - \Delta(z), \tag{2.19}$$

thus without $\varepsilon_0$. This imply the impurity level $\varepsilon_0$ is treated as an interaction term, like the self-energy, so that the interacting Green's function will be the same. The hybridization function is zero in the vicinity of the zero energy, which allows us to separate $g_0$ into a pole contribution at zero energy and a residual part, $\acute{g}_0$, which has a zero imaginary part in the vicinity of zero energy, namely

$$g_0(z) = \frac{a_0}{z} + \acute{g}_0(z), \tag{2.20}$$

with $\acute{\rho}_0(\omega) = -\frac{1}{\pi}\mathrm{Im}\acute{g}_0(\omega + i0^+) = 0$ for $\omega$ close to zero energy. By Taylor expanding the hybridization function, the residue $a_0$ can be estimated with $a_0^{-1} = 1 - \partial_z \Delta(z = 0)$. We interpret $\acute{\rho}_0(\omega)$ as a probability distribution and use it to stochastically sample $n_b$ points $\{b_1^\nu, b_2^\nu, ..., b_{n_b}^\nu\}$, see Fig. 2.3. The $N$ different SIAMs we consider are labeled with $\nu$ and are chosen such that their ensemble average should fulfill

$$g_0(z) = \lim_{N\to\infty} \frac{1}{N} \sum_{\nu=1}^{N} g_{0,\mathrm{ED}}^\nu(z). \tag{2.21}$$

For each SIAM $\nu$ we approximate $g_0$ according to

$$g_0(z) \approx g_{0,\mathrm{ED}}^\nu(z) = \frac{a_0}{z} + \sum_{i=1}^{n_b} \frac{a_i^\nu}{z - b_i^\nu}, \tag{2.22}$$

where the normalization condition for $g_0$ demands

$$\sum_{i=1}^{n_b} a_i^\nu = 1 - a_0. \tag{2.23}$$

Due to the particle-hole symmetry only $n_b/2$ points $b_i^\nu$ needs be sampled by demaning $b_{n_b+1-i}^\nu = -b_i^\nu$ and $a_{n_b+1-i}^\nu = a_i^\nu$ for $i \leq n_b/2$. The parameters $a_i^\nu$ are chosen to be constants and $a_i^\nu = \frac{1-a_0}{n_b}$ to fulfil Eq. (2.23). The next step in the DED algorithm is to map $g_{0,\mathrm{ED}}^\nu$, with parameters $a_i^\nu$ and $b_i^\nu$, to the non-interacting Green's function of the SIAM, with parameters $V_b^\nu$ and $\varepsilon_b^\nu$. The mapping is done by demanding

$$\frac{a_0}{z} + \sum_{i=1}^{n_b} \frac{a_i^\nu}{z - b_i^\nu} = g_{0,\mathrm{ED}}^\nu(z) = \frac{1}{z - \Delta_{\mathrm{ED}}^\nu(z)}, \tag{2.24}$$

where the hybridization is

$$\Delta_{\mathrm{ED}}^\nu(z) = \sum_{b=1}^{n_b} \frac{|V_b^\nu|^2}{z - \varepsilon_b^\nu}. \tag{2.25}$$

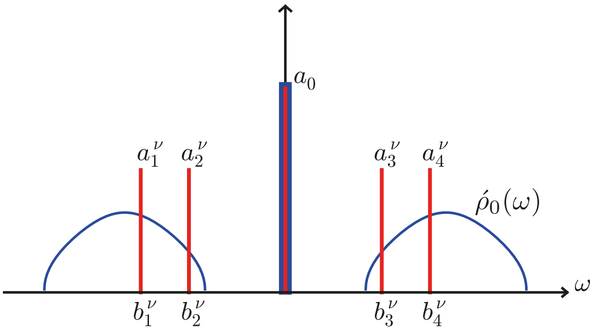

*Figure 2.3.* Schematic representation of the discretization of $g_0(z)$ to $g_0^\nu(z)$ by using $\acute{\rho}_0(\omega)$ as a probability density.

The bath energies $\varepsilon_b^\nu$ are found by $g_{0,\mathrm{ED}}^\nu(\varepsilon_b^\nu) = 0$ and once found, $V_b^\nu$ are determined by $\partial_z g_{0,\mathrm{ED}}^\nu(z=\varepsilon_b^\nu) = |V_b^\nu|^{-2}$. The SIAM is now defined and exact diagonalization followed by the Lehmann sum (see Eq. (1.39)) gives $g_{\mathrm{ED}}^\nu$ and the self-energy

$$\Sigma_{\mathrm{ED}}^\nu(z) = (g_{0,\mathrm{ED}}^\nu(z))^{-1} - (g_{\mathrm{ED}}^\nu(z))^{-1} + \varepsilon_0. \tag{2.26}$$

The self-energy has a pole at $z=0$ and the corresponding pole in $(g_{\mathrm{ED}}^\nu)^{-1}$ is treated separately and not by Eq. (2.26). Taylor expanding $g_{\mathrm{ED}}^\nu$ enables us to estimate the self-energy residue at $z=0$ with $\alpha^\nu = -(\partial_z g_{\mathrm{ED}}^\nu(z=0))^{-1}$. As the last step all the self-energies from the $N$ SIAMs are averaged:

$$\Sigma(z) = \frac{1}{N}\sum_{\nu=1}^{N} \Sigma_{\mathrm{ED}}^\nu(z). \tag{2.27}$$

The pole at $z=0$ is separately calculated according to $\alpha = 1/N\sum_{\nu=1}^{N}\alpha^\nu$. Notice that Eq. (2.27) is an approximation, even for $N\to\infty$. In the next iteration, $a_0$ can be calculated from Eqs. (2.17) and (2.19), giving $a_0 = 1/(1+\alpha/4)$. This algorithm was used for different $U$, $n_b$ and distances $\delta$ above the real axis. In article I, agreement was found at the Matsubara points with CTQMC, within the statistical uncertainty of the CTQMC data. Close to the real axis, $\delta \leq 0.001$, quasiparticles at the inner edge of the Hubbard bands were obtained, see the spectral function in Fig. 2.4. A D-DMRG spectral function is shown for comparison. The D-DMRG gives similar shape of the Hubbard band except for the quasiparticle peaks at the inner edge. Small wiggles are present at both the inner and the outer band and the insulating gap is slightly smaller than what is obtained using the DED method.

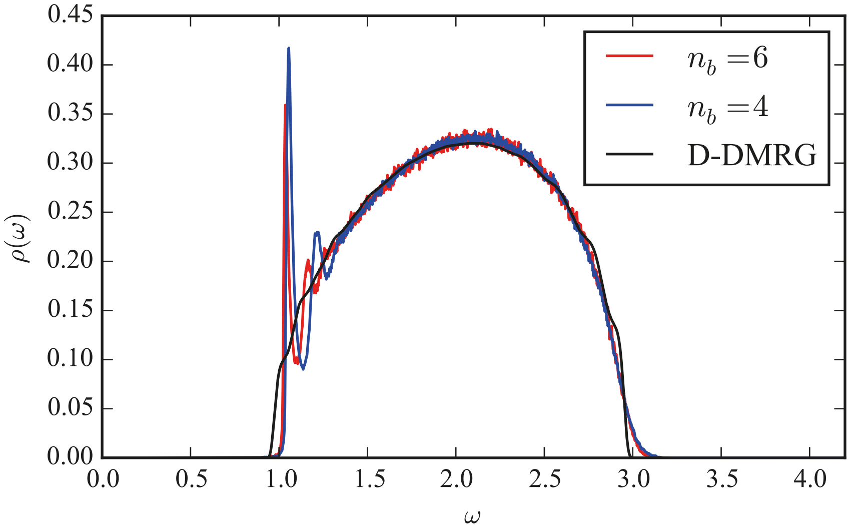

*Figure 2.4.* The spectral function $-\frac{1}{\pi}\text{Im}g(\omega+i\delta)$ for $U=4$ and $\delta=0.001$. Quasiparticles are visible at the inner edge of the upper Hubbard band. Results are compared with D-DMRG data from Ref. [56].

## 2.5 DFT+DMFT

So far in this chapter, DMFT has been discussed for the single band Hubbard model and the corresponding SIAM. However, to reliably calculate properties of materials, typically more than one band has to be considered. On the other hand, we also know that DFT for many systems is not accurate enough. This section describes how to combine DFT with DMFT, in order to study correlated materials in a ab-initio fashion. With this approach, DFT is used as a starting point and its electronic structure is projected onto a subset of (a few) localized orbitals to which the Coulomb interaction is explicitly added. This means one has to study the Hamiltonian in Eq. (1.13), but with hoppings $t_{i,j}^{\text{KS}}$ determined from DFT, and with the explicit Coulomb interaction only acting on a subset of all orbitals. Also, since the KS hopping approximately include the Coulomb interaction, a double counting terms needs to be added to the Hamiltonian, and this is discussed in section 2.5.3. Information about the localized orbitals and the projection procedure of quantities from the DFT basis to these localized orbitals is described below in section 2.5.1. In section 2.5.2, an expansion and a parameterization of the Coulomb interaction for the localized orbitals is shown. There are different flavours of DFT+DMFT and a common approach is to keep the charge density and the DFT hoppings fixed and converge the DMFT cycle. But once this is achieved, a new charge density can be calculated, incorporating the information from the self-energy. This results in updated DFT hoppings, and how to converge this cycle is outlined in section 2.5.4. Note that the content of this section is used extensively in section 2.6, where results of paper II are summarized, and in chapter 3, about x-ray absorption spectroscopy.

### 2.5.1 Projection to localized basis

Let us start by considering a DFT basis $\{|\boldsymbol{k},a\rangle\}$, describing all valence electrons on a lattice, where $\boldsymbol{k}$ is the lattice momentum and $a$ an orbital and spin index. This basis may be chosen rather freely, see section 1.1.2. Then we can define a local basis $\{i\}$ describing a subset of the valence electrons, where $i$ is an orbital and spin index. One can now define projectors from the DFT basis to the local basis, and use them to recover the DMFT equations. Let us write down the lattice Green's function operator

$$\tilde{G} = ((z+\mu)\tilde{1} - \tilde{H}_{\mathrm{KS}} - \tilde{\Sigma} + \tilde{\Sigma}_{\mathrm{DC}})^{-1}. \tag{2.28}$$

This operator equation is analogous to Eq. (2.10), up to the additional double counting term $\tilde{\Sigma}_{\mathrm{DC}}$, which is described in section 2.5.3.

The DFT basis is typically not orthonormal within a $\boldsymbol{k}$-point, with an overlap matrix $S_{a,b}(\boldsymbol{k}) = \langle \boldsymbol{k}a|\boldsymbol{k}b\rangle$. Due to this non-orthonormality, it is helpful to introduce the dual basis set $\{|\boldsymbol{k}\acute{a}\rangle\}$, which is defined by the relations [27]

$$\langle \boldsymbol{k}_1\acute{a}|\boldsymbol{k}_2 b\rangle = \langle \boldsymbol{k}_1 a|\boldsymbol{k}_2\acute{b}\rangle = \delta_{a,b}\delta_{\boldsymbol{k}_1,\boldsymbol{k}_2} \tag{2.29}$$

$$\tilde{1} = \sum_{\boldsymbol{k},a} |\boldsymbol{k}\acute{a}\rangle\langle \boldsymbol{k}a| = \sum_{\boldsymbol{k},a} |\boldsymbol{k}a\rangle\langle \boldsymbol{k}\acute{a}|. \tag{2.30}$$

Inserting the identity operator $\tilde{1}$ twice, the local Green's function becomes

$$\begin{aligned} G_{i,j}(z) = \langle i|\tilde{G}|j\rangle &= \sum_{k_1,a}\sum_{k_2,b} \underbrace{\langle i|\boldsymbol{k}_1,\acute{a}\rangle}_{P_{i,a}(\boldsymbol{k}_1)}\underbrace{\langle \boldsymbol{k}_1,a|\tilde{G}|\boldsymbol{k}_2,b\rangle}_{G_{a,b}(\boldsymbol{k}_1,z)\delta_{\boldsymbol{k}_1,\boldsymbol{k}_2}}\underbrace{\langle \boldsymbol{k}_2,\acute{b}|j\rangle}_{P^*_{j,b}(\boldsymbol{k}_2)} \\ &= \sum_{\boldsymbol{k},a,b} P_{i,a}(\boldsymbol{k})G_{a,b}(\boldsymbol{k},z)P^*_{j,b}(\boldsymbol{k}) = \sum_{\boldsymbol{k}} (P(\boldsymbol{k})G(\boldsymbol{k},z)P^\dagger(\boldsymbol{k}))_{i,j}, \end{aligned} \tag{2.31}$$

where $P(\boldsymbol{k})$ is called projector matrix, $G(\boldsymbol{k},z)$ lattice Green's function and the last expression is written in implicit matrix multiplication form[1]. Similarly, the non-interacting local impurity Hamiltonian is constructed by down-folding the KS Hamiltonian, i.e.

---

[1] From the properties of the dual basis, the projector element $P_{i,a}(\boldsymbol{k})$ can be expressed as $P_{i,a}(\boldsymbol{k}) = \langle i|\boldsymbol{k}\acute{a}\rangle = \sum_b (S^{-1})_{b,a}\langle i|\boldsymbol{k}b\rangle$, which in case of an orthonormal DFT basis simplifies to $\langle i|\boldsymbol{k}a\rangle$. To evaluate the Green's function elements $G_{a,b}(\boldsymbol{k}) = \langle \boldsymbol{k},a|\tilde{G}|\boldsymbol{k},b\rangle$, we can introduce $\tilde{A} = \tilde{G}^{-1} = (z+\mu)\tilde{1} - \tilde{H}_{\mathrm{KS}} - \tilde{\Sigma} + \tilde{\Sigma}_{\mathrm{DC}}$ and investigate the expression: $\langle \boldsymbol{k}a|\tilde{A}^{-1}\tilde{A}|\boldsymbol{k}b\rangle = \langle \boldsymbol{k}a|\tilde{1}|\boldsymbol{k}b\rangle$. Inserting the identity operator on the left hand side and expanding dual states gives: $\sum_{c,d} G_{a,c}(\boldsymbol{k})(S^{-1}(\boldsymbol{k}))_{c,d}A_{d,b}(\boldsymbol{k}) = S_{a,b}(\boldsymbol{k})$. This matrix equation can easily be reshuffled to finally obtain the matrix expression $G = SA^{-1}S$.

$$H_{i,j}^{\text{imp},(0)} = \langle i|\tilde{H}_{\text{KS}}|j\rangle = \sum_{\boldsymbol{k}} (P(\boldsymbol{k})H_{\text{KS}}(\boldsymbol{k})P^{\dagger}(\boldsymbol{k}))_{i,j}. \tag{2.32}$$

Also here an implicit matrix multiplication form is used. The requirements of the local basis are stricter than those of the DFT basis. First of all the local basis should describe well the Hilbert space associated to those degrees of freedom which are treated wrongly in DFT. Also, the local basis is often chosen (for technical reasons) to be orthonormal (in contrast to the DFT basis in RSPt) and its overlap matrix can be expressed in terms of the DFT overlap matrix, i.e.

$$s_{i,j} = \langle i|j\rangle = \sum_{\boldsymbol{k}} (P(\boldsymbol{k})S_{\text{KS}}(\boldsymbol{k})P^{\dagger}(\boldsymbol{k}))_{i,j}. \tag{2.33}$$

In the DMFT cycle, a projection onto the local basis is required, but also the inverse process. In particular, the local self-energy calculated from the impurity problem can be up-folded to the DFT basis according to

$$\Sigma_{a,b}(\boldsymbol{k},z) = \langle \boldsymbol{k},a|\tilde{\Sigma}|\boldsymbol{k},b\rangle = \sum_{\boldsymbol{k}} (P(\boldsymbol{k})^{\dagger}\Sigma^{\text{loc}}(z)P(\boldsymbol{k}))_{a,b}. \tag{2.34}$$

In RSPt there are two different types of localized orbitals, called orthogonalized LMTO (ORT) basis and muffin-tin heads (MT) basis. The ORT orbitals consist of linear combinations of the DFT orbitals. This results in rather delocalized orbitals, without any pure angular momentum character and with $s_{i,j} = \delta_{i,j}$ Instead an MT orbital is constructed only from the muffin-tin part of a LMTO. This results in localized orbitals with pure angular momentum. However, since the DFT basis is not entirely complete the local overlap matrix calculated according to Eq (2.33) is typically only approximately equal to the identity matrix. Or more precisely, the deviation from the identity matrix is small if the intersection between the two basis sets is big [17,27].

### 2.5.2 Coulomb expansion

The interacting part of the impurity Hamiltonian in DMFT for a multi-orbital system reads

$$\hat{H}_{\text{int.}} = \frac{1}{2} \sum_{abcd,\sigma\sigma'} U_{abcd}\hat{c}_{a,\sigma}^{\dagger}\hat{c}_{b,\sigma'}^{\dagger}\hat{c}_{c,\sigma'}\hat{c}_{d,\sigma}, \tag{2.35}$$

where each term describes a process illustrated by Fig. 1.1, and $U_{abcd}$ is given by Eq. (1.6). By expanding the Coulomb interaction $1/|\boldsymbol{r}-\boldsymbol{r}'|$ in terms of spherical harmonics and with basic functions of the form

$$\psi_i(\boldsymbol{r}) = f_{n_i,l_i}(r)Y_{l_i,m_i}(\theta,\phi), \tag{2.36}$$

the Coulomb interaction tensor becomes [14]

$$U_{abcd} = \delta_{m_a+m_b,m_c+m_d} \sum_{k=0}^{k_{\max}} c^k(l_a,m_a;l_d,m_d)c^k(l_c,m_c;l_b,m_b) \times R^k(n_al_a,n_bl_b,n_cl_c,n_dl_d). \tag{2.37}$$

The term $\delta_{m_a+m_b,m_c+m_d}$ in Eq. (2.37) simply states that the $z$-component of the angular momentum has to be conserved in the scattering event. The Gaunt coefficients

$$c^k(l,m;l',m') = \sqrt{\frac{4\pi}{2k+1}} \int_0^{2\pi} d\phi \int_0^{\pi} d\theta \sin\theta Y^*_{l,m}(\theta,\phi) Y_{k,m-m'}(\theta,\phi) \times Y_{l',m'}(\theta,\phi) \tag{2.38}$$

take care of the angular integrals in Eq. (1.6) and are easily evaluated. By considering the parity of the spherical harmonics in Eq. (2.38), only Gaunt coefficients with $l+l'+k$ being an even number can be non-zero. The two Gaunt coefficients in Eq. (2.37) constrain the $k$-expansion to a maximum of $k_{\max} = \min(|l_a+l_d|,|l_c+l_b|)$. The last factor to discuss in Eq. (2.37) is the parameter

$$R^k(n_al_a,n_bl_b,n_cl_c,n_dl_d) = \int_0^\infty \int_0^\infty dr dr' r^2 r'^2 f_{n_a,l_a}(r) f_{n_b,l_b}(r') \frac{r_<^k}{r_>^{k+1}} \times f_{n_d,l_d}(r) f_{n_c,l_c}(r'), \tag{2.39}$$

where $r_<$ ($r_>$) indicates $\min(r,r')$ ($\max(r,r')$). It is customary to define the Slater-Condon parameters

$$\begin{aligned} F^k(nl,n'l') &= R^k(nl,n'l',n'l',nl) \\ G^k(nl,n'l') &= R^k(nl,n'l',nl,n'l'), \end{aligned} \tag{2.40}$$

where $F$ and $G$ describe Coulomb and exchange integrals, respectively. For the Coulomb interaction between $d$-orbitals, for any given principal quantum number, $F^k = G^k$, and only the three parameters $F^0$,$F^2$ and $F^4$ are relevant, due to the constrains mentioned above. The orbital average of $U_{ijji}$ for a $(n,l)$-shell is

$$\frac{1}{(2l+1)^2} \sum_{i,j} U_{ijji} = F^0, \tag{2.41}$$

and is often denoted as the parameter $U$, without any indices. For $l=2$ the sum over $U_{ijij}$ terms gives

$$\sum_{i,j} U_{ijji} = 5F^0 + 20 \underbrace{\frac{F^2+F^4}{14}}_{J}, \tag{2.42}$$

where $J$ is the Hund's intrasite exchange parameter. Since the ratio $F^2/F^4$ approximately is constant ($\approx 0.6$) for $3d$ elements [59], one can express the full Coulomb tensor by the two parameters $U$ and $J$. So far we have considered the bare Coulomb interaction $1/|\boldsymbol{r}-\boldsymbol{r}'|$. However, there are screening effects from uncorrelated electrons. This screening reduces the $F^k$ parameters, especially $F^0$. Constrained RPA aims to take the screening into account [60], but in practice $F^0$ is often used as a free parameter.

### 2.5.3 Double counting

After the projection of the DFT bandstructure, a Coulomb interaction term is explicitly added to the Hamiltonian for these localized orbitals. This results in a double counting of certain components of the full Coulomb interaction. Hence we have to remove the approximate Coulomb interaction added by DFT for these correlated states by introducing a double counting term. This is a non-trivial task since DFT functionals are non-linear and do not have a diagrammatic representation [61, 62]. Several different double counting expressions exist, e.g. around mean-field (AMF) [35], fully localized limit (FLL) [63, 64] and the so called exact double counting [65]. In paper II the FLL double counting potential

$$\Sigma_{\text{DC}} = U(N-1/2) - J(N_\sigma - 1/2), \tag{2.43}$$

is used, where $N$ is the total electron occupation, $N_\sigma$ the occupation with spin $\sigma$, and $U$ and $J$ the Coulomb and Hund's exchange parameters respectively. For a non-spin polarized functional, $n/2$ is used instead of $n_\sigma$ in Eq. (2.43).

### 2.5.4 Charge self consistency

Once the lattice self-energy has been calculated by, e.g. DMFT, the charge density $n(\boldsymbol{r})$ can be updated and inserted into the DFT functional. By repeating this additional step charge self-consistency can also be achieved. Fig. 2.5 shows a charge self-consistent DFT+DMFT flow diagram. The one-particle density operator can be expressed as the Green's function operator at imaginary time $\tau \to 0^-$ and by using the Fourier series expansion in Eq. (1.18), the charge density can be written

$$n(\boldsymbol{r}) = \langle \boldsymbol{r}|\tilde{n}|\boldsymbol{r}\rangle = \langle \boldsymbol{r}| \lim_{\tau\to 0^-} \frac{1}{\beta} \sum_{\nu_n} \tilde{G}(i\nu_n) e^{-i\nu_n \tau} |\boldsymbol{r}\rangle, \tag{2.44}$$

where $\tilde{G}(i\nu_n)$ is given by Eq. (2.28). This is further simplified by inserting the identify operator $\tilde{1}$ twice, namely

$$n(\boldsymbol{r}) = \sum_{\boldsymbol{k},a,b} \psi_{\boldsymbol{k},\acute{a}}(\boldsymbol{r}) n_{\boldsymbol{k},a,b} \psi^*_{\boldsymbol{k},\acute{b}}(\boldsymbol{r}), \tag{2.45}$$

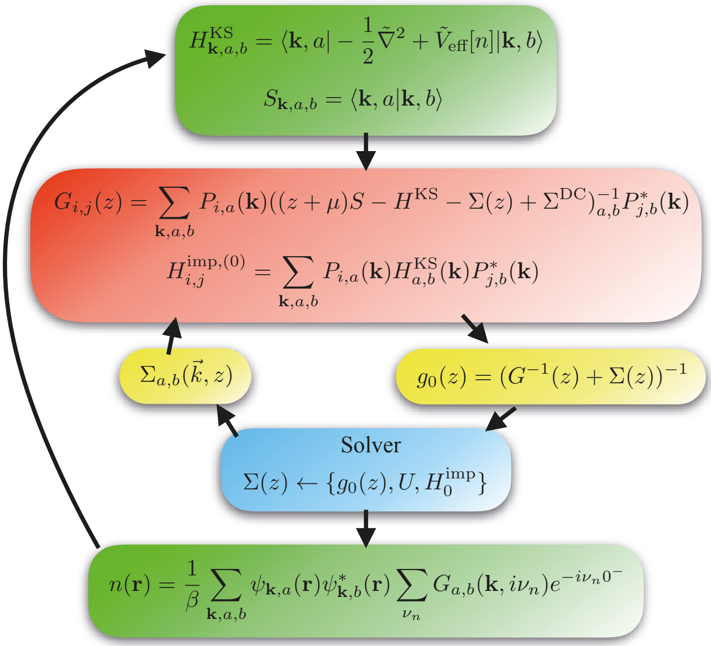
$H^{\mathrm{KS}}_{\mathbf{k},a,b} = \langle \mathbf{k}, a| -\frac{1}{2}\tilde{\nabla}^2 + \tilde{V}_{\mathrm{eff}}[n]|\mathbf{k}, b\rangle$
$S_{\mathbf{k},a,b} = \langle \mathbf{k}, a|\mathbf{k}, b\rangle$
$G_{i,j}(z) = \sum_{\mathbf{k},a,b} P_{i,a}(\mathbf{k})((z+\mu)S - H^{\mathrm{KS}} - \Sigma(z) + \Sigma^{\mathrm{DC}})^{-1}_{a,b} P^*_{j,b}(\mathbf{k})$
$H^{\mathrm{imp},(0)}_{i,j} = \sum_{\mathbf{k},a,b} P_{i,a}(\mathbf{k}) H^{\mathrm{KS}}_{a,b}(\mathbf{k}) P^*_{j,b}(\mathbf{k})$
$\Sigma_{a,b}(\vec{k}, z)$
$g_0(z) = (G^{-1}(z) + \Sigma(z))^{-1}$
Solver
$\Sigma(z) \leftarrow \{g_0(z), U, H^{\mathrm{imp}}_0\}$
$n(\mathbf{r}) = \frac{1}{\beta}\sum_{\mathbf{k},a,b} \psi_{\mathbf{k},a}(\mathbf{r})\psi^*_{\mathbf{k},b}(\mathbf{r}) \sum_{\nu_n} G_{a,b}(\mathbf{k}, i\nu_n) e^{-i\nu_n 0^-}$

*Figure 2.5.* Flow diagram of charge self-consistent DFT+DMFT.

where $n_{\boldsymbol{k},a,b} = \lim_{\tau\to 0^-} \frac{1}{\beta}\sum_{\nu_n} G_{a,b}(\boldsymbol{k}, i\nu_n) e^{-i\nu_n\tau}$, $\psi_{\boldsymbol{k},\acute{a}}(\boldsymbol{r}) = \sum_c (S^{-1})_{c,a}\psi_{\boldsymbol{k},c}(\boldsymbol{r})$, and $\psi_{\boldsymbol{k},c}(\boldsymbol{r})$ being a DFT basis function.

### 2.5.5 DFT+$U$

This section describes the DFT+$U$ method, which is a historically successful method for improving the description beyond plain DFT of correlated insulators [34–38]. The DFT+$U$ method requires convergence over two separate entities; the whole electron density, as in DFT, and the local one-particle density matrix of chosen orbitals. In this sense, DFT+$U$ can be seen as a special case of DFT+DMFT, with a Hartree-Fock (HF) like method as the impurity solver. Consequently, the self-energy becomes static (energy independent) and for a $(n,l)$-shell can be written as [64]

$$\Sigma^{\sigma}_{i,j} = \sum_{k,l}(U_{iklj}\sum_{\sigma'} n^{\sigma'}_{k,l} - U_{ikjl} n^{\sigma}_{k,l}), \tag{2.46}$$

where the one-particle density matrix $n^{\sigma}_{i,j}$ is calculated from the local interacting Green's function and here assumed to be spin-diagonal.

A problem with DFT+$U$ is that the converged results sometimes depend on the initial one-particle density matrix or, equivalently, the initial self-energy.

This problem is illustrated by the fact that in literature one can find different DFT+$U$ results (band gaps gaps, spins and orbital moments, etc.) for identical systems [66–70]. Among the systems studied in paper II, FeO and CoO have a partially occupied shell ($t_{2g}$) and therefore many local minima solutions.

### 2.5.6 Exchange integrals

In many materials the magnetization density is localized around the atoms, forming atomic magnetic moments. In this case, macroscopic magnetism is a collective phenomenon where these atomic magnetic moments order [71]. The driving force for magnetic moments ordering originates from pair-wise exchange interaction. The exchange interaction between atomic sites $i$ and $j$ usually is denoted as $\acute{J}_{i,j}$ and is a microscopic quantity of quantum mechanical origin. Together with the magnetic moments it gives rise to macroscopic observables such as Curie temperature, magnon dispersion and magnetic susceptibility. The total energy variations of the electronic system due to infinitesimally small rotations of spins can be simulated by the classical Heisenberg spin model [72]

$$H = -\sum_{i \neq j} J_{i,j} \boldsymbol{e}_i \cdot \boldsymbol{e}_j, \tag{2.47}$$

where the sum is over all atomic pairs and $\boldsymbol{e}_i$ denotes the unit vector along the magnetic moment at the atomic site $i$. $J_{i,j} = \acute{J}_{i,j} s_i s_j$ contains the exchange interaction as well as the size of the spin moments. This mapping to a classical system enables large scale simulations in the thermodynamic limit, e.g. using Monte Carlo methods or the time-dependent Landau-Lifshitz-Gilbert equation. The extraction of $J_{i,j}$ from the electronic structure can be done even for correlated systems with a local self-energy [73], using the expression

$$J_{i,j} = \frac{1}{4\beta} \sum_{n,a} \langle a | \tilde{\Delta}_i^{\mathrm{xs}}(i\nu_n) \tilde{G}^{\uparrow}_{i,j}(i\nu_n) \tilde{\Delta}_j^{\mathrm{xs}}(i\nu_n) \tilde{G}^{\downarrow}_{j,i}(i\nu_n) | a \rangle, \tag{2.48}$$

where $a$ here denotes a localized orbital index at site $i$ and $\tilde{\Delta}_i^{\mathrm{xs}}$ is the local (dynamic) exchange splitting, namely

$$\tilde{\Delta}_i^{\mathrm{xs}}(i\nu_n) = \tilde{H}^{\mathrm{KS}}_{i,\uparrow} + \tilde{\Sigma}_{i,\uparrow}(i\nu_n) - \tilde{H}^{\mathrm{KS}}_{i,\downarrow} - \tilde{\Sigma}_{i,\downarrow}(i\nu_n). \tag{2.49}$$

Variables in the two equations above are diagonal in spin-space since spin-orbit coupling has been neglected. This formalism is implemented in the RSPt code [53]. Note that Eq. (2.48) can not be used for a paramagnetic configuration where the exchange splitting $\Delta_i^{\mathrm{xs}}$ is zero, and that $J_{ij}$ may depend on the initial magnetic configuration. In paper II we study this configuration dependence and the role of spin polarization of the DFT functional. A summary of that work is presented in section 2.6.

There are other ways of extracting $J_{i,j}$ from the electronic structure than the magnetic force theorem (MFT) expression in Eq. (2.48), such as the frozen magnon approach [74] or by considering total energy differences of several magnetic configurations [75].

## 2.6 Exchange integrals using L(S)DA+U of transition metal oxides

In this section results presented in paper II (Ref. [76]) are summarized. The main finding in the paper is that a spin nonpolarized functional (e.g. LDA) is preferable, compared to a spin polarized functional (e.g. LSDA), for extracting exchange integrals directly from DFT+$U$ total energy differences. This conclusion is obtained by studying the ferromagnetic (FM) and the antiferromagnetic (AFM) configurations using both LDA+$U$ and LSDA+$U$.

We calculated exchange integrals according to Eq. (2.48). From the Heisenberg model in Eq. (2.47), we extracted the energy difference $\Delta E_J$ between the FM and the AFM configuration. The total energy difference $\Delta E_{\text{tot}}$ obtained directly from the electronic structure was also calculated. By comparing these energy differences for both DFT functionals, $\Delta E_{\text{tot}}$ using LSDA+$U$ stands out, as can be seen in Fig. 2.6. The discrepancies in LSDA+$U$ between $\Delta E_{\text{tot}}$ and $\Delta E_J(\text{R})$, where R denotes either a FM or a AFM reference configuration, indicate an inconsistency of the mapping from the electronic structure system to the Heisenberg model. However, for LDA+$U$, $\Delta E_{\text{tot}}$ agrees reasonably well with $\Delta E_J$. Furthermore, $\Delta E_J$ shows less functional dependence than $\Delta E_{\text{tot}}$. The reference configuration dependence of $\Delta_J$ indicate a non-Heisenberg behavior and is depicted with the shaded areas in Fig. 2.6. This behaviour is explained as a consequence of the different electronic structures of the FM and AFM configurations (see paper II). The generality of the conclusions are ensured by studying five different insulating TMOs, namely $\text{CaMnO}_3$ (CMO), MnO, FeO, CoO and NiO, having different crystal structures and $d$-shell occupations.

To gain insights on the total energy results, we calculated the density of states. In Fig. 2.7, the DOS of NiO is shown. By considering both the band gaps $E_G$, obtained from the DOS, and the total exchange field $J_0 = \sum_j J_{i,j}$, we noticed that the $E_G$ is larger, and $J_0$ smaller, in LSDA+$U$ than in LDA+$U$. Also, AFM has a larger $E_G$ and a smaller $J_0$ than in FM. The bigger band gap in AFM than in FM can be understood from the simple dimer system illustrated in Fig. 2.8. In LSDA+$U$ the double counting is spin polarized, but by using $J = 0$ the double counting is the same in LDA+$U$ and LSDA+$U$ and only the exchange correlation functionals are different. We observe also for $J = 0$ an inverse relationship between band gaps and exchange parameters. From simple super-exchange arguments one would expect $J_0 \propto E_G^{-1}$ but our results show a weaker dependence.

We also tested how robust our results are by varying the $U$ parameter. Both functionals show a increasing Heisenberg behavior with increasing $U$ but LDA+$U$ consistently provides a better agreement between direct total en-

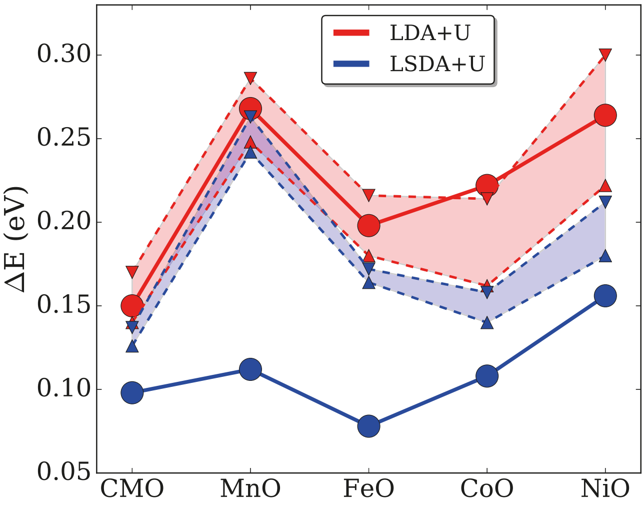

*Figure 2.6.* Total energy differences ($\Delta E = E_{\mathrm{FM}} - E_{\mathrm{AFM}}$) obtained from LDA+$U$ (red) and LSDA+$U$ (blue) calculations. Solid lines are total energies whereas dashed lines with upward (downward) triangles represent total energies obtained from $J_{i,j}$ extracted from a AFM (FM) configuration.

ergy differences $\Delta_{\mathrm{tot}}$ and exchange parameter derived total energy differences $\Delta_J$, than with LSDA+$U$.

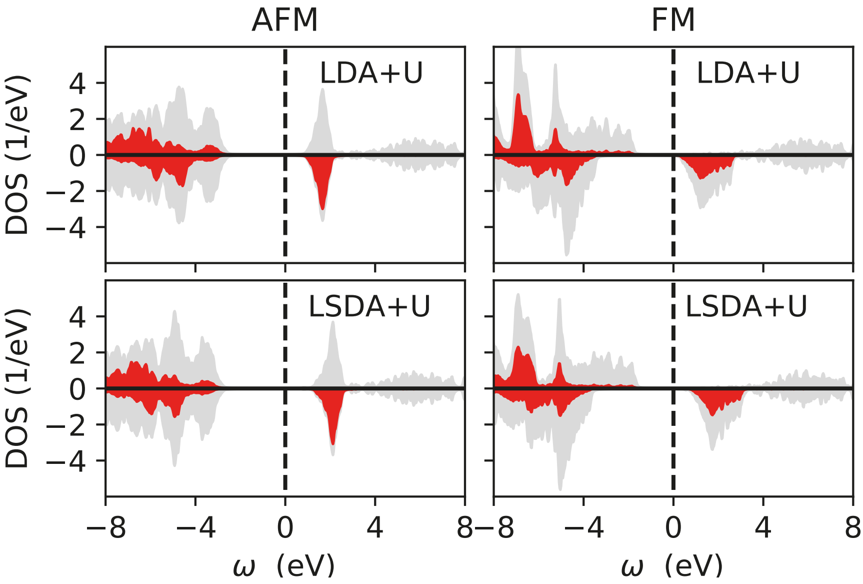

*Figure 2.7.* Total density of states (grey) of NiO and projected density of states of Ni 3*d* orbitals of one site (red).

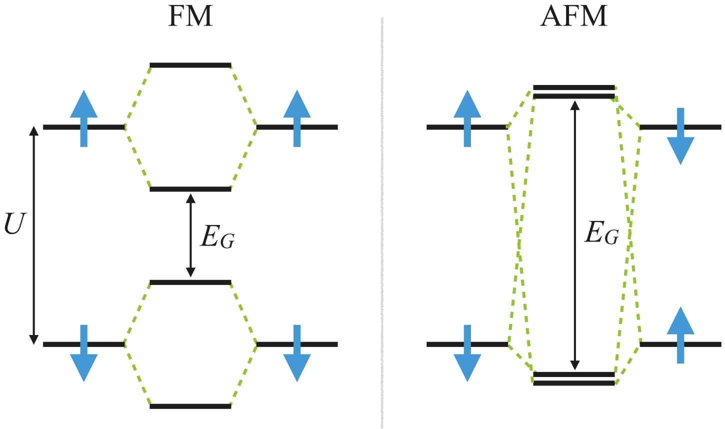

*Figure 2.8.* Two site system with spin conserving hopping of FM (left panel) and AFM (right panel) order at half-filling. The gaps are different in FM and AFM configurations, due to different hybridization between the two sites.

# 3. X-ray absorption spectroscopy

X-ray absorption spectroscopy (XAS) is a widely used technique for studying materials and can provide information about e.g. elemental composition, electronic structure, coordination environment, atomic binding lengths and magnetic moments. Spectroscopy is used to characterize materials used for instance for hydrogen storage [77, 78], batteries [79], and catalysis [80, 81]. Readers interested in more details on core-level spectroscopy are referred to textbooks [82–85]. In XAS the samples can be gases, solutions or solids, and experiments are usually performed at synchrotron radiation facilities, like MAX IV [86], where tunable, monochromatic and intense x-ray beams of high quality are generated. In the x-ray absorption (XA) process a core electron is excited to an unoccupied orbital by an incoming photon. An XA spectrum is obtained by tuning the photon energy and measuring the absorption of the light. XA spectra are labelled by which core electrons are excited, see Fig. 3.1. In this thesis excitations of core $2p$ electrons, resulting in absorption edges labeled $L_{2,3}$, are studied for various TMOs, see Fig. 3.2. Transition selection rules, which are described in Section 3.1, determine which valence orbitals an electron can be excited into. For a specific absorption edge, the binding energy increases monotonically and significantly with the atomic number, making XAS an element specific technique. For the materials studied in this thesis, soft x-rays in the regime $\approx 10^2 - 10^3$ eV are used to measure the $L_{2,3}$-edges. An XA spectrum edge is commonly divided into extended x-ray absorption fine structure (EXAFS) and x-ray absorption near-edge structure (XANES). The latter, which is also called near-edge x-ray absorption fine structure (NEXAFS), is studied in this thesis. In XANES of strongly correlated systems, a many body description is needed to understand and model the physical process accurately, whereas for weakly correlated systems the absorption spectra approximately resembles the unoccupied part of the valence density of states [87]. As is illustrated later in this chapter, oxidation state and site symmetry are important for the line shape of the NEXAFS spectrum.

For a homogenous and isotropic material the light intensity is described by Lambert-Beer's law [88]

$$I = I_0 e^{-\mu s}, \tag{3.1}$$

where $s$ is the sample thickness, $I$ ($I_0$) the transmitted (initial) light intensity and $\mu = \mu(\omega)$ the energy dependent and material characteristic attenuation absorption coefficient $\mu$. There are various experimental techniques to measure the XA coefficient. Transmission detection means that the initial and transmitted light intensity is measured, which puts constraints in sample thickness and is the standard technique for hard x-rays. Another approach is to measure electrons, photons and ions created as a result of the core excitation, escaping the sample surface. In fluorescence yield detection the number of photons are measured. By also detecting their energies (partial fluorescence yield), further information can be obtained which is not restricted by the short life time of the intermediate state where the core hole is present [89]. For soft x-rays with photon energy smaller than 1 keV, electron yield dominates over fluorescence yield. By also measuring the kinetic energy of the electrons (partial electron yield), different Auger decay channels can be analyzed [90, 91]. A technique that is related to XAS is electron energy loss spectroscopy (EELS). In this transmission electron microscopy (TEM) technique, high kinetic energy electrons are transmitted through the sample and measured at different scattering angles, see review [92]. Because of the short de Broglie wavelength atomic scale resolution can be obtained, see Ref. [93] and section 3.4, and for very high kinetic energy electrons and small scattering angles the EELS spectrum is identical to the XA spectrum.

The x-ray magnetic linear dichroism (XMLD) and x-ray magnetic circular dichroism (XMCD) are two powerful techniques to investigate the absorption dependence on the light polarization. In XMCD the so called sum-rules can be used to extract spin and orbital magnetic moments in ferromagnetic materials [94, 95]. In section 3.4 the linear polarization dependence is shown to be crucial for understanding the experimental atomic scale variations of the EELS spectrum.

Calculating the absorption coefficient is a vast research field and there are historically two approaches, either using a delocalized single-particle picture with DFT [96] or a localized atomic multiplet description [97]. Both of these methods have shortcomings and more advanced approaches have been developed, such as time-dependent DFT [98, 99], multiple scattering theory [100], multiplet ligand field theory (MLFT) [101], Bethe-Salpeter method [102, 103], configuration interaction (CI) [104], DFT+DMFT [105–107], and DFT+MLFT [108]. A DFT+MLFT approach based on the DMFT formalism is presented in paper III and summarized in section 3.3. The same approach is applied to study $L_{2,3}$-edges of strained $CaTiO_3$, see section 3.4, and Mo doped $LaFeO_3$, see paper IV and its summary in section 3.5.

## 3.1 Dipole transition operator

The XA spectrum can be calculated using the Green's function formalism outlined in Section 1.3.1 with operators $\hat{A} = \hat{B}^\dagger$ and $\hat{B} = \hat{T}$, where $\hat{T}$ is the transition operator which describes the excitation from a core state into a valence state. This transition can be written in terms of the photon electron interaction according to Fermi's golden rule, and in the weak-field approximation

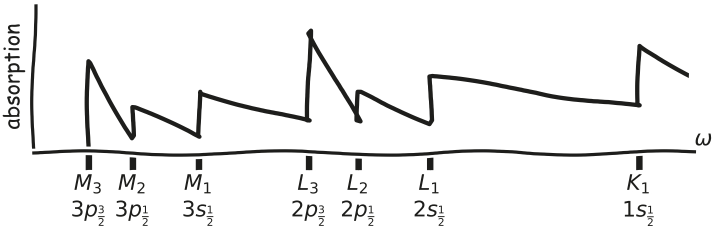

*Figure 3.1.* Schematic picture of a XA spectrum as a function of the photon energy for 3d-elements. XA edges and corresponding core states are labeled.

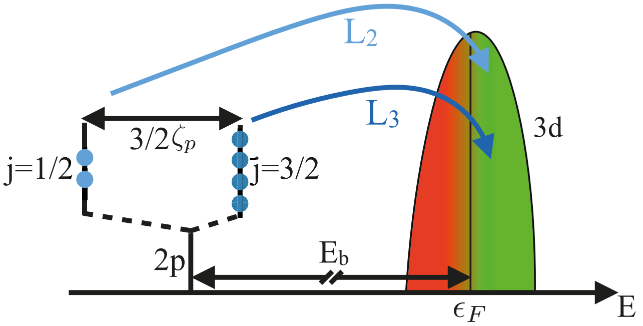

*Figure 3.2.* Schematic picture of the $L_{2,3}$-edge XA process. An electron is excited from the $2p$ core states to the $3d$ valence states. Note that the energy scale is schematic, and not representative of real energy differences.

becomes [84, 109]

$$\tilde{T} \propto \boldsymbol{A} \cdot \tilde{\boldsymbol{p}}, \tag{3.2}$$

where $\boldsymbol{A}$ is the light vector potential and $\tilde{\boldsymbol{p}}$ the electron momentum operator. In the dipole approximation of small photon momentum $\boldsymbol{q}$, the light vector potential factor $e^{i\boldsymbol{q}\cdot\boldsymbol{r}} \approx 1$, which reduces the transition operator to $\tilde{T} \propto \boldsymbol{\varepsilon} \cdot \tilde{\boldsymbol{p}}$, where $\boldsymbol{\varepsilon}$ is the light polarization unit vector. In the case of the same Hamiltonian with and without a core hole, the transition operator can also be expressed as

$$\tilde{T} = \boldsymbol{\varepsilon} \cdot \tilde{\boldsymbol{r}}, \tag{3.3}$$

where $\tilde{\boldsymbol{r}}$ is the position operator [110].

In a (localized) single-particle basis, the dipole transition operator in second quantization can be written as

$$\hat{T} = \sum_{i,j,\sigma} T_{i,j} \hat{c}^{\dagger}_{i,\sigma} \hat{c}_{j,\sigma}, \tag{3.4}$$

where $i$, $j$ are indices belonging to the orbitals involved in the XA process, and $T_{i,j} = \langle i|\tilde{T}|j\rangle$. Note that the spin polarization is conserved in the transitions ($\Delta\sigma = 0$). If each single-particle basis function is composed of a spherical harmonic $Y_{l,m}$ together with a radial function $f_{n,l}$, which depends on the principle quantum number and the angular momentum (but not its $z$-projection $m$), like in Eq (2.36), the transition matrix becomes

$$\begin{aligned} T_{i,j}^{(k)} &= \langle f_{n_i,l_i} Y_{l_i,m_i} | \tilde{r}_k | f_{n_j,l_j} Y_{l_j,m_j} \rangle \\ &= \int_0^\infty dr f_{n_i,l_i}^*(r) f_{n_j,l_j}(r) r^3 \int_0^\pi d\theta \int_0^{2\pi} d\phi \sin\theta Y_{l_i,m_i}^*(\theta,\phi) Y_{l_j,m_j}(\theta,\phi) \frac{r_k}{r}, \end{aligned} \tag{3.5}$$

for cartesian light polarization vector $\boldsymbol{\varepsilon} = \boldsymbol{e}_k$, with $k \in \{x,y,z\}$. The angular part can be calculated analytically and expressed in terms of Gaunt coefficients [14, 110], and gives the dipole selection rule $\Delta l = l_i - l_j = \pm 1$. Left and right polarized lights are written as vectors

$$\boldsymbol{\varepsilon}_l = \frac{-1}{\sqrt{2}}(\boldsymbol{e}_x + i\boldsymbol{e}_y) \tag{3.6}$$

$$\boldsymbol{\varepsilon}_r = \frac{1}{\sqrt{2}}(\boldsymbol{e}_x - i\boldsymbol{e}_y), \tag{3.7}$$

which together with $z$-polarized light obey the additional selection rules:

$$\boldsymbol{\varepsilon}_z : \Delta m = 0 \tag{3.8}$$

$$\boldsymbol{\varepsilon}_l : \Delta m = 1 \tag{3.9}$$

$$\boldsymbol{\varepsilon}_r : \Delta m = -1 \tag{3.10}$$

according to the angular part of Eq. (3.5).

For $L_{2,3}$-edge XAS, which is addressed in this thesis, a $2p$ core electron is excited to an empty $3d$ state. For this process the elements of the radial part of the transition matrix in Eq. (3.5) are the same and can be ignored. The angular part is

$$T^{(z)} = \begin{bmatrix} 0 & 0 & 0 \\ \frac{1}{\sqrt{5}} & 0 & 0 \\ 0 & \frac{2}{\sqrt{15}} & 0 \\ 0 & 0 & \frac{1}{\sqrt{5}} \\ 0 & 0 & 0 \end{bmatrix}, T^{(l)} = \begin{bmatrix} 0 & 0 & 0 \\ 0 & 0 & 0 \\ \frac{1}{\sqrt{15}} & 0 & 0 \\ 0 & \frac{1}{\sqrt{5}} & 0 \\ 0 & 0 & \sqrt{\frac{2}{5}} \end{bmatrix}, T^{(r)} = \begin{bmatrix} \sqrt{\frac{2}{5}} & 0 & 0 \\ 0 & \frac{1}{\sqrt{5}} & 0 \\ 0 & 0 & \frac{1}{\sqrt{15}} \\ 0 & 0 & 0 \\ 0 & 0 & 0 \end{bmatrix}, \tag{3.11}$$

where incremental ordering of $m$ is used for both $3d$ and $2p$ orbitals.

### Dipole transition elements using Bloch states

In the RSPt code the dipole transition matrix elements for the localized orbitals are calculated through the Bloch states in the DFT basis. This implies a projection of the DFT transition matrix elements. The transition elements of the localized orbitals $\{i\}$ can be written as a vector with three light polarization components $\{x, y, z\}$, namely

$$\boldsymbol{T}_{i,j} = \langle i|\tilde{\boldsymbol{p}}|j\rangle. \tag{3.12}$$

Similar to the projection steps discussed in section 2.5.1, we evaluate Eq. (3.12) by using the DFT basis:

$$\begin{aligned}
\boldsymbol{T}_{i,j} &= \sum_{\boldsymbol{k}_1,a}\sum_{\boldsymbol{k}_2,b} \langle i|\boldsymbol{k}_1,\acute{a}\rangle\langle\boldsymbol{k}_1,a|\tilde{\boldsymbol{p}}|\boldsymbol{k}_2,b\rangle\langle\boldsymbol{k}_2,\acute{b}|j\rangle \\
&= \sum_{\boldsymbol{k}\in\mathrm{BZ}}\sum_{a,b}\langle i|\boldsymbol{k},\acute{a}\rangle\langle\boldsymbol{k},a|\tilde{\boldsymbol{p}}|\boldsymbol{k},b\rangle\langle\boldsymbol{k},\acute{b}|j\rangle \\
&= \sum_{R\in g}\sum_{\boldsymbol{k}\in\mathrm{IBZ}}\sum_{a,b}\langle i|R\boldsymbol{k},\acute{a}\rangle\langle R\boldsymbol{k},a|\tilde{\boldsymbol{p}}|R\boldsymbol{k},b\rangle\langle R\boldsymbol{k},\acute{b}|j\rangle = \{RR^{-1} = I\} \\
&= \sum_{R\in g} R \sum_{\boldsymbol{k}\in\mathrm{IBZ}}\sum_{a,b}\langle i|R\boldsymbol{k},\acute{a}\rangle\langle R\boldsymbol{k},a|R^{-1}\tilde{\boldsymbol{p}}|R\boldsymbol{k},b\rangle\langle R\boldsymbol{k},\acute{b}|j\rangle \\
&= \sum_{R\in g} R \sum_{\boldsymbol{k}\in\mathrm{IBZ}}\sum_{a,b}\langle i|R\boldsymbol{k},\acute{a}\rangle\underbrace{\langle\boldsymbol{k},a|\tilde{\boldsymbol{p}}|\boldsymbol{k},b\rangle}_{\boldsymbol{p}_{a,b}(\boldsymbol{k})}\langle R\boldsymbol{k},\acute{b}|j\rangle, \qquad (3.13)
\end{aligned}$$

where $\langle\boldsymbol{k}_1,a|\tilde{\boldsymbol{p}}|\boldsymbol{k}_2,b\rangle = \langle\boldsymbol{k}_1,a|\tilde{\boldsymbol{p}}|\boldsymbol{k}_1,b\rangle\delta_{\boldsymbol{k}_1,\boldsymbol{k}_2}$ is used in the first step, $R$ is a symmetry operation of the crystallographic point group $g$, and we have used the Bloch state property $\phi_{R\boldsymbol{k}}(\boldsymbol{r}) = \phi_{\boldsymbol{k}}(R^{-1}\boldsymbol{r})$ in the last step. The momentum operator in the Bloch basis, $\boldsymbol{p}_{a,b}(\boldsymbol{k})$, can be evaluated and we consider it in the following to be a known quantity. For localized orbitals whose angular part is described by spherical harmonics, thus $i = (l_i, m_i)$, we can use the Wigner rotation matrix $D$ to write

$$\psi_i(R\boldsymbol{r}) = \sum_{m_k=-l_i}^{l_i} D^{(l_i)\,*}_{m_i,m_k}(R)\,\psi_{l_i,m_k}(\boldsymbol{r}). \tag{3.14}$$

This is useful in order to formulate the inner products between the localized states and the Bloch states in Eq. (3.13) in terms of the projectors (see section 2.5.1) and Wigner matrices. Then we get

$$\boldsymbol{T}_{i,j} = \sum_{R\in g} R \sum_{m_k=-l_i}^{l_i} D^{(l_i)}_{m_i,m_k}(R) \sum_{m_l=-l_j}^{l_j} \boldsymbol{p}^{\mathrm{local}}_{m_k,m_l} D^{(l_j)\,*}_{m_j,m_l}(R), \tag{3.15}$$

where

$$\boldsymbol{p}^{\mathrm{local}}_{m_k,m_l} = \sum_{\boldsymbol{k}\in\mathrm{IBZ},a,b} \langle l_i m_k|\boldsymbol{k},\acute{a}\rangle\,\boldsymbol{p}_{a,b}(\boldsymbol{k})\,\langle\boldsymbol{k},\acute{b}|l_j m_l\rangle \tag{3.16}$$

is the projected momentum operator (without $\boldsymbol{k}$-point symmetrization). With tensor notation Eq. (3.15) becomes more compact:

$$T_{a,i,j} = \sum_{R\in g} R_{a,b} D_{i,k}(R)\, p^{\mathrm{local}}_{b,k,l} (D^{\dagger}(R))_{l,j}. \tag{3.17}$$

This was recently implemented in the RSPt code. Generalizing this formalism beyond the dipole approximation, using $\tilde{T} = \boldsymbol{\varepsilon} \cdot \tilde{\boldsymbol{p}} e^{i\boldsymbol{q}\cdot\tilde{\boldsymbol{r}}}$, would be an interesting project relevant for high photon energy studies.

## 3.2 Green's function

Since the dipole transition operator $\hat{T}$ is a sum of pairs of creation and annihilation operators the corresponding Green's function is of two-particle type and of bosonic character. The spectral function $\rho$ associated with the Green's function $G$, see Eq. (1.35), represents the absorption coefficient $\mu$. The energies of the eigenstates in the presence of a core-hole are much higher than those without it. Actually this energy difference is equal to the absorption edge energy. This mathematically means that the Boltzmann weight $e^{-\beta E_m}/Z$ for eigenstates $|m\rangle$ with a core-hole is negligible. In principle the transition matrix in Eq. (3.5) also has non-zero $3d \to 2p$ elements, making $\hat{T}$ Hermitian ($\hat{T} = \hat{T}^\dagger$). Including also these transition elements in $\hat{T}$, the Green's function describing the XA process, see Eq. (1.29), becomes

$$G(z) = \frac{1}{Z} \sum_{n\in g, m\in e} e^{-\beta E_n} \left( \frac{1}{z-(E_m-E_n)} - \frac{1}{z+(E_m-E_n)} \right) |\langle m|\hat{T}|n\rangle|^2, \tag{3.18}$$

where $g$ ($e$) refers to the set of all eigenstates without (with) a core-hole. From Eq. (3.18) the corresponding spectral function, see Eq. (1.35), is clearly an odd function of energy. However, often only the $2p \to 3d$ transitions are included in $\hat{T}$, simplifying Eq. (1.29) to

$$G(z) = \frac{1}{Z} \sum_{n\in g, m\in e} e^{-\beta E_n} \frac{|\langle m|\hat{T}|n\rangle|^2}{z-(E_m-E_n)}. \tag{3.19}$$

The corresponding spectral function is in this case zero for negative energies and coincides with the spectral function corresponding to Eq. (3.18) for positive energies. From Eq. (3.19), we see that the XAS process excites eigenstates (with maximum energy of a few $k_B T$ above the lowest eigenenergy) to all possible core-hole eigenstates allowed by the dipole transition operator $\hat{T}$, resulting in a spectral peak at energy $E_m - E_n$. An equivalent, but more computationally suitable [111], expression of the Green's function in Eq. (3.19) is

$$G(z) = \frac{1}{Z} \sum_{n\in g} e^{-\beta E_n} \langle n|\hat{T}^\dagger \frac{1}{z-(\hat{H}-E_n)} \hat{T}|n\rangle. \tag{3.20}$$

In this form the Green's function can efficiently be evaluated using the Lanczos algorithm, see Appendix B. The life time of the core hole is finite, actually it is very short ($\sim 10^{-15}$ s). The corresponding decay rate $\delta$ can be incorporated in the Green's function expression in Eq. (3.20) by using $z = \omega + i\delta$, which will broaden the delta-peaks in the spectral function into Lorentzians, with $\delta$ the half-width at half-maximum (HWHM). For numerical values of $\delta$ please see e.g. Appendix B in Ref. [83].

In the following, the results of three projects will be presented. In the first project, a method to calculate XA spectra was developed and four TMOs were studied. The work resulted in paper III and section 3.3 contains a summary of the main results. The second project, see section 3.4, is about atomic-plane resolution of strained $CaTiO_3$. The third project, see section 3.5 and paper IV, is about Mo doped $LaFeO_3$.

## 3.3 Transition metal oxides: MnO, FeO, CoO and NiO

In this section results included in paper III (Ref. [112]) are summarized. Before discussing them, it is better to present some general discussion of the construction of the SIAM Hamiltonian $\hat{H}$, which is needed to describe the XA process (see Eq. (3.20)). The methodology used in this and following XA projects is DFT+MLFT. This means the DFT band structure is projected onto the TM $3d$ and $2p$ orbitals to generate a SIAM Hamiltonian which is diagonalized and used to generate the XA spectra. From a DFT+DMFT perspective, this approach corresponds to only solving the impurity problem once, thus skipping the self-consistency and therefore breaking the lattice translational invariance [41]. Indeed, performing the DMFT self-consistency loop, like in Ref. [106], should give more accurate results and is currently under development in the RSPt code. The projection procedure onto localized orbitals, in this case ORT-orbitals (see section 2.5.1), and how to describe the Coulomb interaction is described in section 2.5. For $L_{2,3}$-edges, the relevant Slater-Condon parameters are $F^0_{dd}, F^2_{dd}, F^4_{dd}, F^0_{pd}, F^2_{pd}, G^1_{pd}$, and $G^3_{pd}$. The screened values of $F^0_{dd}$ and $F^0_{pd}$ are difficult to calculate and are set to values found in literature [106, 113, 114]. The other Slater-Condon parameters are assumed to be unscreened or weakly screened (a few percentage points).

### Spin orbit coupling

Spin orbit coupling (SOC) is an atomic property with relativistic origin[1]. The SOC Hamiltonian in first quantized form for a $(n,l)$-shell with $N$ electrons and SOC parameter $\zeta$ is

$$\tilde{H}_{\mathrm{SOC}} = \zeta \sum_{i=1}^{N} \tilde{\boldsymbol{l}}_i \cdot \tilde{\boldsymbol{s}}_i = \zeta \sum_{i=1}^{N} \left( \tilde{l}_i^z \tilde{s}_i^z + \frac{1}{2} (\tilde{l}_i^+ \tilde{s}_i^- + \tilde{l}_i^- \tilde{s}_i^+) \right), \tag{3.21}$$

---

[1] The SOC originates from expanding the Dirac equation in terms of the ratio of the electron speed over the speed of light. The SOC parameter is $\zeta \propto \langle f | \frac{1}{c^2 r} \frac{dV(r)}{dr} | f \rangle$, where $f$ is the radial part of the wavefunction and $V(r)$ is a spherically symmetric potential. The SOC parameter $\zeta$ is big for localized orbitals.

where for particle $i$, $\tilde{\boldsymbol{l}}_i$ ($\tilde{\boldsymbol{s}}_i$) is the orbital (spin) angular momentum vector operator, $\tilde{l}_i^z$ ($\tilde{s}_i^z$) the $z$-projected orbital (spin) angular momentum operator and $\tilde{l}_i^{\pm}$ ($\tilde{s}_i^{\pm}$) the raising and lowering orbital (spin) angular momentum operators. In the last expression in Eq. (3.21), the first term is diagonal in the $(l, m, \sigma)$ basis and in second quantized form becomes

$$\zeta \sum_{m=-l}^{l} \sum_{\sigma \in \{-\frac{1}{2}, \frac{1}{2}\}} \sigma m \hat{c}^{\dagger}_{l,m,\sigma} \hat{c}_{l,m,\sigma}. \tag{3.22}$$

The other terms flip the spin and can be written as

$$\zeta \frac{1}{2} \sum_{m=-l}^{l-1} \sqrt{(l-m)(l+m+1)} (\hat{c}^{\dagger}_{l,m+1,\downarrow} \hat{c}_{l,m,\uparrow} + \hat{c}^{\dagger}_{l,m,\uparrow} \hat{c}_{l,m+1,\downarrow}). \tag{3.23}$$

For $3d$ orbitals $\zeta$ is rather small (less than 100 meV) in comparison to other relevant energies, e.g. bandwidth. But for core $2p$ orbitals in transition metal oxides $\zeta$ is of the order of several eVs and thus absolutely necessary to include in the simulations. This is the only term breaking the degeneracy of the single particle Hamiltonian for the $2p$ shell in our simulations. Thus, the $2p$ shell is described without any spin or crystal-field splitting, or hybridization with the environment.

**Double counting**

In this work we have used the MLFT double counting

$$\Sigma_{\mathrm{DC}} = n_d U_{dd} + 6U_{pd} - \delta_{\mathrm{CT}}, \tag{3.24}$$

which acts as a chemical potential for the $3d$ orbitals. The expression is derived from energy considerations of different configurations [115], and $n_d$ is the nominal $3d$ occupation, $U_{dd}$ and $U_{pd}$ average repulsion energies defined in Ref. [112], and $\delta_{\mathrm{CT}}$ charge transfer correction energy [116].

No double counting is needed for the $2p$ core states since the energy position of the $2p$ orbitals only determines the absolute position of the $L_{2,3}$-edge spectrum. This is anyway hard to get correct, and typically calculated spectrum is shifted in energy for better comparison with the experimental $L_{2,3}$ spectrum.

**Hybridization function discretization**

The studied systems have octahedral ($O_h$) symmetry, which implies that four degenerate $e_g$ spin-orbitals and six degenerate $t_{2g}$ spin-orbitals diagonalize the non-relativistic single particle Hamiltonian and the hybridization function of the $3d$ shell. This simple representation allows us to parameterize the hybridization function by a few discrete bath states. The discretization of the independent $e_g$ and $t_{2g}$ hybridization functions in paper III starts by selecting a

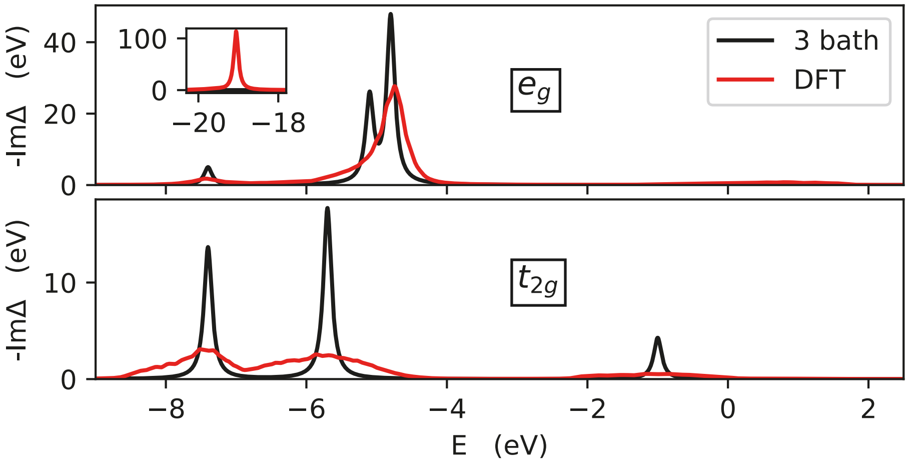

*Figure 3.3.* Continuous and discretized DFT hybridization function of FeO. The inset shows the hybridization with oxygen 2*s* orbitals. A HWHM broadening of 0.07 eV is used.

few bath energies, $\varepsilon_b$, at positions where the spectral weight of the hybridization function is large. Then the corresponding hopping terms, $V_b$, are determined such that the integrated spectral weight of the continuous and discrete hybridization functions match in the vicinity of the bath energies. As an example, the discretized and continuous hybridization spectra of FeO are shown in Fig. 3.3.

The bath and coupling Hamiltonian terms are

$$\sum_i \varepsilon_{b_i} \hat{b}_i^\dagger \hat{b}_i + \sum_{i,j} V_{i,j} (\hat{d}_i^\dagger \hat{b}_j + \text{h.c.}), \tag{3.25}$$

where $\hat{b}$ ($\hat{d}$) annihilates an electron on a bath (3$d$) orbital, parameterized by the bath energies $\varepsilon_b$ and hoppings $V$. We can then adjust the local 3$d$ energies to correct for the hybridization approximation error. This is only needed if zero or a few bath states are used to capture the correct crystal-field splitting. Without this adjustment the $e_g$ orbitals have lower energies than the $t_{2g}$ orbitals for the systems studied in paper III. This is due to the hybridization between $e_g$ and oxygen 2$s$ orbitals, which is especially strong with the ORT basis, see e.g. the inset of Fig. 3.3. In paper III the on-site energy adjustment is achieved by demanding the local non-interacting Green's function $g_0$, see Eq. (2.6), and its discretized version to resemble each other. In Fig. 3.3, the absence of a bath state around -19 eV in the $e_g$ shell is justified since it is too far away from the Fermi level to enable charge transfer. Instead the hybridization effect is captured by the on-site energy shift.

### Total Hamiltonian

Finally, the total impurity Hamiltonian for the $3d$ and $2p$ shells is summarized as

$$
\begin{aligned}
\hat{H} = & \sum_{i,j} t_{i,j} \hat{d}_i^\dagger \hat{d}_j + \sum_i \varepsilon_{b_i} \hat{b}_i^\dagger \hat{b}_i + \sum_{i,j} V_{i,j} (\hat{d}_i^\dagger \hat{b}_j + \text{h.c.}) \\
& + \hat{H}_{3d}^{\text{SOC}} + \hat{H}_{2p}^{\text{SOC}} + \varepsilon_p \sum_i \hat{p}_i^\dagger \hat{p}_i - \Sigma_{\text{DC}} \sum_i \hat{d}_i^\dagger \hat{d}_i + \hat{H}_U,
\end{aligned}
\tag{3.26}
$$

where the first term contains the non relativistic and adjusted $3d$ on-site energies, the second and third terms describe the bath and its coupling to the impurity, the fourth and fifth terms are due to the SOC (see Eq. (3.21)), then the onsite energy of the $2p$ orbitals. The last two terms are the double counting correction and the last term the Coulomb interaction (see Eq. (2.35)). Please note that $t_{i,j}$ in Eq. (3.26) is diagonal in the cubic harmonics basis with a splitting between $e_g$ and $t_{2g}$ orbitals which can be described by a crystal-field parameter $10Dq$.

### Work flow summary

In all the XAS projects discussed in this thesis, the FP-LMTO software RSPt [22] was used for the DFT calculations, projections to the localized orbitals, calculations of the Slater integrals, calculations of the SOC parameters and generation of hybridization functions and projected DOS. A Python package has been developed, as a part of RSPt, and used, if needed, to transform correlated orbitals to a local single-particle Hamiltonian diagonal form, discretize hybridization functions, correct on-site energies due to this approximation, and construct single-particle Hamiltonians in a format suitable for Quanty. The many body script language Quanty [117, 118] was used to find the lowest relevant eigenstates and calculate the corresponding spectra, using the Lanczos algorithm outlined in Appendix B. A recently developed open source Python implementation of the exact diagonalization algorithm has also been used, as a complement to Quanty [119].

### Results

To characterize the ground states of the four investigated TMOs in terms of eigenstates and their degeneracies, we start the discussion from an atomic limit with a nominal occupation of $n$ electrons in the 3d-shell. Let us at the very beginning consider the case of no hybridization, no crystal field, no SOC and no Coulomb interaction, thus with no degeneracy splitting terms in the Hamiltonian of Eq. (3.26). There are $\binom{10}{n}$ ways of distributing the electrons in the $3d$-shell and all of these configurations are degenerate. By introducing the Coulomb interaction term, these configurations split up and it is useful to characterize the eigenstates according to their expectation values of the square of the orbital and spin angular momentum operators, $\hat{\boldsymbol{L}}^2$ and $\hat{\boldsymbol{S}}^2$, respectively[2]. For each eigenstate, the expectation values $\langle\hat{\boldsymbol{L}}^2\rangle$ and $\langle\hat{\boldsymbol{S}}^2\rangle$ will take values $L(L+1)$ and $S(S+1)$, where $L$ ($S$) is an (half) integer. For each pair of $L$ and $S$, the energy degeneracy of states is $(2S+1)(2L+1)$. We can use Hund's rules to find the pair of $L$ and $S$ with the lowest energy. For example, in case of $\mathrm{Fe}^{+2}$, where $n=6$, Hund's rules give $S=2$ and $L=2$, and we will have 25 states with the lowest eigenenergy. When SOC is also included in the Hamiltonian for the $d$-shell, we get further degeneracy splitting and the expectation value of the square of the total angular momentum operator, $\hat{\boldsymbol{J}}^2$, characterizes the eigenstates. Similarly as above, for each eigenstate, $\langle\hat{\boldsymbol{J}}^2\rangle = J(J+1)$, where $J$ is a half-integer. Possible $J$ values are $|S-L|, |S-L|+1, ..., |S+L|$, each with a degeneracy of $2J+1$. Hund's third rule dictates which $J$ will have the lowest energy, and for Fe it is $J = S+L = 2+2 = 4$. The ground state degeneracy is thus 9. In paper III the XA spectrum with these terms in the Hamiltonian is shown, alongside spectra in other interesting limits.

Let us now instead consider the system from a non-interacting limit and start with only crystal field splitting present in the Hamiltonian. Without $\hat{H}_U$, Hund's rules do not apply and the ground state is obtained by simply occupying the lowest single particle states. For $\mathrm{Fe}^{+2}$ with $n=6$ and a positive $10Dq$, this means that the $t_{2g}$-shell is fully occupied, while the $e_g$-shell is empty, hence a so-called low-spin solution is obtained. Since there is only one way to have this configuration, the ground state has no degeneracy. When $\hat{H}$ includes crystal-field splitting and $\hat{H}_U$, there is a competition between crystal-field splitting, favoring a low-spin solution, and $\hat{H}_U$, favoring a high-spin solution. For the materials in paper III, all solutions are high-spin. For Fe in FeO, this means that one spin channel is full, and the remaining electron occupy the $t_{2g}$ orbitals with the opposite spin. To analyze the system, let us consider the orbitals $|d_1\rangle = \frac{1}{\sqrt{2}}(-|d_{xz}\rangle - i|d_{yz}\rangle)$, $|d_{xy}\rangle$ and $|d_{-1}\rangle = \frac{1}{\sqrt{2}}(|d_{xz}\rangle - i|d_{yz}\rangle)$ to represent the $t_{2g}$-shell. They have a projected angular momentum along the $z$ direction of $-1, 0$ and 1, respectively. It is therefore natural to introduce a pseudo angular momentum of $\acute{L}=1$ for the $t_{2g}$-shell [120–122]. We can now apply the same reasoning as above, when the Hamiltonian only contained $\hat{H}_U$, but instead of using $S$ and $L$, we use $S$ and $\acute{L}$. For Fe, with $S=2$ and $\acute{L}=1$, this means the lowest eigenenergy will have a degeneracy of $(2S+1)(2\acute{L}+1) = 15$. A small SOC term will further split these states into groups with different pseudo total angular momentum $\acute{J}$. In the case of Fe, the different $\acute{J}$ are $1, 2$ and 3 [121]. The lowest states have $\acute{J}=1$ and degeneracy $2\acute{J}+1 = 3$. There are 5 (al-

---

[2] The square of the orbital angular momentum operator $\hat{\boldsymbol{L}}^2$ can be written as $\hat{L}^z\hat{L}^z + 1/2(\hat{L}^+\hat{L}^- + \hat{L}^-\hat{L}^+)$. For a $(l,m)$-shell, $\hat{L}^z = \sum_{m=-l}^{l}\sum_\sigma m\hat{c}^\dagger_{l,m,\sigma}\hat{c}_{l,m,\sigma}$, $\hat{L}^+ = \sum_{m=-l}^{l-1}\sum_\sigma \sqrt{(l-m)(l+m+1)}\hat{c}^\dagger_{l,m+1,\sigma}\hat{c}_{l,m,\sigma}$, and $\hat{L}^- = (\hat{L}^+)^\dagger$. Hence for a many body state $|\Psi\rangle$, the expectation value $\langle\Psi|\hat{\boldsymbol{L}}^2|\Psi\rangle$ can be evaluated as $\langle\Psi_1|\Psi_1\rangle + 1/2(\langle\Psi_2|\Psi_2\rangle + \langle\Psi_3|\Psi_3\rangle)$, with $|\Psi_1\rangle = \hat{L}^z|\Psi\rangle$, $|\Psi_2\rangle = \hat{L}^-|\Psi\rangle$, and $|\Psi_3\rangle = \hat{L}^+|\Psi\rangle$. The reasoning for $\hat{\boldsymbol{S}}^2$ is analogous [14].

**Table 3.1.** *Eigenstate information of the four studied materials. Only states relevant at 300 K are shown. Calculated eigenenergies (in meV) with (approximate) degeneracies, pseudo total (orbital) angular momentum* $\acute{J}$ *(*$\acute{L}$*), expected Hund's rule values of* $S$ *and* $L$ *for an atom without SOC, and expectation values* $\langle S_z \rangle$ *and* $\langle L_z \rangle$ *of the 3d-shell from the impurity model calculations.*

| | $E-E_0$ | degen. | $\acute{J}$ | $\acute{L}$ | $S$ | $L$ | $\langle S_z \rangle$ | $\langle L_z \rangle$ |
|---|---|---|---|---|---|---|---|---|
| MnO | 0 | 6 | 5/2 | 0 | 5/2 | 0 | $\pm1.5, \pm0.7, \pm0.5$ | $6 \times 0$ |
| FeO | 0 | 3 | 1 | 1 | 2 | 2 | $\pm1.4, 0$ | $\pm0.6, 0$ |
| FeO | $\approx 30$ | 5 | 2 | 1 | 2 | 2 | $\pm0.7, 3 \times 0$ | $\mp0.3, 3 \times 0$ |
| FeO | $\approx 75$ | 7 | 3 | 1 | 2 | 2 | $\pm0.8, \pm0.1, 3 \times 0$ | $\mp0.4, \mp0.1, 3 \times 0$ |
| CoO | 0 | 2 | 1/2 | 1 | 3/2 | 3 | $\pm0.8$ | $\pm0.6$ |
| CoO | $\approx 50$ | 4 | 3/2 | 1 | 3/2 | 3 | $\pm0.4, \pm0.4$ | $\pm0.2, \mp0.2$ |
| CoO | $\approx 140$ | 6 | 5/2 | 1 | 3/2 | 3 | $\pm1.0, \pm0.5, \pm0.2$ | $\mp0.7, \mp0.6, \mp0.5$ |
| NiO | 0 | 3 | 1 | 0 | 1 | 3 | $\pm0.9, 0$ | $\pm0.4, 0$ |

most) degenerate eigenstates above the lowest eigenenergy with $\acute{J} = 2$. Above those, a second group of excited states have $\acute{J} = 3$ and consists of 7 (almost) degenerate states. Hybridization with the bath is the last missing term in the Hamiltonian in Eq. (3.26). This term has small influence on the eigenstates contributing to the thermal ground states, and their energies.

After parameterizing the impurity model Hamiltonian in Eq. (3.26) using non-spin polarized DFT calculations, the impurity calculations of FeO result in excited eigenenergies that are about 30 meV and 75 meV (respectively for $\acute{J} = 2$ and $\acute{J} = 3$) above the lowest eigenstate. These states will therefore be thermally populated at room temperature. With similar considerations as above, applied for the other materials, we obtain Table 3.1.

After the eigenstates have been calculated we can calculate their XA spectra. In Fig. 3.4 the $L_{2,3}$ spectra of FeO are shown and resolved into the three different $\acute{J}$ values. Since the lineshapes are rather different and the states differ only a few $k_B T$ from each other (with $T \approx 300$ K), one can expect changes of the Boltzmann averaged spectrum by varying the temperature. Theoretical isotropic XA spectra of MnO, FeO, CoO and NiO are presented in paper III. As the number of bath states used to represent the hybridization function increases, a higher accuracy is expected. According to Fig 3.5, where the number of bath states per impurity orbital is increased from zero to three, changes in the line shapes are moderate, with a few exceptions. For example, in NiO the small peak around 859 eV is absent without any bath states. This is because this peak corresponds to a charge transfer process.

In paper III, we used two different DFT functionals, one with a warped LDA potential and the other with the full LDA potential. A warped potential is designed to be spherical inside the MT sphere, and was suggested in Ref. [108] as a way to avoid double counting the non-spherical part of the Coulomb in-

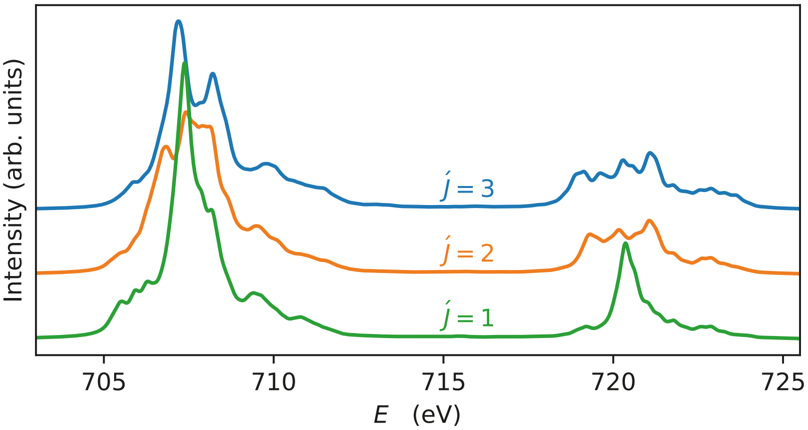

*Figure 3.4.* XA $L_{2,3}$ spectra of FeO, resolved in the lowest energy eigenstate groups and labeled by $\acute{J}$. Three bath states per impurity orbital are considered.

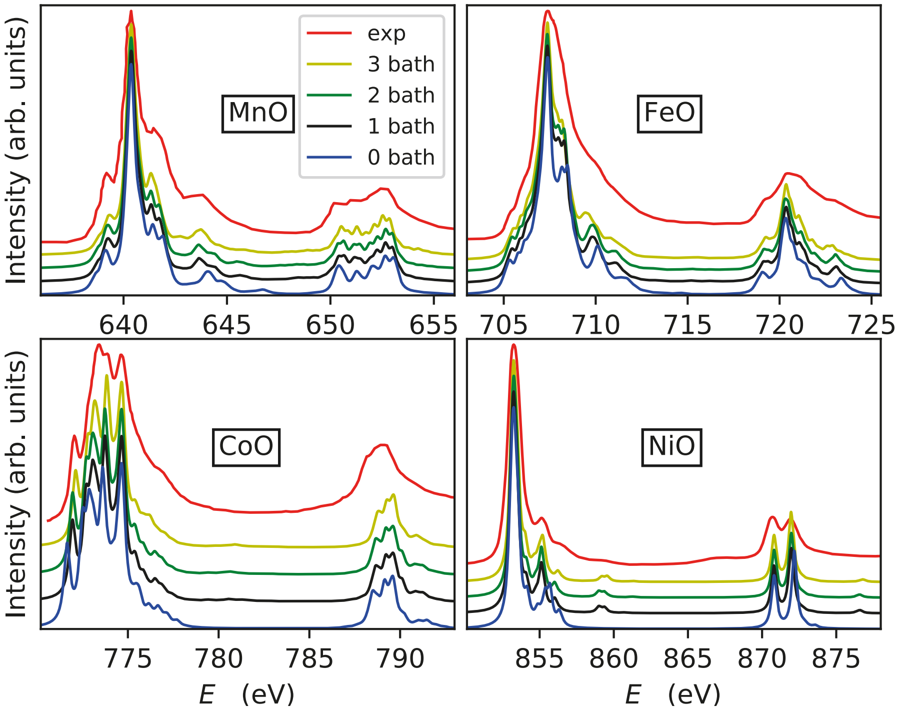

*Figure 3.5.* Computed XA $L_{2,3}$ spectra for four different number of bath states per impurity orbital. Experimental spectra (red curves) of MnO [123], FeO [124], CoO [125], and NiO [126] are included for comparison.

teraction. In practice the main difference in the band structure between the two potentials is that using the warped potential results in higher crystal field splitting. By comparing the XA spectra with the experimental spectra, some features are in better agreement when using the warped potential.

The effect of the presence of a core-hole is also investigated. By considering a core-hole in the DFT calculations (using a supercell), its effect on the valence electronic structure is determined. The hybridization functions of the four TMs decrease and the Slater-Condon parameters increase up to 17% due to the presence of the core-hole. The changes of the XA spectra when including these effects are seen in paper III.

In summary, a DFT+MLFT approach for calculating $L_{2,3}$-edge XA spectra is presented in paper III and applied to MnO, FeO, CoO, and NiO. Good agreement with experiment is obtained. For a more accurate description of the hybridization function, a combination of DFT and DMFT can be used [106].

## 3.4 Atomic-plane resolution of strained $CaTiO_3$

In this ongoing project, Ti and Ca $L_{2,3}$-edge EELS spectra with atomic-plane resolution are measured across an interface of $CaTiO_3$/$SrTiO_3$. As mentioned in the introduction of this chapter, the spectra of EELS and XAS coincide if an EELS setup, with very high kinetic energy electrons and small scattering angles, is used. Theoretical calculations of the Ti $L_{2,3}$-edge have been performed, using DFT combined with MLFT [108, 112]. The hybridization between the $3d$ orbitals with their surrounding is treated with one bath orbital per Ti $3d$-orbital, and a nominal occupation of $d^0$ is used. Due to the different lattice parameters of Ca and Sr, a lattice strain is present, distorting the local octahedral environment at the Ti site. In Fig. 3.6, theoretical Ti $L_{2,3}$-edge spectra are shown. The linear polarization dependence is due to the local distortion and has important implications, as we will discuss later. The four main absorption peaks in the electron energy-loss spectra can be understood already from a single-particle picture with a perfect octahedral environment [108] as the transitions $2p_{3/2} \rightarrow t_{2g}, 2p_{3/2} \rightarrow e_g, 2p_{1/2} \rightarrow t_{2g}$, and $2p_{1/2} \rightarrow e_g$. The single-particle picture predicts a decreasing spectral intensity as the photon energy is increased, with expected relative intensities 6,4,3, and 2, respectively. However, the Coulomb interaction mixes the spectral intensity from the $p_{1/2}$ and $p_{3/2}$ edges and, in agreement with observations, gives the opposite trend. The distortion of the local octahedral environment of the Ti atoms splits up both the $e_g$ and the $t_{2g}$ sets, and in the calculations the local symmetry is treated as $D_{4h}$. The crystal-field parameters $\bar{\varepsilon}_d = 3.029$ eV, $Dq = 0.144$ eV, $Ds = -0.064$ eV, and $Dt = -0.033$ eV and the hybridization parameters $\bar{\varepsilon}_b = -2.48$ eV, $Dq_b = 0.13$ eV, $V_{a_{1g}} = 4.2$ eV, $V_{b_{1g}} = 3.7$ eV, $V_{e_g} = 2.5$ eV and $V_{b_{2g}} = 2.3$ eV are obtained from the projected density of states and by discretizing the hybridization function [112]. The calculated spin-orbit parameters are $\zeta_{2p} = 3.83$ eV and $\zeta_{3d} = 0.03$ eV. The anisotropic Slater integrals $F^2_{pd}, G^1_{pd}$ and $G^3_{pd}$ are assumed to be unscreened and $F^2_{dd}$ and $F^4_{dd}$ to be screened with factors 0.82 and 0.88, respectively. The Slater integral value $F^0_{dd} = 6.3$ eV [114] is not calculated but determined from core-level x-ray photoemission spectra, the Slater integral value $F^0_{pd} = 8.2$ eV is set by the empirical rule $F^0_{pd} \approx 1.3F^0_{dd}$ [106, 108, 114], and the correction of the bare charge-transfer energy $\delta_{\mathrm{CT}} = 1.5$ eV is taken from Ref. [112]. A Lorentzian broadening of 0.4 eV (FWHM) is used for the core-hole lifetime and a Gaussian broadening of 1.2 eV (FWHM) is used to account for experimental broadening. Notice that there are different crystal field notations and the conversion between the crystal field parameters $\{Dq, Dt, Ds\}$ and $\{\Delta_d, \Delta_{e_g}, \Delta_{t_{2g}}\}$ , where $\Delta_d$ indicates the splitting between the $e_g$ and the $t_{2g}$-shell, $\Delta_{e_g}$ the splitting between $d_{x^2-y^2}$ and $d_{z^2}$ orbitals, and $\Delta_{t_{2g}}$ the splitting between $d_{xy}$ and $\{d_{yz}, d_{xz}\}$ orbitals, can be written as

$$\begin{aligned} \Delta_d &= 10Dq - \frac{35}{6}Dt \\ \Delta_{e_g} &= 4Ds + 5Dt \\ \Delta_{t_{2g}} &= 3Ds - 5Dt. \end{aligned} \tag{3.27}$$

The distortion, splitting both the $e_g$ set and the $t_{2g}$ set, results in the polarization dependent spectra, reported in Fig. 3.6. Using these spectra and a combined Bloch-waves/multislice method [127], a Ti $L_{2,3}$-edge spectrum can be calculated also at a Ca-O plane, see Fig. 3.7. This spectrum, compared to the spectrum at the Ti-O$_2$ plane, is not just lower in intensity, but there are also changes in the line-shape. These changes are in fact due to the polarization dependence. Preliminary experimental spectra [128], shown in Fig. 3.8, qualitatively agree with the theoretical results. In particular, the second peak has lower relative intensity at the Ca-O plane compared to the Ti-O$_2$ plane.

**Convergence of theoretical spectra**

Here follows a short discussion on the many body ground state, as well as some technical considerations for calculating the spectra. The ground state can be expressed as a linear combination of many Slater determinants $|\Psi\rangle = \sum_i c_i |i\rangle$, where $|i\rangle$ represents a Slater determinant. We can group the determinants according to the number of holes in the bath orbitals: $d^0\underline{b}^0$, $d^1\underline{b}^1$, $d^2\underline{b}^2$, $d^3\underline{b}^3$, $d^4\underline{b}^4$, .... The corresponding weights for each of these groups are shown in Fig 3.9. Using one bath orbital per impurity orbital, the number of all possible configurations for the group with $n_{\underline{b}}$ bath holes is $\binom{10}{n_{\underline{b}}}^2$, and according to Fig 3.9 we see that all determinants contribute for small $n_{\underline{b}}$. The small weights for configurations with high $n_{\underline{b}}$ justifies restricting the number of possible bath holes for computational speed up, without sever loss of accuracy. In Fig. 3.10, the XA spectra for different values of the maximum allowed number of bath holes, $n_{\underline{b}}^{\max}$, are shown, and compared with the unrestricted CI spectrum.

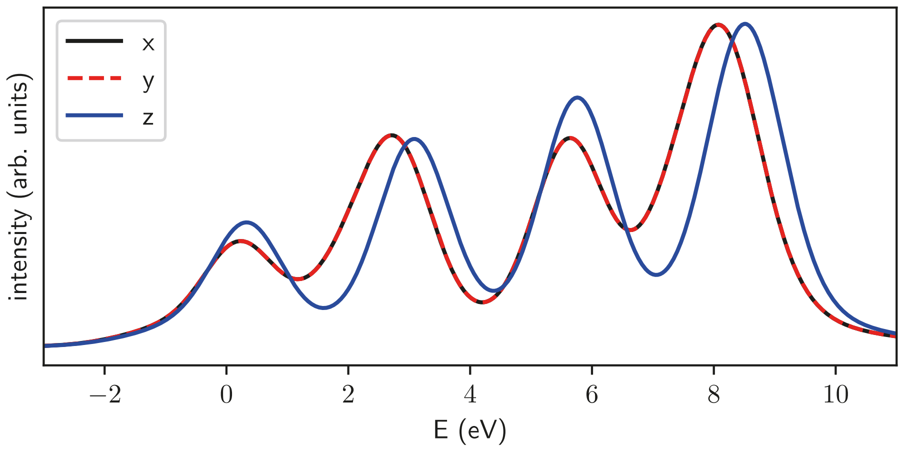

*Figure 3.6.* Theoretical Ti $L_{2,3}$-edge spectra of strained $CaTiO_3$, resolved in $x, y$ and $z$ polarizations.

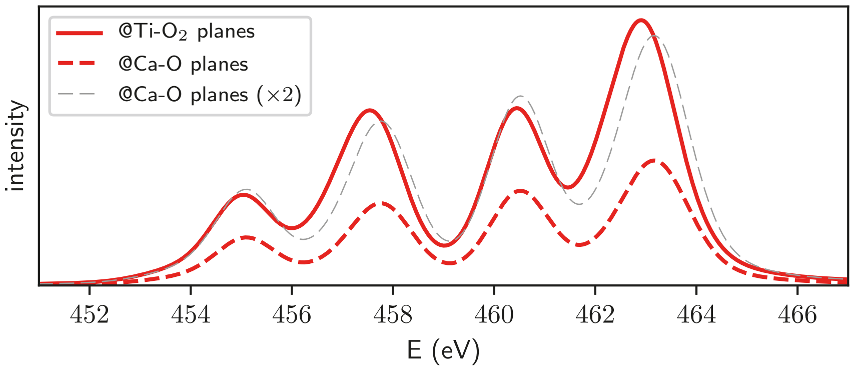

*Figure 3.7.* Theoretical Ti $L_{2,3}$-edge spectra of strained $CaTiO_3$.

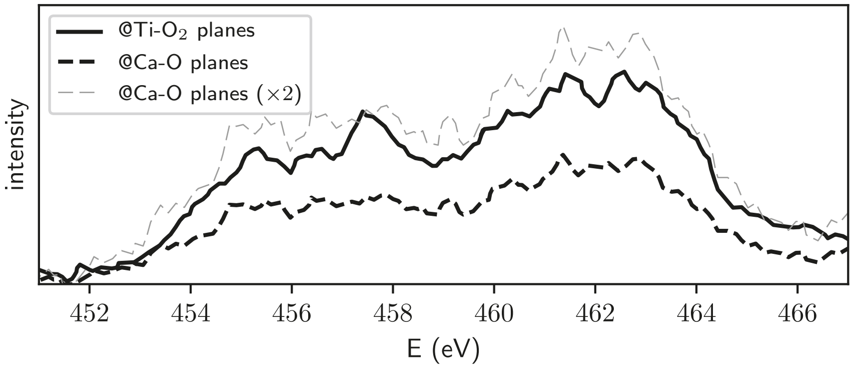

*Figure 3.8.* Preliminary experimental Ti $L_{2,3}$-edge spectra of strained $CaTiO_3$.

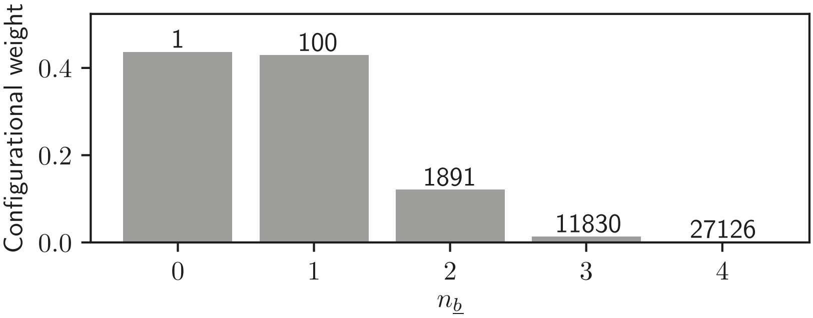

*Figure 3.9.* Configurational weights of the many body ground state of the Ti impurity model, resolved in the number of holes in the bath orbitals. The number on top of the bars indicate how many Slater determinants contribute to the ground state. One bath orbital per impurity orbital was used.

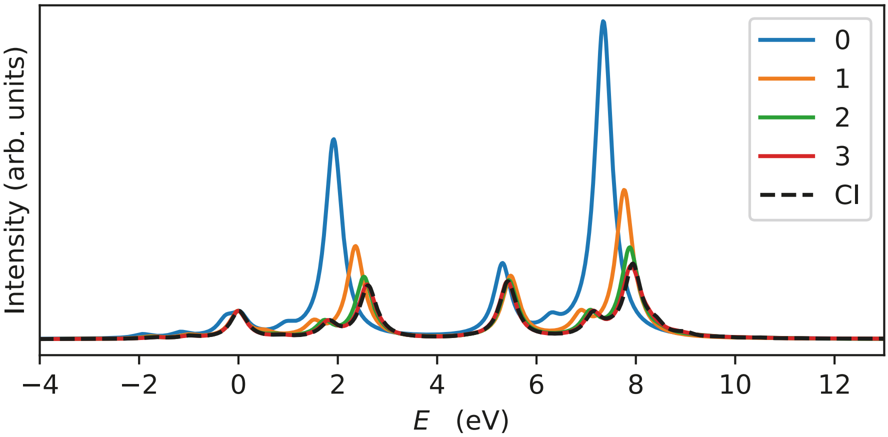

*Figure 3.10.* Ti $L_{2,3}$ spectra for polarization in the $x$ direction. Different values of the configurational restriction parameter $n_{\underline{b}}^{\max}$ are used. As $n_{\underline{b}}^{\max}$ increases the spectra converge to the CI spectrum. No experimental broadening is applied.

## 3.5 Mo doped $LaFeO_3$

This section is a summary of the theoretical XAS results obtained in paper IV. The studied system is $LaFe_{1-x}Mo_xO_3$ with a maximum Mo concentration of $x = 0.25$. The undoped system (i.e. $x = 0$) is insulating and antiferromagnetic (AFM). However, with Mo doping, charge disproportionation among the Fe-sites develops, as well as metallicity, while the AFM order is preserved. The calculations of the XA spectra are based on the same combined approach discussed above. The theoretical $L_{2,3}$-edge calculations of Fe are performed at 0% and 25% Mo doping. The Fe sites are treated with $D_{4h}$ symmetry. The hybridization is modelled with two bath orbitals per Fe 3d-orbital. One of them is assumed to be fully occupied, while the other one is assumed to be completely empty before covalency. The Fe sites before covalency are considered to be $d^6$. One difference with the other projects in this thesis is that the double counting here is determined such that the $3d$ occupations in the impurity calculations match the occupations obtained in DFT+$U$. This is an approximate attempt to improve the charge disproportionation description from pure DFT. To calculate the spectra using a more accurate method, such as DFT+DMFT would be a natural and interesting future project. At 25% Mo, there are three inequivalent Fe-sites in the computational unitcell. Two of those sites have similar local environment as in the undoped system, while the third Fe-site has a more distorted local environment. Corresponding DFT+$U$ occupations are 5.4 and 5.7, respectively. The MT localized orbitals (see section 2.5.1) are used in this project. They typically give smaller occupations compared to the ORT orbitals. In the supplementary information of paper IV the theoretical XA spectra are compared to the experimental spectra. In the case of 25% Mo doping, the total XA spectrum consists of a sum over all three Fe-sites. Two distinct spectra are obtained with a difference between the two maximum peak positions, similar to the maximum peak position difference between $Fe^{+3}$ and $Fe^{+2}$ spectra in Ref. [129].

# 4. Analytical continuation

This chapter discusses analytical continuation of fermionic and bosonic Green's functions and self-energies. The main focus is on fermionic single-particle Green's functions. In the introduction chapter, the analytical continuation was described mathematically as a technique to extend the domain of a given analytical function in the complex plane. In the field of DMFT, this extension is typically from Matsubara frequency points to the upper half of the complex plane. Most interesting are function values on the real axis, containing dynamical information on the studied system. Also note that, once the function is known on the real axis, the corresponding spectral function is also trivially known, due to Eq. (1.35), and thus the function is known everywhere in the complex plane, according to Eq. (1.24).

The analytical continuation problem of going from imaginary to real frequency can be tackled in three ways. One approach of doing analytical continuation is possible only if an analytical expression of the function is known. Then the analytical continuation simply means changing argument from $i\nu_n$ to $\omega + i\delta$. Note this trivial way requires the function be given as a rational function [45]. For example, if one takes Eq. (1.20) and replaces $i\nu_n$ with $\omega + i\delta$ the continuation to the real axis would be completely wrong. Another approach is to generalize the domain of the function of interest by fitting a parameterized function ansatz to the Matsubara frequency data. The obtained function is then evaluated on the real axis. The Padé approximant method, described in section 4.6, does exactly this. The third and last approach directly calculates the spectral function by solving an integral equation. If the input is represented by Matsubara frequency data, this means solving Eq. (1.23). For imaginary time input data for a fermionic Green's function, instead, Eq. (1.25) has be solved. This kind of integral equations are known as Fredholm integral equations of the first kind and are discussed below. How to solve the Fredholm equation, using non-negative least-squares method, non-negative Tikhonov method, maximum entropy method and stochastic optimization method, is discussed in sections 4.2, 4.3, 4.4 and 4.5 respectively. See Fig. 4.1 for a summary of the discussed methods for analytical continuation.

Due to the similarities of the analytical properties of fermionic Green's functions and self-energies, it is easy to rescale the self-energy to the form of a Green's function. Thus the methods for doing continuations of fermionic Green's functions can be used also for self-energies. A self-energy can be written as $\Sigma(z) = \Sigma_\infty + \Sigma_D(z)$, where $\Sigma_\infty \in \mathbb{R}$ is the asymptotic value that the self-energy has for $|z| \in \infty$. The dynamical part $\Sigma_D(z)$ only differs from a

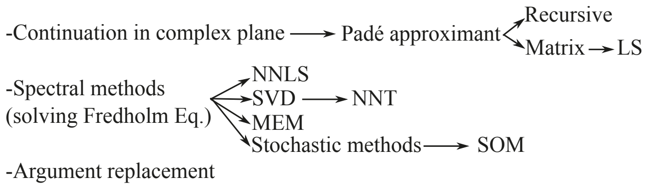

*Figure 4.1.* Classification diagram of the analytical continuation methods discussed in the text.

Green's function by its asymptote. Instead of decaying as $1/z$ it decays as $s/z$ with $s \in \mathbb{R}$ [130]. By diving the Matsubara frequency data by $s$, the dynamical part of the self-energy can be treated as a fermionic Green's function. Once the continuation is done, one can rescale the function values by $s$. Therefore we only discuss fermionic and bosonic Green's function below, unless explicitly saying otherwise.

## 4.1 Fredholm equation

The analytical continuation can be done by solving a Fredholm equation of the first kind:

$$f(y) = \int d\omega k(y,\omega)\rho(\omega), \tag{4.1}$$

where $\rho(\omega)$ is the desired function, $f(y)$ is the input data and $k(y,\omega)$ is a known integral kernel. In our case the spectral function is $\rho$, $f$ represents the Matsubara Green's function and the shape of the kernel $k(x,y)$ will depend on which Matsubara representation is used and whether $f$ is a fermionic or bosonic function. The goal will be to numerically solve Eq. (4.1) with the help of any a priori knowledge. There are many numerically methods for solving the Fredholm equation. We will discuss four different methods in sections 4.2, 4.3, 4.4 and 4.5 respectively.

The Fredholm equation arises in many fields of science and engineering [131]. According to Hadamard [131, 132], there are three properties to classify Fredholm equations. The first is the existence of a solution, the second is the uniqueness of a solution and the third is the continuous dependence of the solution on the input data. Continuous dependence means that a small change of the input data will cause small changes in the solution. To have a well-defined problem all three properties have to be fulfilled, otherwise the problem is called ill-posed. Solving the Fredholm equation of the first kind is considered an ill-posed problem [132]. Assuming that the function $\rho$ was given, any sharp feature would be washed out during the integration to generate $f$ from Eq. (4.1). This also means that, given $f$, it is hard to extract $\rho$ since many $\rho$ give similar $f$. As pointed out in [133] and proven in [132], the ill-posedness is due to the infinite dimensional space which $\rho$ belongs to, and not to the shape of the kernel. In fact there are infinitely many solutions to Eq. (4.1) for a finite set of values $f_i = f(y_i)$ [134]. Stochastic noise on the input data makes the analytical continuation even harder.

### 4.1.1 Kernels

The Matsubara Green's function can be represented in imaginary time, imaginary frequency or by Legendre polynomials. All these representations have corresponding kernels. The kernels are also different depending on the bosonic or fermionic character of the Green's function. The non-negative property for the spectral function significantly reduces the domain for the solution to find, which helps when solving the Fredholm equation. Since the non-negativity is a property of the fermionic spectral function, see Eq. (1.32), it is easy to enforce. For bosons, with the property in Eq. (1.33), an effective spectral function is usually introduced, let us denote it as $\tilde{\rho}$, that satisfies the non-negative property. For convenience it may be useful to work with normalized spectral functions integrating to one. Fermionic spectral functions normalize to one, see Eq. (1.38), but bosonic spectral functions do not. Therefore, an effective spectral function normalized to one is introduced in the bosonic case. For a system with particle-hole symmetry, fermionic k-integrated spectral functions are even ($\rho(\omega) = \rho(-\omega)$). For bosonic operators with $\hat{A} = \hat{B}^\dagger$ and hermitian symmetry ($\hat{B} = \hat{B}^\dagger$), the bosonic spectral functions are odd ($\rho(\omega) = -\rho(-\omega)$), according to Eq. (1.31). These spectral symmetries help in the analytical continuation and are included by modifying the kernels.

### 4.1.2 Imaginary frequency

The expression for doing analytical continuation from imaginary frequencies is found in Eq. (1.23). This is true for both fermions and bosons. To fulfil the non-negativity we introduce $\tilde{\rho}(\omega) = \rho(\omega)/\omega$ and solve the Fredholm equation for $\tilde{\rho}$ in the bosonic case. Once the solution is found one transforms back to get $\rho$. The kernels thus become:

$$k_n(\omega) = \frac{1}{i\nu_n - \omega}\,, \quad \text{for fermions} \tag{4.2}$$

$$k_n(\omega) = \frac{\omega}{i\nu_n - \omega}\,, \quad \text{for bosons.} \tag{4.3}$$

To work with a normalized bosonic spectral function, one can introduce $\tilde{\rho}(\omega) = \frac{1}{-\chi_0}\frac{\rho(\omega)}{\omega}$ which makes the kernel look like

$$k_n(\omega) = \frac{-\chi_0\omega}{i\nu_n - \omega}, \tag{4.4}$$

where $\chi_0$ is the bosonic Green's function at the Matsubara point $\nu = 0$. Let us hereafter separate fermionic and bosonic Green's functions by using the letters $G$ and $\chi$ respectively.

**Even (odd) symmetry**
For even (odd) fermionic (bosonic) spectral functions the integral in Eq. (1.23) can be rewritten such that the left integration limit is changed from $-\infty$ to 0. Furthermore the real (imaginary) part of the Matsubara Green's function becomes zero for fermions (bosons). The Fredholm equations, including the kernels, become:

$$\mathrm{Im}[G_n] = \int_0^\infty d\omega \frac{-2\nu_n}{\nu_n^2 + \omega^2}\rho(\omega)\ , \ \text{for fermions} \tag{4.5}$$

$$\mathrm{Re}[\chi_n] = \int_0^\infty d\omega \frac{-2\omega}{\nu_n^2 + \omega^2}\rho(\omega)\ , \ \text{for bosons.} \tag{4.6}$$

Halving the integration limits reduces the integral of the fermionic spectral function to $1/2$. To work with normalized spectral functions, one can introduce $\tilde{\rho}(\omega) = 2\rho(\omega)$ and $\tilde{\rho}(\omega) = \frac{2}{-\chi_0}\frac{\rho(\omega)}{\omega}$ in the fermionic and bosonic case respectively. The kernels then read:

$$k_n(\omega) = \frac{-\nu_n}{\nu_n^2 + \omega^2}\ , \ \text{for fermions} \tag{4.7}$$

$$k_n(\omega) = \frac{\chi_0\omega^2}{\nu_n^2 + \omega^2}\ , \ \text{for bosons.} \tag{4.8}$$

### 4.1.3 Imaginary time

The expression for the imaginary time Green's function is found in Eq. (1.25). The imaginary time kernels have the form:

$$k_\tau(\omega) = \frac{-e^{-\tau\omega}}{1 \pm e^{-\beta\omega}}, \tag{4.9}$$

where $+$ $(-)$ is for fermions (bosons). To obey the non-negativity condition we introduce $\tilde{\rho}(\omega) = \rho(\omega)/\omega$ and solve the Fredholm equation for $\tilde{\rho}$ in the bosonic case. The bosonic kernel for $\tilde{\rho}$ is thus

$$k_\tau(\omega) = \frac{-\omega e^{-\tau\omega}}{1 - e^{-\beta\omega}}. \tag{4.10}$$

One way of normalizing the spectral function to one is to work with the effective spectral function $\tilde{\rho}(\omega) = \frac{1}{-\chi(\tau=0^+)}\frac{\rho(\omega)}{1-e^{-\beta\omega}}$, which has the corresponding modified kernel

$$k_\tau(\omega) = \chi(\tau = 0^+)e^{-\tau\omega}. \tag{4.11}$$

The effective spectral function $\tilde{\rho}$ has the desired normalization, which can be seen by studying the limit $\tau \to 0^+$.

**Even (odd) symmetry**
For even (odd) fermionic (bosonic) spectral functions Eq. (4.9) can simplified to

$$G(\tau) = \int_0^\infty d\omega \frac{-\cosh\left(\left(\frac{\beta}{2}-\tau\right)\omega\right)}{\cosh\left(\frac{\beta}{2}\omega\right)}\rho(\omega)\ , \ \text{for fermions} \tag{4.12}$$

$$\chi(\tau) = \int_0^\infty d\omega \frac{-\cosh\left(\left(\frac{\beta}{2}-\tau\right)\omega\right)}{\sinh\left(\frac{\beta}{2}\omega\right)}\rho(\omega)\ , \ \text{for bosons.} \tag{4.13}$$

If spectral function normalization is desired, we can change to $\tilde{\rho}(\omega) = 2\rho(\omega)$ for fermions and $\tilde{\rho}(\omega) = \frac{1}{-\chi_{0^+}} \coth\frac{\beta}{2}\omega\rho(\omega)$ for bosons, resulting in kernels:

$$k_\tau(\omega) = \frac{-\cosh\left(\left(\frac{\beta}{2}-\tau\right)\omega\right)}{2\cosh\left(\frac{\beta}{2}\omega\right)}\ , \ \text{for fermions} \tag{4.14}$$

$$k_\tau(\omega) = \frac{-\chi_{0^+}\cosh\left(\left(\frac{\beta}{2}-\tau\right)\omega\right)}{\cosh\left(\frac{\beta}{2}\omega\right)}\ , \ \text{for bosons.} \tag{4.15}$$

### 4.1.4 Legendre polynomials

In the context of DMFT, CTQMC is a popular impurity solver which samples the fermionic Green's function $G(\tau)$ [135]. Instead of directly measuring $G(\tau)$, in CTQMC one can also expand $G(\tau)$ in a basis of Legendre polynomials $P_l(x)$ defined on the intervall $[0,\beta)$ [136]:

$$G(\tau) = \sum_{l=0}^{\infty} G_l \frac{\sqrt{2l+1}}{\beta} P_l(2\tau/\beta - 1). \tag{4.16}$$

Then one can directly sample the coefficients

$$G_l = \sqrt{2l+1}\int_0^\beta d\tau P_l(2\tau/\beta - 1)G(\tau). \tag{4.17}$$

To make a direct connection between $G_l$ and the spectral function $\rho(\omega)$, we combine Eq. (4.16) and Eq. (1.25) and use the orthogonality of the Legendre polynomials by multiplying with $P_l'$ and integrating over $[0,\beta)$. To get rid of the remaining integral over $\tau$ we also use: $\int_{-1}^{1} dx P_l(x) e^{-ax} = 2i^l j_l(ia)$, where $j_l$ is the spherical Bessel function. This gives us a new analytical continuation kernel

$$k_l(\omega) = \frac{-\sqrt{2l+1}\beta i^l e^{-\beta\omega/2} j_l(i\beta\omega/2)}{1+e^{-\beta\omega}} \tag{4.18}$$

and the corresponding integral equation

$$G_l = \int_{-\infty}^{\infty} d\omega k_l(\omega)\rho(\omega). \tag{4.19}$$

The spectral function can thus be calculated using the Legendre coefficients $G_l$. Even though the kernel expression in Eq. (4.18) has imaginary numbers, $k_l \in \mathbb{R}$. The kernel $k_l(\omega)$ is even (odd) for even (odd) $l$. Furthermore, for even $l$, $k_l(\omega)$ is non-positive. Particle-hole symmetry thus simply implies that $G_l = 0$ for all odd $l$. This kernel was not used in any of the papers but is described here to offer a more complete picture of possible analytical continuation kernels.

### 4.1.5 Complex decomposition

For any kernel $k(\omega) \in \mathbb{C}$ and input data $f(y) \in \mathbb{C}$ we can use the linearity of the Fredholm equation and the fact that $\rho \in \mathbb{R}$ to obtain separate equations for the real and the imaginary parts:

$$
\begin{aligned}
f(y) = f_r(y) + i f_i(y) = \int dx k(y,x)\rho(x) = \int dx (k_r(y,x) + i k_i(y,x))\rho(\omega) \\
\Rightarrow \begin{cases} f_r(y) = \int dx k_r(y,x)\rho(x) \\ f_i(y) = \int dx k_i(y,x)\rho(x) \end{cases}
\end{aligned}
\tag{4.20}
$$

This allows working with real numbers when solving the Fredholm equation.

## 4.2 Least squares

The least-squares (LS) method is a computationally fast and simple method for solving the Fredholm Eq. (4.1). A finite number $M$ of input data $f_i = f(y_i)$ has to be chosen. Then the integral has to be approximated to reduce the problem to algebraic equations.

**Mesh discretization**

The first step is the discretization of the real-axis with a finite mesh defined on an energy window where the unknown spectral function is expected to have a finite weight. In the papers V and VI we use the trapezoidal rule and a logarithmic distribution of $N$ grid points to obtain a linear algebraic problem [137]:

$$
f_i = \sum_{j=1}^{N} \underbrace{w_j k_{i,j}}_{K_{i,j}} \rho_j \,, \quad \text{for } i = 1, 2, ..., M, \tag{4.21}
$$

where $w_j$ are the integration weights. Using vectors $\boldsymbol{f} \in \mathbb{R}^M$, $\boldsymbol{\rho} \in \mathbb{R}^N$ and matrix $K \in \mathbb{R}^{M \times N}$, Eq. 4.21 takes the form

$$
\boldsymbol{f} = K\boldsymbol{\rho}, \tag{4.22}
$$

where $K_{i,j}$ includes both $w_j$ and $k_{i,j}$. An alternative discretization method is to use a basis to represent the spectral function, $\rho(x) = \sum_i \rho_i b_i(x)$, which results

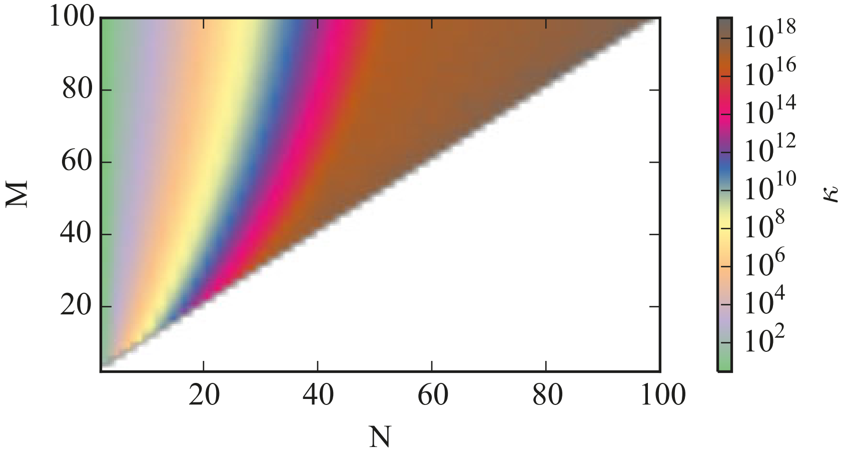

*Figure 4.2.* Condition number of kernel matrix, varying number of real-axis points $N$ and number of input data $M$ ($\frac{M}{2}$ Matsubara frequency points). Use the generalized condition number, see Eq. (4.36) and double precision with machine epsilon $\approx 2.2 \cdot 10^{-16}$.

in

$$f_i = \sum_j \rho_j \underbrace{\int dx k_i(x) b_j(x)}_{K_{i,j}}. \tag{4.23}$$

This expression can also be recast into Eq. (4.22). The fermionic spectral functions should normalize to one. Instead of explicitly enforcing this normalization, one can consider a Matsubara frequency point at high energy which, in absence of noise, will also enforce the normalization of the spectral function.

**Condition number**

The condition number is an estimate of the relative solution error of a linear equation, like Eq. (4.22), compared to a relative error in the input data. This has nothing to do with computational round-off errors but is a property of the matrix, telling how much the solution will change due to small change $\delta f$ in the input data. The condition number is defined as

$$\kappa(K) = ||K^{-1}||\, ||K||, \tag{4.24}$$

where $||\cdot||$ is the norm and $K^{-1}$ is the inverse of $K$. In case of $N \leq M$ and $K$ having full rank, let $K^{-1}$ denote the LS inverse, see Eq. (4.28). One can show [132], that the condition number gives an upper bound for the relative solution error:

$$\frac{||\delta \boldsymbol{\rho}||}{||\boldsymbol{\rho}||} \leq \kappa \frac{||\delta \boldsymbol{f}||}{||\boldsymbol{f}||}, \tag{4.25}$$

where $\delta\boldsymbol{\rho}$ is the solution of $K\delta\boldsymbol{\rho} = \delta\boldsymbol{f}$. Note that the condition number will depend on the discretization. A perhaps unintuitive fact for ill-posed problems, is that the denser real-axis mesh is used, hence a more precise integral discretization, the higher will the condition number be, thus making the solution less reliable [132]. This can be verified by a direct evaluation of the condition number. Let us consider the Matsubara frequency kernel in Eq. (4.2), choose the lowest $\frac{M}{2}$ Matsubara frequency points and discretize the real-axis with $N$ points from $-5$ to 5 using a logarithmic mesh. Since the kernel is complex, we get $M$ rows in the matrix kernel $K$. The condition number is shown in Fig. 4.2, where both $N$ and $M$ are varied. It is clear that $\kappa$ increases strongly with $N$. Another point worth noticing is that the condition number decreases as more Matsubara points are used, but this behaviour is weaker for many Matsubara points. Even though the condition number does not measure round-off errors, the double precision routines used artificially introduces a saturation in $\kappa$ around $10^{18}$ (see brown area). The problem clearly becomes more stable by using a small $N$. However the error introduced by discretizing the integral using the trapezoidal rule is $\mathscr{O}(N^{-2})$ [138], making a large $N$ a more accurate choice. A compromise is needed between stability and accuracy. Another remark about the real-axis discretization can be made with respect to Runge's phenomenon [139]. It states that interpolation with a polynomial of high degree on a uniform grid will create oscillations at the edges of the interpolation interval. Runge also showed that using a higher order polynomial does not imply a higher interpolation accuracy. In the context of analytical continuation, it means that using a dense real-axis mesh to represent the spectral function with many unknown coefficients may lead to oscillatory behaviour of the spectral function for high energy. A practical advise is to not use a denser mesh than the real-axis resolution one is interested in, and also test the discretization dependence on $\boldsymbol{\rho}$.

**Solving LS**

The next step after the mesh discretization is the LS minimization. The LS formulation of Eq. (4.22) is

$$\min_{\boldsymbol{\rho}} ||K\boldsymbol{\rho} - \boldsymbol{f}||_2^2, \tag{4.26}$$

where the subscript 2 stands for the $L^2$ norm (Euclidean norm). Setting the gradient with respect to $\rho$ to zero gives the normal equation

$$K^T K\boldsymbol{\rho} = K^T \boldsymbol{f}, \tag{4.27}$$

which always has a solution, although not necessarily unique. For a unique least-squares solution the matrix $K$ needs to have full rank [139]. Then an LS inverse can be defined as

$$K_{\mathrm{LS}}^{-1} = (K^T K)^{-1} K^T, \tag{4.28}$$

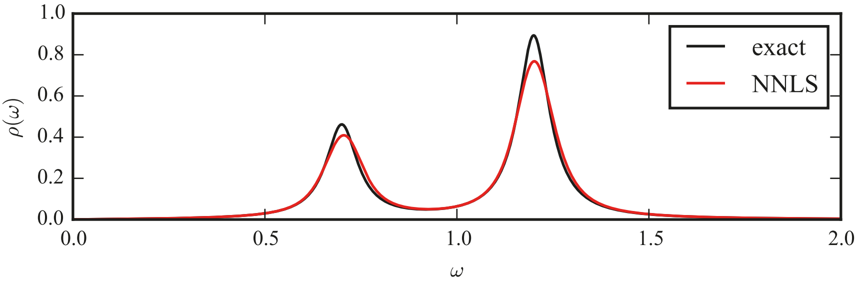

*Figure 4.3.* Spectral function of the susceptibility for simple two-pole model. NNLS is accurately recovering the two peaks in the presence of statistical Matsubara noise of the order of $10^{-4}$.

which is easily obtained from Eq. (4.27). However, for analytical continuation problems, $K$ is typically rank deficient, i.e. has a null-space, thus there are infinitely many least-squares solutions. The LS inverse in Eq. (4.28) does not exist and the condition number in Eq. (4.24) is infinite. To obtain a unique LS solution an extra condition is required; a common choice is to minimize the norm of $\boldsymbol{\rho}$.

### Non-negative property

The fermionic and bosonic symmetry of the spectral function, given by Eq. (1.32) and (1.33) respectively, help when performing analytical continuations by greatly reducing the solutions domain. In section 4.1.1 we showed that it is possible to modify the kernel to make the solution non-negative. This means that we, instead of Eq. (4.26), want to solve a non-negative least-squares (NNLS) problem:

$$\min_{0\leq\boldsymbol{\rho}} ||K\boldsymbol{\rho} - \boldsymbol{f}||_2^2. \tag{4.29}$$

The method for solving Eq. (4.29) is described in [140] and is referred to as the NNLS method. In practice it involves iteratively solving reduced least-squares problems. For simple spectral functions, using NNLS can give accurate analytical continuations. An example is the susceptibility of a two-pole model where NNLS almost perfectly reobtains the exact spectral function, as is shown in Fig. 4.3. However for more complicated spectra, NNLS is known to give sharp fictitious sawtooth spectra, which can be seen in paper VI and in Fig. 4.4. Another typical spectrum artefact from using the NNLS is the presence of spectral function values $\rho_i$ identical to zero. This is due to overfitting to the input data together with the non-negative constrain. However for simple spectra, consisting of a few well defined peaks, this method sometimes perform very well, which is also shown in paper VI. This unreliability and its

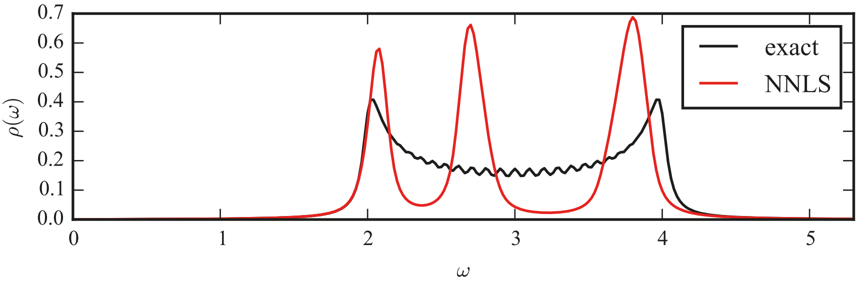

*Figure 4.4.* Spectral function of the susceptibility for a band-gap model. NNLS inaccurately gives a sharp sawtooth spectrum in the presence of statistical Matsubara noise of the order of $10^{-4}$.

instability to handle stochastic noise on the input data, leads us to investigate more robust methods, where regularizations typically are imposed on $\boldsymbol{\rho}$.

## 4.3 SVD and Tikhonov regularization

The singular value decomposition (SVD) and the Tikhonov regularization are two important methods for solving ill-posed problems. SVD can be used to solve the LS equations seen in section 4.2. It also provides a natural starting point for more robust methods, such as the Tikhonov method.

### 4.3.1 SVD

A matrix $K \in \mathbb{R}^{M \times N}$ can always be decomposed in the form

$$K = U \Sigma V^T, \tag{4.30}$$

where $U \in \mathbb{R}^{M \times M}$ and $V \in \mathbb{R}^{N \times N}$ are unitary matrices and $\Sigma \in \mathbb{R}^{M \times N}$ is diagonal with non-negative values $\sigma_i$, called singular-values. For $N \leq M$, $\Sigma$ has the shape:

$$\Sigma = \left[\begin{array}{ccccc} \sigma_1 & & & & \\ & \ddots & & 0 & \\ & & \sigma_r & & \\ & 0 & & \ddots & \\ & & & & \sigma_N \\ \hline & & 0 & & \\ & & & & \end{array}\right] \tag{4.31}$$

The columns $\boldsymbol{u}_i$ in $U$ make an orthonormal basis in $\mathbb{R}^M$ and the columns $\boldsymbol{v}_i$ in $V$ make an orthonormal basis in $\mathbb{R}^N$. A matrix with rank $r$ has $r$ non-zero singular-values $\sigma_i$. By using the SVD definition it is easy to show that

$$K\boldsymbol{v}_i = \sigma_i \boldsymbol{u}_i \text{ , for } i \in [1, \min(N,M)]. \tag{4.32}$$

Using this property and expanding in the SVD basis the input data $\boldsymbol{f}$ and the sought solution $\boldsymbol{\rho}$ in Eq. (4.22), one finds the solution

$$\boldsymbol{\rho} = \sum_{i=1}^{r} \sigma_i^{-1} (\boldsymbol{u}_i^T \boldsymbol{f}) \boldsymbol{v}_i. \tag{4.33}$$

This is actually nothing else than the minimum norm LS solution to Eq. (4.22). Thus the obtained $\boldsymbol{\rho}$ solves the normal equation in Eq. (4.27). Moreover if several solutions exist, $\boldsymbol{\rho}$ has the smallest norm of all solutions. This procedure can be done by using the LAPACK routine DGELSD [141], which is the approach used in paper V and VI. The Moore-Penrose pseudoinverse of $K$ is

$$K^+ = V\Sigma^+ U^T, \tag{4.34}$$

with $\Sigma^+ \in \mathbb{R}^{N\times M}$ being diagonal and having elements $\sigma_i^{-1}$ [142]. The minimum norm LS solution can now be formulated as

$$\boldsymbol{\rho} = K^+ \boldsymbol{f}. \tag{4.35}$$

For numerical computation, note that only the $r$ biggest singular-values $\sigma_i$ and their corresponding column vectors $\boldsymbol{u}_i$ and $\boldsymbol{v}_i$ are needed to calculate $\boldsymbol{\rho}$.

### 4.3.2 Condition number

Let us discuss the condition number in the language of SVD. The classical condition number in Eq. (4.24) is equal to $\sigma_{\max}/\sigma_{\min}$ in the $L^2$ norm and is infinite for a rank deficient matrix, since $\sigma_{\min} = 0$. Instead one can use the generalized condition number of a (possibly rank deficient) matrix to study the problem stability. It is defined as

$$\kappa(K) = ||K||_2 ||K^+||_2, \tag{4.36}$$

which is equivalent to $\kappa = \sigma_1/\sigma_r$ [142]. For a rank deficient matrix, thus having at least one singular value being zero, SVD will in practise not provide any singular values being zero due to round-off errors in the calculations. Instead the smallest calculated singular value will be of the order of the computers machine epsilon, hence artificially presenting $K$ as a full rank matrix. By studying the magnitude of the singular values, one can approximately determine which ones of them are non-zero due to round-off errors. The calculated singular-values to a rank deficient matrix, using double precision, is shown in Fig. 4.5. The rank of the matrix is about 50 since the 10 smallest singular values have values around the machine epsilon.

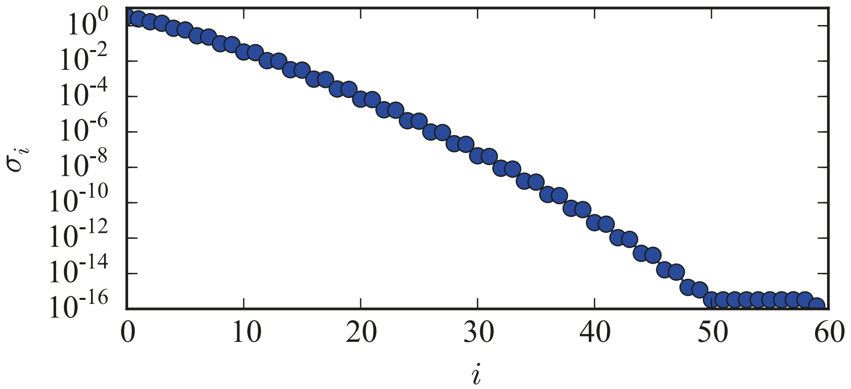

*Figure 4.5.* Singular values, in descending order, for kernel matrix with $N = 60$ real-axis points and $M = 80$ input values (40 Matsubara frequency points). Double precision with machine epsilon $\approx 2.2 \cdot 10^{-16}$ is used in for the SVD.

### 4.3.3 Truncated SVD

We see that small singular-values in Eq. (4.33) will have big impact on $\boldsymbol{\rho}$. To improve solution stability we can reduce the weight for small singular-values. Truncated SVD means we only use the $t < r$ biggest singular-values in the SVD expression in Eq. (4.33). This is a form of regularization which makes the solution $\boldsymbol{\rho}$ more stable to numerical noise. At what value $t$ one should cut the sum is hard to know a priori. To make the transition from included singular values to those not included less sharp Tikhonov smoothly filters the singular-values, see below.

### 4.3.4 Tikhonov regularization

Tikhonov regularization is one of the most used methods of regularization for ill-posed problems [132]. It can be interpreted as a process for filtering away the smallest singular values of the minimum norm LS solution in Eq. (4.33). The filter (called Wiener filter) has the form:

$$d(x,\alpha) = \frac{x^2}{x^2+\alpha^2} \tag{4.37}$$

The Tikhonov method therefore modifies Eq. (4.33) into

$$\boldsymbol{\rho} = \sum_{i=1}^{r} d(\sigma_i,\alpha)\sigma_i^{-1}(\boldsymbol{u}_i^T \boldsymbol{f})\boldsymbol{v}_i. \tag{4.38}$$

The regularization parameter $\alpha$ determines the value around which singular-values start to be filtered away. Another formulation of the Tikhonov method is given by the minimization problem [143]:

$$\min_{\rho} ||K\boldsymbol{\rho} - \boldsymbol{f}||_2^2 + \alpha^2 ||\boldsymbol{\rho}||_2^2. \tag{4.39}$$

By introducing a modified kernel matrix and input data vector

$$K' = \begin{bmatrix} \begin{bmatrix} \\ K \\ \\ \end{bmatrix} \\ \begin{bmatrix} \\ \alpha I \\ \\ \end{bmatrix} \end{bmatrix}, \ \boldsymbol{f}' = \begin{bmatrix} \begin{bmatrix} \\ \boldsymbol{f} \\ \\ \end{bmatrix} \\ \begin{bmatrix} \\ \boldsymbol{0} \\ \\ \end{bmatrix} \end{bmatrix}, \tag{4.40}$$

where $I$ is the identity matrix, Eq. (4.39) can be rewritten as

$$\min_{\rho} ||K'\boldsymbol{\rho} - \boldsymbol{f}'||_2^2. \tag{4.41}$$

This is simply a LS problem, but with modified $\boldsymbol{f}'$ and $K'$ [133]. To see that the solution to the minimization problem in Eq. (4.39) truly is the filtered SVD formula in Eq. (4.38), we can look at the normal equation to Eq. (4.41):

$$(K^T K + \alpha^2 I)\boldsymbol{\rho} = K^T \boldsymbol{f}. \tag{4.42}$$

Using SVD for the matrix $K$, the solution of Eq. (4.42) becomes:

$$\begin{aligned} \boldsymbol{\rho} &= V(\Sigma^T\Sigma + \alpha^2 I)^{-1}\Sigma^T U^T \boldsymbol{f} && (4.43) \\ &= \sum_{i=1}^{r} \frac{\sigma_i}{\sigma_i^2 + \alpha^2} (\boldsymbol{u}_i^T \boldsymbol{f}) \boldsymbol{v}_i, && (4.44) \end{aligned}$$

which indeed coincides with Eq. (4.39). The value for the regularization parameter $\alpha$ can be determined by the L-curve method [144], where $\alpha$ is selected corresponding to the smallest value of $(||K\boldsymbol{\rho}_\alpha - \boldsymbol{f}||_2^2 \, ||\boldsymbol{\rho}_\alpha||_2^2)$. Here $\boldsymbol{\rho}_\alpha$ means the solution of Eq. (4.39) for a given $\alpha$.

The Tikhonov method can be generalized by modifying the second term in Eq. (4.39) to

$$\alpha^2 ||\Lambda\boldsymbol{\rho} - \boldsymbol{m}||_2^2, \tag{4.45}$$

with fixed matrix $\Lambda$ and vector $\boldsymbol{m}$. If, for example, a priori knowledge of the approximative shape of the spectral function $\boldsymbol{\rho}$ exists, one can incorporate that information by setting $\Lambda = I$ and letting $\boldsymbol{m}$ take the approximate solution shape.

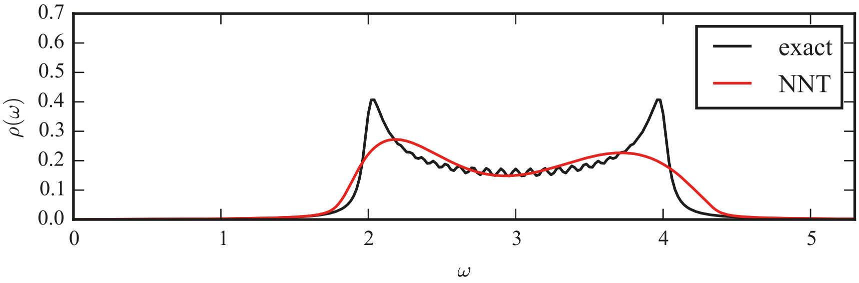

*Figure 4.6.* Spectral function of the susceptibility for a band-gap model. NNT smears the peaks due to the regularization. The Matsubara points have a statistical noise of the order of $10^{-4}$.

**Non-negative property**

The non-negative Tikhonov (NNT) method is the Tikhonov method with the additional constrain of $0 \leq \boldsymbol{\rho}$, which means:

$$\min_{0\leq\rho} ||K\boldsymbol{\rho} - \boldsymbol{f}||_2^2 + \alpha^2||\boldsymbol{\rho}||_2^2. \tag{4.46}$$

In practice, Eq. (4.46) is solved by considering Eq. 4.41 and enforcing the non-negativity by the iterative algorithm in Ref. [140]. By comparing with the NNLS spectral function of the band-gap model in Fig. 4.4, the NNT spectral function in Fig. 4.6 better resemble the exact function. The spectral weight weight between the peaks are captured well and the two peaks are present, even though they are smeared. Sometimes this smearing effect removes structure and is discussed more in section 4.7.

## 4.4 Maximum entropy method

Probably the most used method for analytical continuation in the DMFT community is the maximum entropy method (MEM) [137,145–151]. The solution of the ill-posed inversion problem is sought by regularization, so that the entropy is maximized, as following. Similar to the Tikhonov method, there is a regularization parameter $\alpha$, which needs to be determined.

**Bayesian inference**

Using Bayesian inference, a posterior probability $P(\rho|\tilde{f})$ for the spectrum $\rho(\omega)$ and the input data $\tilde{f}$ is defined as

$$P(\rho|\tilde{f}) = P(\tilde{f}|\rho)P(\rho)/P(\tilde{f}). \tag{4.47}$$

The MEM finds $\rho$ by maximizing $P(\rho|\tilde{f})$. In Eq. (4.47), $P(\tilde{f}|\rho)$ is the likelihood function, $P(\rho)$ is the a priori probability function and $P(\tilde{f})$ is a constant (since the input data is fixed) which we can ignore.

**Likelihood function**

The likelihood probability function $P(\tilde{f}|\rho)$ is a multivariate Gaussian distribution. In section 4.8 we will show how to remove correlation between the different Matsubara points, allowing us to write $P(\tilde{f}|\rho)$ simply as a product of Gaussian distributions for each Matsubara point:

$$P(\tilde{f}|\rho) = \prod_{i=1}^{M} \frac{1}{\sqrt{2\pi}\sigma_i} e^{\frac{-(f_i-\tilde{f}_i)^2}{2\sigma_i^2}} = \frac{1}{Z} e^{\frac{-\chi^2}{2}}, \tag{4.48}$$

with the normalization factor $Z = (2\pi)^{\frac{M}{2}} \prod_{i=1}^{M} \sigma_i$ and fitting-function

$$\chi^2 = \sum_{i=1}^{M} \frac{(f_i - \tilde{f}_i)^2}{\sigma_i^2}, \tag{4.49}$$

where $f_i$ is the Matsubara value corresponding to the spectrum $\rho$.

**Entropic prior**

The MEM is characterized by its a priori probability function $P(\rho)$. Statistical inference arguments exist [145], showing that the entropic prior $P(\rho|m,\alpha)$ can be expressed as

$$P(\rho|m,\alpha) = \frac{1}{Z_S} e^{\alpha S}, \tag{4.50}$$

where $Z_S$ is a normalization factor and the Shannon entropy is

$$S = \int d\omega \left[\rho(\omega) - m(\omega) - \rho(\omega) \ln\left(\frac{\rho(\omega)}{m(\omega)}\right)\right]. \tag{4.51}$$

The so called default model $m(\omega)$ should incorporate any prior knowledge about the spectrum, such as positiveness, normalization, high-frequency asymptote, etc. The entropic prior is maximized when $\rho(\omega) = m(\omega)$. The different options for choosing $\alpha$ will be discussed below.

**Probability maximization**

The most probable spectral function is found by maximizing Eq. (4.47). Using the expressions for the likelihood function and the entropic prior means maximizing the functional

$$Q[\rho] = \frac{-\chi^2}{2} + \alpha S. \tag{4.52}$$

For numerical calculations, the real-axis is typically discretized, which is discussed in section 4.2. The discretized version of the functional $Q[\rho]$, denoted as $Q(\boldsymbol{\rho})$, is maximized by setting its gradient to zero:

$$0 = \frac{\partial Q(\boldsymbol{\rho})}{\partial \rho_i} = \sum_{j=1}^{M} \frac{(f_j - \tilde{f}_j)K_{j,i}}{\sigma_j^2} - \alpha w_i \ln\left(\frac{\rho_i}{m_i}\right). \tag{4.53}$$

The kernel expression $f_i = \sum_{j=1}^{N} K_{i,j}\rho_j$ has been used in Eq. (4.53) and $w_i$ are integration weights. A commonly used FORTRAN library for solving systems of non-linear equations is MINPACK. Let us call the solution to Eq. (4.53) $\boldsymbol{\rho}_\alpha$ since it will depend on which $\alpha$-value is used. Instead of discretizing the functional in Eq. (4.52), one can instead take the functional derivative with respect to $\rho$. This avoids real-axis discretization errors. Instead one gets a analytic expression for spectral function, with some unknown parameters which can be determined by solving a set of non-linear equations, see Ref. [152, 153] for more information.

**Regularization parameter $\alpha$**

The value of $\alpha$ determines the competition between $S$ and $\chi^2$. For a small $\alpha$, overfitting will occur in presence of statistical noise on the input data and result in $\chi^2 \ll M$. For a big $\alpha$, the entropic prior will instead dominate over the likelihood function and the solution $\rho$ will be close to the default model $m$. There are several ways of choosing the $\alpha$ value, common choices are labeled Historic, Classic and Bryan's method. In the Historic MEM, $\chi^2 = M$ is desired. This is achieved by adjusting $\alpha$ and using the fact that $\chi^2$ is monotonically increasing as a function of $\alpha$. The Historic MEM usually underfits the input data which leads to smeared spectra. In the Classic MEM, $\alpha$ is estimated from Bayesian reasoning [145, 147, 151]. A probability distribution $P(\alpha|\tilde{f}, m)$ is constructed and $\alpha$ is chosen to maximize it. The expression for $P(\alpha|\tilde{f}, m)$ is [151]

$$P(\alpha|\tilde{f}, m) = \frac{1}{Z_\alpha} \frac{\alpha^{\frac{N}{2}-1} e^{Q(\boldsymbol{\rho}_\alpha)}}{\sqrt{\prod_{i=1}^{N}(\alpha + \lambda_i)}}, \tag{4.54}$$

where $Z_\alpha$ is a normalization factor and $\lambda_i$ are the eigenvalues of the matrix with elements

$$\sqrt{\rho_i \rho_j} \sum_{n=1}^{M} \frac{K_{n,i}K_{n,j}}{\sigma_n^2}. \tag{4.55}$$

The Bryan method [148] calculates $\boldsymbol{\rho}$ as an average over $\alpha$, using $P(\alpha|\tilde{f}, m)$ in Eq. (4.54) as weights, as well as the solutions $\boldsymbol{\rho}_\alpha$ from Eq. (4.53):

$$\boldsymbol{\rho}_{\text{Bryan}} = \int d\alpha P(\alpha|\tilde{f}, m)\boldsymbol{\rho}_\alpha. \tag{4.56}$$

Viewing the entropy $S$ as a regularization factor makes the MEM similar to the Tikhonov method. For the Tikhonov method we use the L-curve method

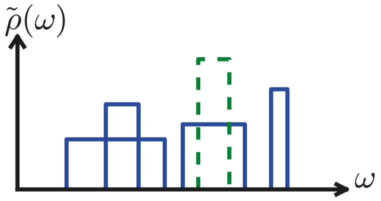

*Figure 4.7.* Representation of the spectrum given by a configuration $C$, consisting of 4 rectangles (solid blue lines). The green dashed line indicates a proposed elementary update, increasing the height of one rectangle while keeping its center position and spectral weight fixed.

to estimate $\alpha$ [144]. Applying the L-curve method to the MEM leads to $\alpha$ minimizing $-\chi^2 S$. This approach is used in paper V and paper VI and gives similar result to the Classic MEM.

## 4.5 Stochastic optimization method

The stochastic optimization method (SOM) [151, 154] belongs to a class of stochastic sampling methods to solve the Fredholm equation for the analytical continuation, see Fig. 4.1. The general idea in stochastic sampling methods is to average calculated spectra with a probability distribution $P(\rho|\tilde{f})$. The distribution should impose as little a priori knowledge as possible to avoid biased solutions. In Ref. [155] Sandvik uses $P(\rho|\tilde{f}) = e^{\frac{-\chi^2}{T}}$ to sample spectra, where $T$ acts a artificial temperature. The temperature $T$ is adjusted to sample solutions with small $\chi^2$, but not only very small $\chi^2$, since that leads to overfitting and sawtooth spectral functions. It can also be shown the MEM is a special case of the stochastic sampling methods [156].

The SOM formulated in [154] is briefly described below and is used in our papers VI and VII, where SOM is referred to as Mishchenko's method. A central difference with respect to the methods described in the other sections concerns how a spectral function $\rho(\omega)$ is represented. Instead of discretizing the real-axis to a fixed mesh, approximating the integral equation in Eq. (4.1) and finding the unknown heights at the grid points, SOM uses a set of rectangles for representing the spectrum. A spectrum of $N_r$ rectangles can be written as

$$\tilde{\rho}(\omega) = \sum_{i=1}^{N_r} R_{\{h_i,w_i,c_i\}}(\omega), \tag{4.57}$$

where the parameters $h_i, w_i, c_i$ respectively represent height, width and center position for the rectangle $i$, see Fig. 4.7. The corresponding Matsubara function, obtained from Eq. (4.1), becomes

$$f(y) = \sum_{i=1}^{N_r} h_i \int_{c_i - \frac{w_i}{2}}^{c_i + \frac{w_i}{2}} dx k(y, \omega), \tag{4.58}$$

which for some kernels can be calculated analytically. This representation avoids a systematic mesh error. To evaluate how good a spectrum is, a deviation measure similar to the $\chi^2$ is used, namely

$$D = \sum_{j=1}^{M} \frac{|f_j - \tilde{f}_j|}{|\tilde{f}_j|}, \tag{4.59}$$

where $\tilde{f}_j$ are the input data and Eq. (4.58) gives the $f_j$. The algorithm starts with randomly initializing a set of rectangles, forming a start configuration $C^{(\text{start})}$. Then, $N_e$ quasi-random elementary updates of the rectangles are performed: $C^{(\text{start})} \to C^{(1)} \to \ldots \to C^{(r)} \to \ldots \to C^{(N_e)}$. There are 7 types of elementary updates, such as changing the center position of one rectangle or changing the height but keeping the weight fixed, see Fig. 4.7. A proposed update is accepted with a probability which depends on the ratio of the deviation values between the current and the proposed configuration. The configuration $C^{(r)}$ with the smallest deviation value among the $N_e$ configurations are picked as starting point for a new sequence of $N_e$ updates. In total, $N_g$ sequences, each with $N_e$ updates, are performed. The number $N_g$ should be big enough so that the last configuration has a deviation value about the size of the stochastic noise on the input data. To avoid sawtooth features in the spectrum, the above steps are repeated $N_a$ times and the final spectrum is the average of the last spectra from the $N_a$ independent runs:

$$\rho(\omega) = \frac{1}{N_a} \sum_{i=1}^{N_a} \rho_i(\omega). \tag{4.60}$$

### GPU and MPI implementations

The minimization procedure of the deviation measure $D$ might require long simulation times, due to the presence of many local minima. A prior knowledge of the overall shape of the spectrum can partially be included in the starting configurations to arrive more rapidly at a reasonable spectrum, which reduces the computational cost. Since the $N_a$ different runs are trivially independent of each other, parallelization with message passing interface (MPI) or a graphics processing unit (GPU) can be used to reduce the time to get the solution. In a collaborative effort, involving Master and Bachelor students, both these approaches have been investigated. The original FORTRAN code of Mishchenko [154] was parallelized using MPI, while a GPU implementation of SOM was written from scratch. This implementation is presented in

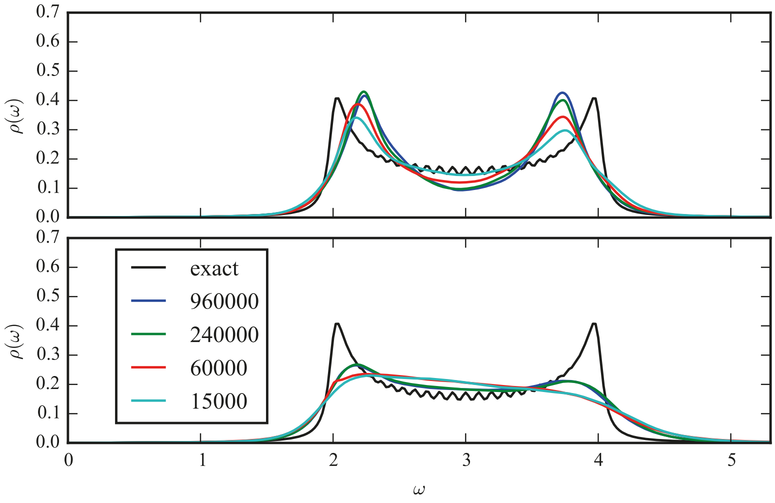

*Figure 4.8.* Spectral function of the susceptibility for a band-gap model. SOM spectral functions, for various $N_g$ values, are shown using the MPI (GPU) implementation in the top (down) panel. The Matsubara points have a statistical noise of the order of $10^{-4}$.

paper VII (Ref. [157]) and also in more details, in the bachelor thesis of Johan Nordström [158]. It is not easy to make a fair comparison between a GPU program and a program using MPI, but the examples below gives a hint of the actual times and the computational resources used. The examples are the analytical continuations of the two different tight binding models (for one k-point) in paper VI. $N_g = 240000$ updates and $N_a = 128$ attempts were used. With MPI 128 CPUs were used. The simulation using the GPU implementation was around 4 times faster than using MPI. One shall also note that 128 CPUs consume more energy than a single GPU and require access to a supercomputer facility. Using MPI and GPU, the spectra for the doped tight binding model are similar. However for the band-gapped tight binding model, the output spectral functions were not identical, as shown in Fig. 4.8. Using the MPI code, the spectra contain the two-peak structure and change when vary $N_g$. The GPU code barely resolves the two peaks and gives smaller changes by varying $N_g$. One reason of the difference output and speed is related to that $N_e$ was fixed to 400 in the GPU case but varied stochastically between 1 to 7000 in the MPI case. There are also other optimization differences, such as the number of starting rectangles, the maximum allowed number of rectangles and the proposal and acceptance distributions for an elementary update. Comparing with the NNLS and NNT methods, shown in Fig. 4.4 and 4.6, the SOM method gives an accurate description of the exact spectrum for the considered noise level $10^{-4}$.

## 4.6 Padé approximants

A Padé approximant can be expressed as a $[k/r]$ rational polynomial [159, 160]:

$$P_{k,r}(z) = \frac{\sum_{i=1}^{k+1} a_i z^{i-1}}{\sum_{i=1}^{r} b_i z^{i-1} + z^r}, \tag{4.61}$$

with coefficients $a_i, b_i \in \mathbb{C}$. Analytical continuations in the complex plane from e.g. Matsubara frequency points on the imaginary axis to the real axis, see Fig 1.5, can be performed with the Padé approximant method. The Green's functions $G(z)$ and the dynamical part of the self-energy $\Sigma_D(z)$ decay with asymptote $s/z$ when $|z|$ increases, as can be seen from Eq. (1.24). For self-energies, $s \in \mathbb{R}^+$ [161], while for fermionic Green's functions, $s = 1$, due to the normalization condition of the spectral function. For bosonic Green's functions with an odd spectral function, $s = 0$. Therefore its asymptote behaves instead as $\sim 1/z^2$. The Padé approximant defined in Eq (4.61) has the asymptote $a_{k+1} z^{k-r}$ for large $|z|$. Self-energies and fermionic Green's functions are hence suitably represented by $[(r-1)/r]$ approximants:

$$P(z) = \frac{\sum_{i=1}^{r} a_i z^{i-1}}{\sum_{i=1}^{r} b_i z^{i-1} + z^r}, \tag{4.62}$$

with $N = 2r$ coefficients and asymptote $a_r/z$, where $a_r = s \in \mathbb{R}^+$. A correct asymptote for odd bosonic Green's functions is obtained by either using a $[(r-2)/r]$ Padé approximant or setting $a_r = 0$. Given $M$ function values $f(z_i)$, at points $z_i$ in the complex plane, the task to find a Padé approximant $P(z)$ such that

$$P(z_i) = f(z_i), \text{ for } i \in \{1, 2, ..., M\}, \tag{4.63}$$

is discussed below. In the context of the Matsubara formalism, the points $z_i$ are Matsubara frequency points and the approximant is evaluated just above the real axis.

### 4.6.1 Thiele's reciprocal difference method

Thiele's reciprocal difference method [159, 162, 163] for determining the Padé approximant was first applied in the field of condensed matter physics by Vidberg and Serene [162]. The method is fast and recursive, and starts by formulating the Padé approximant as a terminated continued fraction:

$$P_N(z) = \cfrac{c_1}{1 + \cfrac{c_2(z - z_1)}{1 + \cfrac{c_3(z - z_2)}{\cdots + \cfrac{c_N(z - z_{N-1})}{1}}}}, \tag{4.64}$$

where the subscript $N$ denotes the number of (unknown) coefficients $c_i$, which in Thiele's algorithm coincides with the number of input points $M$. By demanding the approximant to fulfil Eq. (4.63), the coefficients $c_i$ are given by the recursion

$$\begin{aligned} g_i(z) &= \frac{g_{i-1}(z_{i-1}) - g_{i-1}(z)}{(z - z_{i-1})g_{i-1}(z)}, \text{ for } i \in \{2,3,...,N\} \\ c_j &= g_j(z_j)\ ,\ g_1(z_j) = f_j, \text{ for } j \in \{1,2,...,N\}. \end{aligned} \tag{4.65}$$

By viewing $g_i(z_j)$ as a $N \times N$ matrix, the initially unknown Padé coefficients $c_i$ are on the diagonal, the first row has elements $f_j$ and the recursion relation can be used to determine the elements one row below. To attain the diagonal elements $g_i(z_i)$ the elements in the upper triangle of the matrix have to be determined, which is a $\mathcal{O}(N^2)$ process. Once the coefficients $c_i$ are determined, the continued fraction can be calculated at a point $z$ according to

$$P_N(z) = \frac{A_N(z)}{B_N(z)}, \tag{4.66}$$

where

$$\begin{aligned} A_{n+1}(z) &= A_n(z) + (z - z_n)c_{n+1}A_{n-1}(z) \\ B_{n+1}(z) &= B_n(z) + (z - z_n)c_{n+1}B_{n-1}(z) \end{aligned} \tag{4.67}$$

and

$$A_0 = 0, A_1 = c_1, B_0 = B_1 = 1. \tag{4.68}$$

For odd $N$, $P_N(z)$ is a $[\frac{N-1}{2}/\frac{N-1}{2}]$ approximant and for even $N$, the approximant is of the order $[\frac{N}{2} - 1/\frac{N}{2}]$. To have the asymptote of Green's functions, an even $N$ is suitable and makes $P_N(z)$ of the form as in Eq. (4.62).

### 4.6.2 Square matrix formulation

The square matrix formulation by Beach et al. [161] requires the Padé approximant in Eq. (4.62), with $N = 2r$ coefficients, to fulfil Eq. (4.63) for $M = N$. By introducing the vectors

$$\boldsymbol{v} = \begin{bmatrix} \boldsymbol{a} \\ \boldsymbol{b} \end{bmatrix} = \begin{bmatrix} a_1 \\ \vdots \\ a_r \\ b_1 \\ \vdots \\ b_r \end{bmatrix}, \quad \boldsymbol{y} = \begin{bmatrix} z_1^r f(z_1) \\ z_2^r f(z_2) \\ \vdots \\ z_N^r f(z_N) \end{bmatrix} \tag{4.69}$$

and the matrix

$$K = \begin{bmatrix} 1 & \cdots & z_1^{r-1} & -f(z_1) & \cdots & -f(z_1)z_1^{r-1} \\ 1 & \cdots & z_2^{r-1} & -f(z_2) & \cdots & -f(z_2)z_2^{r-1} \\ \vdots & \vdots & \vdots & \vdots & \vdots & \vdots \\ 1 & \cdots & z_N^{r-1} & -f(z_N) & \cdots & -f(z_N)z_N^{r-1} \end{bmatrix}, \tag{4.70}$$

the problem of finding the coefficients for the Padé approximant is given by

$$K\boldsymbol{v} = \boldsymbol{y}. \tag{4.71}$$

Once Eq. (4.71) is solved, the Padé approximant at a point $z$ can be written as

$$P(z) = \frac{[1, z, z^2, ..., z^{r-1}]\boldsymbol{a}}{[1, z, z^2, ..., z^{r-1}]\boldsymbol{b} + z^r}. \tag{4.72}$$

Solving a linear system of equations requires $\mathscr{O}(N^3)$ operations, making it slower than Thiele's algorithm. On the other hand, for matrix problems, highly efficient routines are available.

### 4.6.3 Zero-pole pairs

The ill-posed nature of the analytical continuation manifests itself by a big condition number of the matrix $K$. By looking at the ratio between the largest and the smallest elements in $K$, $\xi = v_{\max}^r$, the numerical precision needed to invert $K$ can be estimated to be $2\log_{10}\xi$ decimal digits [161,164]. If extremely high precision input data exists, which seldom is the case in electronic structure calculations, and equally high inversion precision routines are used, the Padé approximant is known to perform very well [161]. However, for moderate precision, approximate Padé approximant coefficients can give rise to spurious peaks or breaking of required symmetries, such as the non-negativity of the spectral function. The optimal choice of the number of coefficients $N$ in the approximant is in general not known a priori. If very high precision data are available, Ref. [161] showed that the value of the coefficient $a_r$ can be used to estimate a good value of $N$. Since fermionic Green's functions have an asymptote $1/z$ and the Padé approximant has an asymptote $a_r/z$, the imaginary part of $a_r$ should be zero. The number $N$ giving the smallest imaginary part works as a criterion for choosing the optimal $N$. Another approach for choosing $N$ is focused on the zeros and the poles of the approximant. By finding the zeros of the polynomials in the numerator and denominator of $P(z)$, the approximant can be written as [165]

$$P(z) = C\frac{\prod_{i=1}^{r-1}(z-p_i)}{\prod_{i=1}^{r}(z-q_i)}, \tag{4.73}$$

with $C \in \mathbb{C}$ being a constant. Let us assume that the function to analytically continue $f(z)$ can be written as a sum of a *finite* number, $r_0$, of poles. When the number of poles in the approximant, $r$, is smaller than $r_0$, the approximant will not be able to model the true function perfectly, even if an arbitrary precision is accessible. If instead $r_0 < r$, some zeros in the numerator will cancel out redundant poles [161]. But due to the finite precision, these zero-pole pairs will not cancel out completely, and can potentially cause artefacts in the spectral function. The higher $r$, the more of these non-canceling zero-pole pairs will appear. Assuming that a spurious non-canceling zero-pole pair $(p_j, q_j)$ exists in $P(z)$, it can be removed by multiplying $P$ with $(z - q_j)/(z - p_j)$. Many techniques exist for identifying and removing these zero-pole pairs. As discussed in Ref. [165], one approach defines zero-pole pairs as spurious if the zero and the pole are within a certain distance from each other. To check the stability of poles and zeros, Ref. [166] shows that adding a random number to the input data changes spurious zeros and poles more than actual ones. If high order poles do not exist in $P(z)$, the approximant can be expressed as a sum of poles [165]

$$P(z) = \sum_{i=1}^{r} \frac{w_i}{z - q_i}, \tag{4.74}$$

where $w_i$ is the residue corresponding to the pole at position $q_i$. Ref. [165] also argues that poles with a negative residue shall be removed to make the approximant more similar to a sum of poles on the real axis with positive residues, which is know to have a positive spectral function (see the Lehmann representation in Eq. (1.39)).

### 4.6.4 LS Padé

This subsection and the following ones contain an overview of the method development on the Padé approximant done in paper V (Ref. [167]), aiming at improving the stability and accuracy of the analytical continuation. Both Thiele's reciprocal difference method and Beach's square matrix formulation presented in subsection 4.6.1 and 4.6.2, use equally many input points $M$ as approximant coefficients $N$. As discussed in subsection 4.6.3, the absence of very precise input data may lead to unstable spectral functions, due to overfitting of the noisy data. To reduce the risk of overfitting we proposed to use equal or more input points $M$ than the number of approximant coefficients $N$, thus $N \leq M$, and seek a LS solution, which was also suggested in Ref. [164]. By generalizing the square matrix formulation in subsection 4.6.2, the matrix and vector shapes are modified to $K \in \mathbb{C}^{M \times N}$, $\boldsymbol{v} \in \mathbb{C}^{N}$ and $\boldsymbol{y} \in \mathbb{C}^{M}$. For highly noisy input data one can not expect to retrieve as many and sharp spectral features as for high precision data. It is in such cases reasonable to work with fewer degrees of freedom in the approximant, meaning a low $N$. The advantage of the LS Padé is that we are not restricted to use equally few input points, but can still include as many points as desirable.

### 4.6.5 Averaging

Instead of looking at zeros and poles of the Padé approximant for determining the number of coefficients to use in the approximant, we here discuss the possibility of considering several different independent pairs of $N$ and $M$, and then taking an average over the resulting spectral functions. Let us denote each such pair as a configuration $c$. Since spurious non-canceling zero-pole pairs arise from the absence of arbitrary precise numerical data, one can expect them to be different for different configurations. The non-negative property of the spectral function, see Eqs. (1.32) and (1.33), allows us to discard unphysical configurations breaking it. In the averaging, to avoid the risk of one or a few configurations with spurious spectral function structure of degrading the average, only configurations with spectra similar to each other are considered. This can be achieved by using the deviation measure

$$\Delta_c = \sum_{c' \neq c} \int_{-\infty}^{\infty} d\omega |\rho(\omega) - \rho'(\omega)|, \tag{4.75}$$

where the sum runs over physical configurations. We can then discard configurations with a big relative $\Delta_c$. This mechanism is illustrated in Fig. 4.9, where $\Delta_c$ for various LS Padé approximants is reported. How the spectral function improves by the ideas outlined above is shown in Fig. 4.10 (taken from paper V).

### 4.6.6 Mirror symmetry

When doing the analytical continuation, one solves the Fredholm integral in Eq. (4.1) or performs a Padé approximant fit of Matsubara frequency data. In the first case, the mirror symmetry in Eq. (1.36) is automatically fulfilled. However, using Padé, this is not the case. One way of trying to enforce the mirror symmetry in the Padé approximant is to include in the fitting also negative Matsubara points. As pointed out in Ref. [168], symmetrically including positive and negative frequencies tends to put the poles in the Padé approximant near the real axis, giving a spuriously peaky spectrum. However, this problem can be avoided by including only a limited number of negative frequencies. This is shown in paper V to give a more accurate spectral function, as can be also seen in Fig. 4.10.

As a test to see how well the Padé method actually fulfils the mirror symmetry, we perform the analytical continuation of a Green's function from Matsubara frequencies to axes at distances $\pm 0.2$ away from the real axis. According

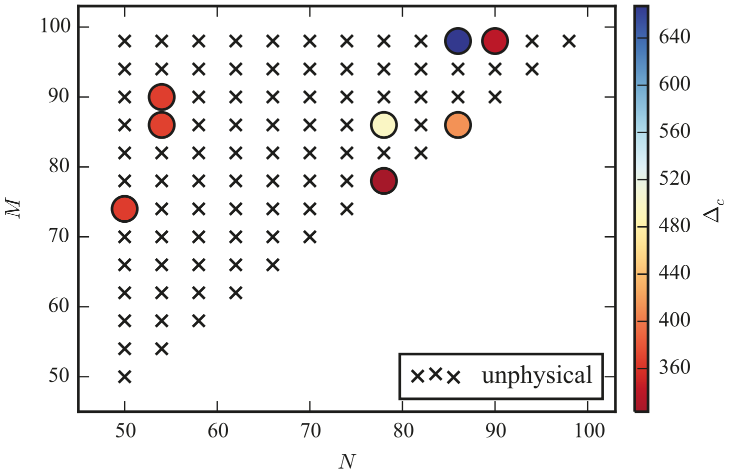

*Figure 4.9.* Illustration of configurations in $(N, M)$ space. The black crosses denote unphysical continuations and the circles denote physical continuations. The color of the circles denotes the deviation $\Delta_c$. The test model is the self-energy of a Sm atom, with relative noise of magnitude $\sigma = 10^{-6}$ added on the Matsubara points before the continuation. More details can be found in paper V.

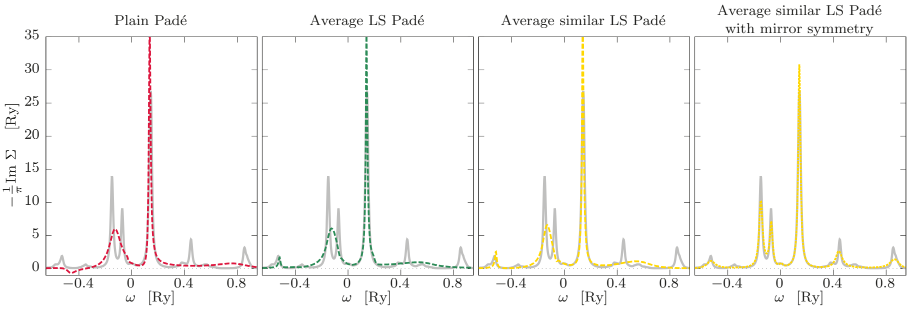

*Figure 4.10.* Illustration of the different improvements done on the square matrix formulation of Padé. Description of the four obtained spectra (from left to right panel): Padé approximant using $N = M = 70$, and characterised by unphysical features; LS Padé average, including unphysical continuations; LS Padé using $\Delta_c$; LS Padé using $\Delta_c$ and with mirror symmetry imposed using 6 negative Matsubara points. The test model is the self-energy of a Sm atom, with relative noise of magnitude $\sigma = 10^{-6}$ added on the Matsubara points before the continuation. More details can be found in paper V.

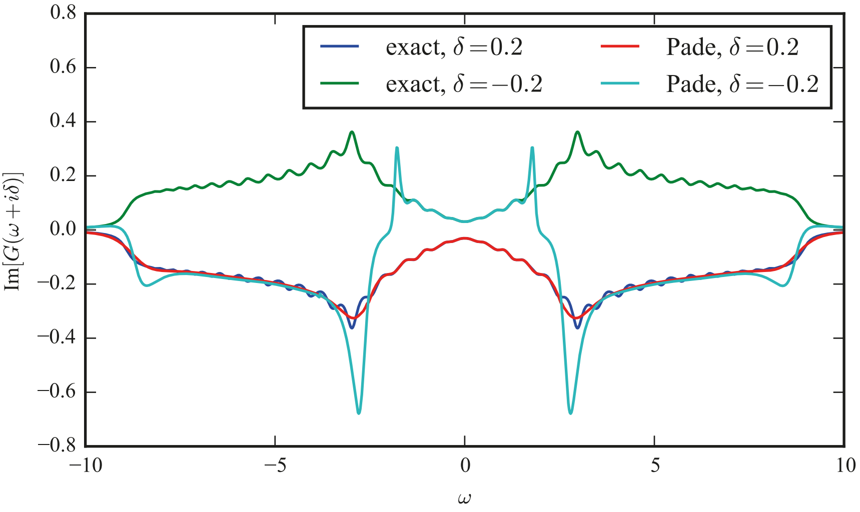

*Figure 4.11.* Imaginary part of Green's functions obtained by analytical continuation using Padé from Matsubara frequencies $i\nu_n$ to distances ±0.2 above the real axis. The test model is the Green's function from a tight-binding model of Graphene where the exact function is known. In the Padé approximant fit, 9 negative Matsubara points are included.

to the mirror symmetry in Eq. (1.36), the imaginary part of the Green's function along those axes should have opposite sign. However this is fulfilled only for small $\omega$, where the Padé Green's function coincides with the exact one, see Fig. 4.11. For large $\omega$, instead of having opposite sign, the Green's functions become similar, thus the mirror symmetry is not fulfilled. These results hold for this test function both with and without including a few negative Matsubara points.

### 4.6.7 Inversion precision

The numerical precision in the inversion routine should be high enough so that the spectral function does not alter by further increasing the inversion precision. In the case of noise-free input data, the precision needed to solve the matrix problem in Eq. (4.71) is approximately $2\log_{10}\xi$ decimal digits, with $\xi = \nu^r_{\max}$ being the ratio of the largest to the smallest elements in the matrix $K$ [161, 164]. This precision is much higher than double or quadruple precision. In paper V, we instead investigated the inversion precision needed in the presence of input noise. By using a multiple precision library [169], precision around quadruple was shown to be sufficient for a range of noise levels. Double precision resulted in absent peaks in the spectrum compared

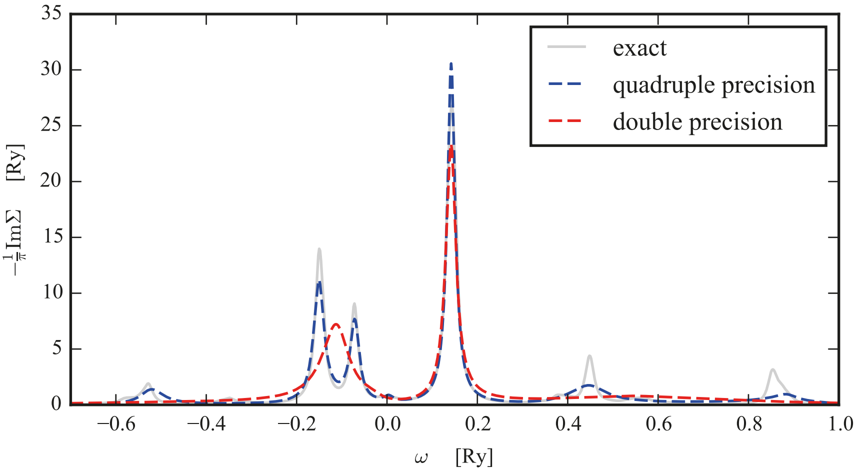

*Figure 4.12.* Spectra attained using double and quadruple precision LAPACK routines. The test model is the self-energy of a Sm atom, with relative noise of magnitude $\sigma = 10^{-5}$ added on the Matsubara points before the continuation. More details can be found in paper V.

to higher precisions, unless very big noise was used. An example of this is shown in Fig. 4.12.

### 4.6.8 Summary of method development

In paper V we developed a Padé scheme to perform the analytic continuation of Green's functions and self-energies. First the LS approach was introduced. Secondly an average scheme over several LS spectra, rejecting spectra with negative weight, was shown to improve the stability and the accuracy. Including a few negative Matsubara points was shown to better resolve peak structures, under the condition of small spectral weight at zero energy. We obtained the insight that quadruple precision, but not less, is enough in the presence of stochastic noise with magnitudes typical in electronic structure calculations. By comparing the developed Padé algorithm with NNLS, NNT and MEM, it was shown to perform well, e.g. to resolve two closely positioned peaks.

## 4.7 A comparision between methods for bosonic functions

In paper VI (Ref. [170]), three different physically relevant bosonic models are analytically continued, using the methods described above: NNLS, NNT, MEM, SOM and Padé. The influence of numerical noise in the input data on the spectra is investigated. In general, the SOM is the most robust approach for various magnitudes of the input noise. For the smallest investigated noise, the Padé scheme and the SOM are the most accurate methods. Spectral functions with broad modes away from zero are shown to be difficult to resolve correctly, causing spurious wiggles, especially for the simple NNLS method. In such cases MEM, NNT and SOM are preferable. Functions with two distinct peaks, on the other hand, are much easier to continue and the NNLS method performs very well. Another observation is that a single sharp peak close to zero energy is accurately captured even at high noise levels by all methods. The function dependence for the performance shows it is important to consider several test cases for evaluating analytical continuation algorithms. The MEM, NNT and Padé tend to smear the spectra and sometimes merge two actual peaks into one peak. The tendency to merge peaks and the risk of creating spurious peaks makes it hard to analyze a single spectrum. Nevertheless, considering several different continuation methods helps in understanding the most important features of the true spectrum.

## 4.8 Correlation

Matsubara Green's function data can contain undesired correlation if it is sampled by a QMC algorithm. This should be taken into account before the analytical continuation. There are two types of correlations within the QMC data. Correlations between samples of an observable in one QMC Markov chain can be eliminated by binning analysis. Another type of correlation is between different observables, in this case Green's function points. By decomposing the covariance matrix of the input data, uncorrelated observables are created. In practice this means the analytical continuation is performed using modified input data as well as kernel.

### 4.8.1 Binning analysis

Let us denote $N$ eventually correlated sample measurements of an observable from a distribution, perhaps created by a QMC simulation, by $O_i^{(0)}$, with $i \in 1,2,...,N$. These raw data have the super script $^{(0)}$. The procedure to remove correlations from these measurements involves averaging the raw data into bins [171]:

$$O_i^{(j)} = \frac{O_{2i-1}^{(j-1)} + O_{2i}^{(j-1)}}{2}, \text{ for } i \in [1,2,...,N_j \equiv \frac{N}{2^j}]. \tag{4.76}$$

As $j$ increases, the bins $O_i^{(j)}$ become less correlated. This allows us to estimate the variance of the mean value of $O_i^{(0)}$ by

$$\sigma^2 = \lim_{j\to\infty} \frac{\mathrm{Var}[O_i^{(j)}]}{N_j}. \tag{4.77}$$

From Ref. [171] the correlation length $\tau$ is equal to

$$\tau = \frac{1}{2}\left(\frac{N\sigma^2}{\mathrm{Var}[O_i^{(0)}]} - 1\right). \tag{4.78}$$

Hence bins with $\tau < 2^j$ should be used to get uncorrelated samples. The upper bound for possible $j$ is in practice determined by the precision needed for the covariance matrix, see below.

## 4.8.2 Covariance matrix

Let $\tilde{f}_{i,k}$ denote measured Matsubara Green's function data, where $k \in \{1,2,...,N\}$ labels different uncorrelated data sets. Each set contains $M$ different, possibly correlated, observables which are labeled by $i \in \{1,2,...,M\}$. For example, $\tilde{f}_{i,k}$ represent the data from a binning analysis of QMC data. The averages

$$\tilde{f}_i = \frac{1}{N}\sum_{k=1}^{N} \tilde{f}_{i,k} \tag{4.79}$$

have the covariance estimator

$$C_{i,j} = \frac{1}{N(N-1)}\sum_{k=1}^{N} (\tilde{f}_{i,k} - \tilde{f}_i)(\tilde{f}_{j,k} - \tilde{f}_j). \tag{4.80}$$

For a precise estimation of the covariance matrix, the number of data sets has to be at least bigger than the number of observables ($N > M$). Using the covariance matrix we can formulate the $\chi^2$ deviation measure for the analytically continued function as

$$\chi^2 = \Delta \boldsymbol{f}^T C^{-1} \Delta \boldsymbol{f}. \tag{4.81}$$

The element $\Delta f_i = f_i - \tilde{f}_i$ expresses the difference between the input data in Eq. (4.79) and the Matsubara data $f_i$ corresponding to the analytically continued function. For uncorrelated data, the covariance matrix is diagonal with $C_{ii} = \sigma_i^2$, where $\sigma_i$ is the estimated standard deviation for $\tilde{f}_i$. Then $\chi^2 = \sum_{i=1}^{M} \frac{\Delta f_i^2}{\sigma_i^2}$, which we have seen before in Eq. (4.49). The covariance matrix is related to the correlation matrix defined as $C_{i,j}/(\sigma_i \sigma_j)$, which takes values between $-1$ and 1. In paper VI the Hubbard dimer is studied and correlation matrices of the QMC data in shown in Fig. 4.13.

We here present two ways of reformulating Eq. (4.81) into a rotated uncorrelated representation, enabling us to employ the analytical continuation methods discussed earlier in this chapter. For a more extensive description than the one that follows below, please look in Ref. [151].

**Cholesky decomposition**

The covariance is positive definite which allows for a Cholesky decomposition as $C^{-1} = W^T W$. Inserted in Eq. (4.81), this gives

$$\chi^2 = ||\Delta \boldsymbol{f}'||_2^2, \tag{4.82}$$

where $\Delta \boldsymbol{f}' = W \Delta \boldsymbol{f}$. The integral kernel $K$ and the input data $\tilde{\boldsymbol{f}}$ for the Fredholm equation are thus modified to $K' = WK$ and $\tilde{\boldsymbol{f}}' = W\tilde{\boldsymbol{f}}$.

**Eigendecomposition**

The eigendecomposition $C = UDU^T$ simplifies Eq. (4.81) to

$$\chi^2 = \sum_{i=1}^{M} \frac{\Delta f_i'^2}{\sigma_i^2}, \tag{4.83}$$

where $\sigma_i^2$ are the eigenvalues of $C$, occurring on the diagonal of $D$, and $\Delta \boldsymbol{f}' = U^T \Delta \boldsymbol{f}$. The integral kernel $K$ and the input data $\tilde{\boldsymbol{f}}$ when solving the Fredholm equation are thus modified to $K' = U^T K$ and $\tilde{\boldsymbol{f}}' = U^T \tilde{\boldsymbol{f}}$.

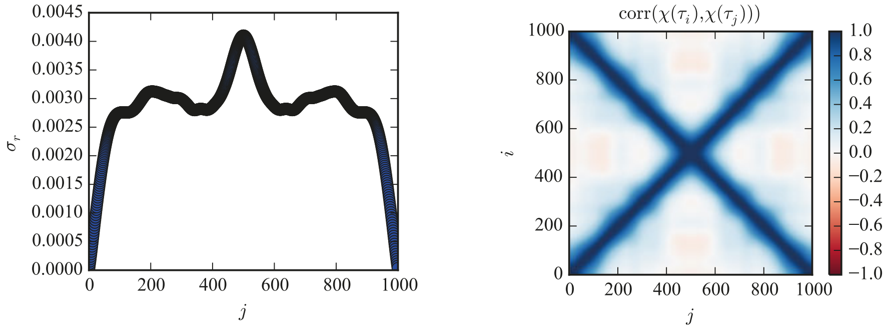

(a) Relative standard deviation, in $\tau$ space.

(b) Correlation matrix, in $\tau$ space.

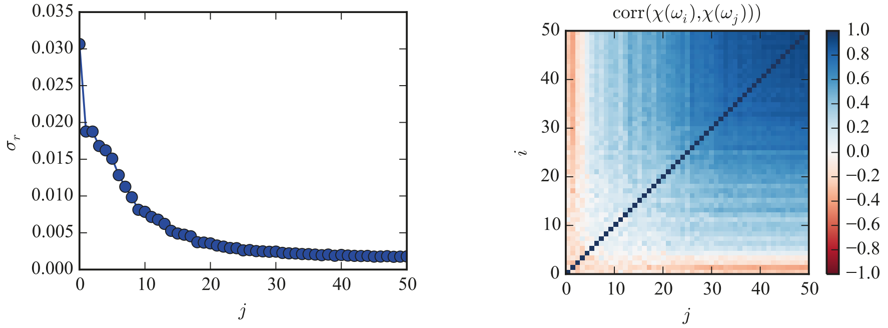

(c) Relative standard deviation, in Matsubara frequency space.

(d) Correlation matrix, in Matsubara frequency space.

*Figure 4.13.* The noise characteristics of QMC data for the Hubbard dimer.

# 5. Summary and outlook

This thesis is based on in the following works:

**Paper I**: The Mott phase of the Hubbard model is studied using DMFT with a stochastic impurity solver. The self-energy is constructed from an average over a distribution of impurity models. Few bath states are used for each impurity model, enabling ED to be used. Spectral functions with sharp features are obtained, for moderate computational cost. An interesting project for the DED method would be to study larger impurity systems, with more bath sites, to investigate the convergence of the observed finite-size effects. Another interesting area of applicability of DED is multi-orbital systems, where computational efficiency is an important concern.

**Paper II**: Inter-site $J_{ij}$'s are obtained by means of DFT$+U$ through the MFT. Good estimates of ordering temperatures and magnon dispersions are provided, if combined with atomistic spin dynamics simulations [172–175]. Our results suggest that if one extracts the $J_{ij}$'s from the DFT+$U$ total energies, the use of a spin non-polarized functional (e.g. LDA) is preferable. To investigate if this conclusion also holds for DFT+DMFT could be an interesting project.

**Papers III-IV**: In paper III, a DFT+MLFT approach is developed and applied to four TMOs, leading to good agreement between theoretical and experimental spectra. In paper IV, Mo doped $LaFeO_3$ is studied. Experimental and theoretical XA spectra are compared, primarily to investigate the charge disproportionation as a function of Mo the doping. To analyze the system using DFT+DMFT would be an interesting continuation.

**Papers V-VII**: In paper V, a Padé approximant scheme is developed. It can be applied to several problems arising in strongly correlated physics. To extract the spectral function within DMFT an analytical continuation is needed for impurity solvers working on the Matsubara axis. It may also be useful for codes working on the Matsubara axis in order to more accurately discretize the hybridization function in ED [51,113]. Finally, a number of LDA+DMFT implementations have analytical continuations in their computational cycle, such as e.g. the KKR/EMTO implementations of Refs. [163,176,177]. There our Padé scheme, with improved stability and enhanced accuracy, may be beneficial. In paper VI, several analytical continuation methods are compared with each other for various test systems, in terms of accuracy and precision. To use several methods is seen to help in the analysis of obtained spectral functions. A stochastic optimization method is among the tested methods, and a GPU implementation of this method is presented in paper VII. To study the analytical continuation of the off-diagonal elements of single-particle Green's functions, having a normalization condition described by Eq. (1.38), could be a challenging and interesting future project.

# 6. Populärvetenskaplig sammanfattning

Klassisk fysik beskriver naturen på en vanlig (makroskopisk) skala. Men för att förstå, beskriva och förutse verkligheten på en längdskala på några atomer (ungefär 0.0000000001 m), kan inte längre klassisk fysik tillämpas utan kvantfysik behövs. Som namnet kvantfysik antyder är kvantiteter så som energi, rörelsemängd och rörelsemängdsmoment begränsade till kvantiserade värden. Under de senaste ca 100 åren har förståelsen för kvantfysik ökat enormt. Detta har varit nödvändigt för utvecklingen av t.ex. transistorer i datorer, magnetisk datalagring, lasrar och tekniker för medicinsk bildbehandling. Ett fascinerande exempel på en nylig tillämpning av kvantfysik är då forskare 2014 lyckades överföra informationsdata 3 meter med hjälp av kvantteleportering, vilket i framtiden kan komma att användas för kvantkommunikation och kvantberäkningar [178]. Förra året, ett annat imponerande vetenskapligt framsteg gjordes, då den redan världsledande tokamak fusionsrektorn i Kina slog sitt eget världsrekord genom att upprätthålla plasma i 101 sekunder [179]. Utan förståelse av kvantfysik hade denna bedrift, att efterlikna solen, inte varit möjlig. Inom materialfysik är ett mål att kunna förutse materials egenskaper med hjälp av universella kvantmekaniska lagar. Trots att dessa lagar är kända är ekvationerna, som beskriver elektronerna i det aktuella materialet, svåra att lösa och datorsimuleringar används i stor utsträckning. I många material kan approximativa och beräkningseffektiva metoder tillräckligt noggrant beskriva verkligheten. Den hittills kanske mest framgångsrika metoden är den Nobelprisbelönta täthetsfunktionalteorin (DFT) [9, 10]. Men för en grupp material, där växelverkan mellan elektronerna är stor, fallerar DFT. I dynamisk medelfältsteori (DMFT) behandlas elektron-elektron växelverkan mer explicit än i DFT, vilket gör den lämplig för att beskriva dessa starkt korrelerade system. I DMFT översätts systemet med elektroner som rör sig i ett gitter till ett enklare system med en atom med elektroner och dess omgivning. Att lösa problemet med en atom som är kopplad till en omgivning kan dock fortfarande innebära tidskrävande datorberäkningar. I Artikel I används och utvecklas en stokastisk metod för att snabbare lösa detta problem. Att kombinera DFT med DMFT (DFT+DMFT) är idag en av de mest populära och noggranna metoderna för att beskriva material på en atomär längdskala. För att simulera magnetism i material kan först kvantmekaniska beräkningar göras, t.ex. med DFT+DMFT. De erhållna resultaten kan sedan användas i en klassisk modell för att förutsäga magnetiska egenskaper på en makroskopisk skala. I Artikel II genomförs dessa steg för fem olika övergångsmetalloxider (TMOs).

För att karaktärisera material används många olika experimentella metoder. Spektroskopi, studien av material-ljus växelverkan, är en dessa verktyg. Genom att lysa ljus med en viss frekvens, mäta hur mycket av ljuset som absorberas av materialet, och sedan variera frekvensen kan ett absorptionsspektrum samlas in. I den här avhandlingen har röntgen absorptions spektroskopi (XAS) studerats, vilket ger kunskap om elektronstrukturen och den lokal geometrin i materialet. Det som händer inne i materialet är att ljuset exciterar en hårt bunden elektron (kärnelektron) till oockuperade orbitaler (så kallade valens orbitaler) . Då elektronerna i materialet känner av att en kärnelektron har flyttats bort och lämnat ett hål efter sig kommer en växelverkan uppstå mellan hålet och valenselektronerna. För att korrekt simulera XAS behöver denna växelverkan behandlas explicit, vilket görs i Artiklarna III och IV för olika TMOs. God överensstämmelse fås med experimentellt uppmätta spektrum. I kapitel 3 beskrivs ytterligare ett spektroskopi projekt, där en väldigt fokuserad stråle med elektroner av väldigt hög energi propagerar genom $CaTiO_3$. Spektrum med en atomär rumslig upplösning uppmäts och överensstämmer kvalitativt med genomförda teoretiska simuleringar.

Ett kritiskt steg i DMFT, kallat analytisk fortsättning, är nödvändigt för att erhålla fysikaliska storheter. Analytisk fortsättning betyder en transformation av en funktion in det komplexa talplanet, och innebär en övergång från imaginära frekvenser till reella frekvenser. Detta är ett numeriskt ostabilt problem som erfordrar robusta algoritmer med avseende på numeriskt brus. Metoden att anpassa Padé approximanter studeras och utvecklas i Artikel V. En GPU implementering av en stokastisk metod presenteras i Artikel VII. I Artikel VI jämförs flera olika metoder för analytisk fortsättning. För och nackdelar med respektive metod presenteras tillsammans med resultat för olika brusnivåer på indatan.

# 7. Acknowledgements

I am very grateful for being given the opportunity to conduct PhD studies in the nice atmosphere at the Materials Theory division. Especially I would like to thank my advisors Igor Di Marco, Olle Eriksson, Oscar Grånäs and Patrik Thunström for sharing your scientific knowledge during these years. Igor, you are always enthusiastic, positive and supportive, despite periods of health issues. I would like to thank you for all your help and for the work we have done together. Olle, you always give advise, propose new projects, and spread enthusiasm, thanks for being a great boss. I have also had a lot of guidance from Yaroslav Kvashnin and Lars Nordström, thank you very much! For the analytical continuation projects I also would like to thank Inka Locht, Erik van Loon, Elin Lundin, Vidar Stiernström, Joakim Johansson, Viktor Edward, and Johan Nordström for many discussions. Weiwei Sun, it was a lot of fun to work with you in the GW project. I would like to express my gratitude to my former advisor Mats Granath at Gothenburg University. There have been many people involved in my XAS endeavours, and I would like to thank Johann Lüder, Anna Delin, Biplab Sanyal, Barbara Brena and Mebarek Alouani for helpful discussions. It was very interesting to get involved in the EELS project and I enjoyed it a lot, thank you Jan Rusz. Somnath Jana and Swarup Panda, thank you for involving me in your interesting work. In the division I also would like to thank Olga, Johan, Xin, Raquel, Henning, Diana, Suhas, Alexander, Jakob and many more for countless friendly conversations. Samara, thank you for being with me. Lastly I would like to thank my family and friends outside the Materials Theory division for your support.

# Appendices

# A. Matsubara summation

To relate the imaginary time Green's function $G(\tau)$ with the spectral function $\rho(\omega)$ we combine Eq. (1.18) and Eq. (1.23), which gives us

$$G(\tau) = \frac{1}{\beta} \sum_{n=-\infty}^{\infty} e^{-i\nu_n\tau} G_n = \int_{-\infty}^{\infty} d\omega \rho(\omega) \frac{1}{\beta} \sum_{n=-\infty}^{\infty} \frac{e^{-i\nu_n\tau}}{i\nu_n - \omega}. \tag{A.1}$$

We have to perform the summation of the Matsubara points following the procedure outlined in Ref. [133]. We introduce $g(z) = \frac{e^{-z\tau}}{z-\omega}$ and an auxiliary function $h(z)$. We require $h(z)$ to have poles at the Matsubara points with residues equal to one. The sum can now be expressed as an integral in the complex plane by using Cauchy's residue theorem:

$$\sum_{n=-\infty}^{\infty} g(i\nu_n) = \sum_{z_p \in \text{poles of } h} \text{Res}(gh, z_p) = \frac{1}{2\pi i} \oint_C dz g(z)h(z), \tag{A.2}$$

where the integration path $C$ is shown in Fig. A.1. If $g(z)h(z)$ decays for large $|z|$ the only remaining contribution of the integral is from the path around the pole of $g(z)$. This enables us to again use Cauchy's residue theorem, hence

$$\frac{1}{2\pi i} \oint_C dz g(z)h(z) = \frac{1}{2\pi i} \oint_{C'} dz g(z)h(z) = -\text{Res}(gh, w) = -e^{-\omega\tau} h(\omega). \tag{A.3}$$

Note that the minus sign occurs since the path $C'$ is anti-clock wise. For $0 < \tau > \beta$, an auxiliary function which has poles at the Matsubara points with residues of one, and balances the divergence in $g(z)$ at large $|z|$ in the left half plane is $h(z) = \frac{\beta}{1 \pm e^{-\beta z}}$. This finally gives us an expression for the imaginary time Green's function

$$G(\tau) = \int_{-\infty}^{\infty} d\omega \rho(\omega) \frac{1}{\beta} * -e^{-\tau\omega} h(\omega) = \int_{-\infty}^{\infty} d\omega \rho(\omega) \frac{-e^{-\tau\omega}}{1 \pm e^{-\beta\omega}}, \text{ for } 0 < \tau < \beta. \tag{A.4}$$

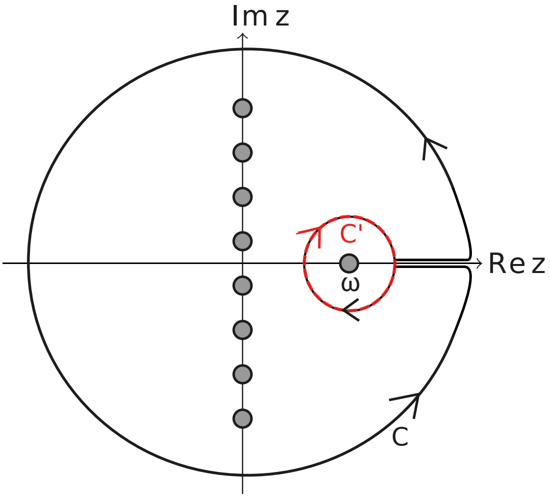

*Figure A.1.* Integration paths $C$ and $C'$, the Matsubara points and the pole of $g(z)$ at $z = \omega$.

# B. Lanczos algorithm

In this Appendix an overview of the Lanczos algorithm for calculating the XA spectrum is presented. For more detailed descriptions, please see Refs. [111, 180–183]. Our starting point is the Green's function in Eq. (3.20). We want to calculate the corresponding spectral function $\rho(\omega) = -\frac{1}{\pi}\mathrm{Im}G(\omega + i\delta)$, for a small positive $\delta$. The first thing is to find the eigenstates $|n\rangle$ and the corresponding eigenenergies $E_n$. In the Lanczos method eigenstates are obtained by the iterative construction of an orthonormal basis and the diagonalization of the Hamiltonian in this so called Krylov basis. Starting from a random normalized state $|v_0\rangle$, the Krylov basis $\{|v_0\rangle, |v_1\rangle, ..., |v_{m-1}\rangle\}$ is defined according to the initializations

$$\begin{aligned} |w'_0\rangle &= \hat{H}|v_0\rangle \\ \alpha_0 &= \langle w'_0|v_0\rangle \\ |w_0\rangle &= |w'_0\rangle - \alpha_0|v_0\rangle. \end{aligned} \tag{B.1}$$

and the recurrent relations:

$$\begin{aligned} \beta_{j-1} &= \sqrt{\langle w_{j-1}|w_{j-1}\rangle} \\ |v_j\rangle &= \frac{1}{\beta_{j-1}}|w_{j-1}\rangle \\ |w'_j\rangle &= \hat{H}|v_j\rangle \\ \alpha_j &= \langle w'_j|v_j\rangle \\ |w_j\rangle &= |w'_j\rangle - \alpha_j|v_j\rangle - \beta_{j-1}|v_{j-1}\rangle. \end{aligned} \tag{B.2}$$

The Hamiltonian in the Krylov basis is tridiagonal,

$$H_{\mathrm{krylov}} = \begin{bmatrix} \alpha_0 & \beta_0 & 0 & 0 & 0 \\ \beta_0 & \alpha_1 & \beta_1 & 0 & 0 \\ 0 & \beta_1 & \alpha_2 & \ddots & 0 \\ 0 & 0 & \ddots & \ddots & \beta_{m-2} \\ 0 & 0 & 0 & \beta_{m-2} & \alpha_{m-1} \end{bmatrix} \tag{B.3}$$

and diagonalizing it gives eigenstates and eigenenergies of the full Hamiltonian.

Once the eigenstates are found, for each eigenstate $|n\rangle$, we want to calculate

$$G^{(n)}(\omega + i\delta) = \langle n|\hat{T}^\dagger \frac{1}{\tilde{\omega}\hat{1} - \hat{H}}\hat{T}|n\rangle, \tag{B.4}$$

where $\tilde{\omega} = \omega + i\delta + E_n$ is introduced for compactness. Starting from the normalized state

$$|v_0\rangle = \frac{1}{\sqrt{\langle n|\hat{T}^\dagger \hat{T}|n\rangle}} \hat{T}|n\rangle \tag{B.5}$$

we construct the Krylov basis $\{|v_j\rangle\}$ of $\hat{H}$ according to Eq. (B.1) and Eq. (B.2), and formulate the Green's function as

$$G^{(n)}(\omega + i\delta) = \langle n|\hat{T}^\dagger \hat{T}|n\rangle \, \left(\tilde{\omega} I - H_{\text{krylov}}\right)^{-1}_{[0,0]}, \tag{B.6}$$

where $[0,0]$ simply are indices to the inverse matrix and $I$ is the identity matrix. Finally, the $[0,0]$ element of the inverse of the tridiagonal matrix in Eq. (B.6) is expressed as a continued fraction [184]

$$G^{(n)}(\omega + i\delta) = \langle n|\hat{T}^\dagger \hat{T}|n\rangle \, \cfrac{1}{\tilde{\omega} - \alpha_0 - \cfrac{\beta_0^2}{\tilde{\omega} - \alpha_1 - \cfrac{\beta_1^2}{\tilde{\omega} - \alpha_2 \cdots}}}. \tag{B.7}$$

In practice there are several things to consider. For finding the ground state, instead of using a relatively large Krylov basis, often it is faster to use a small Krylov basis and restart the Lanczos algorithm from the obtained ground state [183]. For a certain precision, how small the Krylov basis can be depends on the Hamiltonian and the operator $\hat{T}$ but typically it is much smaller than the size of the full Hamiltonian. To find the eigenenergies of interest, it might be necessary to subtract a constant to the Hamiltonian such that the eigenvalues are all negative [111]. Also note, The Lanczos algorithm is numerically unstable and therefor often requires additional orthogonalization steps. For computational reasons, sometimes, only certain occupation configurations are allowed. This approach is called the restricted active space configuration interaction [185]. An important further consideration in order to minimize the number of needed Slater determinants is which single-particle basis to use in the many body calculations. One strategy is to have orbitals which diagonalize the density matrix [111].

# References

[1] Gapminder Foundation. Gapminder: Unveiling the beauty of statistics for a fact based world view. `https://www.gapminder.org/`, 2018.

[2] Hans Rosling, Ola Rosling, and Anna Ronnlund. *Factfulness: Ten Reasons We're Wrong About the World - and Why Things Are Better Than You Think*. Sceptre, 2018.

[3] Robert Lucas. The industrial revolution. `https://web.archive.org/web/20071127032512/http://minneapolisfed.org/pubs/region/04-05/essay.cfm`, 2003.

[4] Martin Hilbert and Priscila López. The world's technological capacity to store, communicate, and compute information. *Science*, 332(6025):60–65, 2011.

[5] Jonathan Rauch. The new old economy: Oil, computers, and the reinvention of the earth. `https://www.theatlantic.com/past/docs/issues/2001/01/rauch.htm`, 2008.

[6] John Hemminger. Science for energy technology: Strengthening the link between basic research and industry. August 2010.

[7] Paul Alivisatos and Michelle Buchanan. Basic research needs for carbon capture: Beyond 2020. March 2010.

[8] Steven Pinker. *Enlightenment Now: The Case for Reason, Science, Humanism, and Progress*. Viking, 2018.

[9] P. Hohenberg and W. Kohn. Inhomogeneous electron gas. *Phys. Rev.*, 136:B864–B871, Nov 1964.

[10] W. Kohn and L. J. Sham. Self-consistent equations including exchange and correlation effects. *Phys. Rev.*, 140:A1133–A1138, Nov 1965.

[11] Jan M. Tomczak and Silke Biermann. Optical properties of correlated materials - or why intelligent windows may look dirty. *physica status solidi (b)*, 246(9):1996–2005.

[12] M. Born and R. Oppenheimer. Zur quantentheorie der molekeln. *Annalen der Physik*, 389(20):457–484, 1927.

[13] M. Troyer. Lecture notes in computational quantum physics, ETH Zurich, spring semester 2012. `http://edu.itp.phys.ethz.ch/fs08/cqp/cqp.pdf`.

[14] Robert Eder. *Multiplets in Transition Metal Ions*. Verlag des Forschungszentrum Julich, 2012.

[15] K. Held. Electronic structure calculations using dynamical mean field theory. *Adv. Phys. 56, 829*, 2007.

[16] Felix Bloch. Über die quantenmechanik der elektronen in kristallgittern. *Zeitschrift für Physik*, 52(7):555–600, 1929.

[17] Oscar Grånäs. *Theoretical Studies of Magnetism and Electron Correlation in Solids*. Diva Vetenskapliga Arkivet, Uppsala University, Uppsala, 2012.

[18] F. Duan and J. Guojun. *Introduction to Condensed Matter Physics, vol 1*. World Scientific Publishing Co. Pte. Ltd., 2005.

[19] J. P. Perdew and Alex Zunger. Self-interaction correction to density-functional approximations for many-electron systems. *Phys. Rev. B*, 23:5048–5079, May 1981.

[20] Richard Martin. *Electronic stucture: basic theory and practical methods*. Cambridge University Press, New York, 2004.

[21] Rspt - relativistic spin polarized toolkit. `http://www.physics.uu.se/research/materials-theory/ongoing-research/code-development/rspt-main/`.

[22] John Wills, Mebarek Alouani, Per Andersson, Anna Delin, Olle Eriksson, and Oleksiy Grechnyev. *Full-Potential Electronic Structure Method*. Springer, New York, 2010.

[23] O. K. Andersen and R. V. Kasowski. Electronic states as linear combinations of muffin-tin orbitals. *Phys. Rev. B*, 4:1064–1069, Aug 1971.

[24] Kurt Lejaeghere, Gustav Bihlmayer, Torbjörn Björkman, Peter Blaha, Stefan Blügel, Volker Blum, Damien Caliste, Ivano E. Castelli, Stewart J. Clark, Andrea Dal Corso, Stefano de Gironcoli, Thierry Deutsch, John Kay Dewhurst, Igor Di Marco, Claudia Draxl, Marcin Dułak, Olle Eriksson, José A. Flores-Livas, Kevin F. Garrity, Luigi Genovese, Paolo Giannozzi, Matteo Giantomassi, Stefan Goedecker, Xavier Gonze, Oscar Grånäs, E. K. U. Gross, Andris Gulans, François Gygi, D. R. Hamann, Phil J. Hasnip, N. A. W. Holzwarth, Diana Iuşan, Dominik B. Jochym, François Jollet, Daniel Jones, Georg Kresse, Klaus Koepernik, Emine Küçükbenli, Yaroslav O. Kvashnin, Inka L. M. Locht, Sven Lubeck, Martijn Marsman, Nicola Marzari, Ulrike Nitzsche, Lars Nordström, Taisuke Ozaki, Lorenzo Paulatto, Chris J. Pickard, Ward Poelmans, Matt I. J. Probert, Keith Refson, Manuel Richter, Gian-Marco Rignanese, Santanu Saha, Matthias Scheffler, Martin Schlipf, Karlheinz Schwarz, Sangeeta Sharma, Francesca Tavazza, Patrik Thunström, Alexandre Tkatchenko, Marc Torrent, David Vanderbilt, Michiel J. van Setten, Veronique Van Speybroeck, John M. Wills, Jonathan R. Yates, Guo-Xu Zhang, and Stefaan Cottenier. Reproducibility in density functional theory calculations of solids. *Science*, 351(6280), 2016.

[25] John Wills, Olle Eriksson, Mebarek Alouani, and D.L. Price. *Full-Potential Total Energy and Force Calculations*. In Electronic Structure and Physical Properties of Solids, volume 535 of Lecture Notes in Physics, pages 148-167. Springer, Berlin, Heidelberg, 1999.

[26] Torbjorn Bjorkman. *Magnetic and Structural Properties of f-electron Systems from First Principles Theory*. PhD thesis, Uppsala University, 2009.

[27] Igor Di Marco. *Correlation Effects in the Electronic Structure of Transition Metals and Their Compounds*. PhD thesis, Radboud University, Nijmegen, 2009.

[28] Inka Locht. *Theoretical methods for the electronic structure and magnetism of strongly correlated materials*. PhD thesis, Uppsala University, 2017.

[29] Samara Keshavarz. *Magnetism in Transition Metal Systems - Interplay between structure, dimensionality and electron correlation*. PhD thesis, Uppsala University, 2018.

[30] J. Hubbard. Electron correlations in narrow energy bands. *Proceedings of the Royal Society of London. Series A. Mathematical and Physical Sciences*, 276(1365):238–257, 1963.

[31] H. Strand. *Critical Properties of the Mott-Hubbard Metal-Insulator Transition*. Chalmers, Gothenburg, Sweden, 2011.

[32] P. Thalmeier and L. M. Falicov. Intra-atomic correlation energies in cubic metals with canonical *d* bands. *Phys. Rev. B*, 20:4637–4644, Dec 1979.

[33] F. Loez-aguilar and J. Costa-Quintana. Coulomb correlation effects in the spin polarized band structure of Eu2O2. *physica status solidi (b)*, 114(2):599–608, 1982.

[34] V. I. Anisimov and O. Gunnarsson. Density-functional calculation of effective coulomb interactions in metals. *Phys. Rev. B*, 43:7570–7574, Apr 1991.

[35] Vladimir I. Anisimov, Jan Zaanen, and Ole K. Andersen. Band theory and Mott insulators: Hubbard U instead of Stoner I. *Phys. Rev. B*, 44:943–954, Jul 1991.

[36] V. I. Anisimov, I. V. Solovyev, M. A. Korotin, M. T. Czyżyk, and G. A. Sawatzky. Density-functional theory and NiO photoemission spectra. *Phys. Rev. B*, 48:16929–16934, Dec 1993.

[37] I. V. Solovyev, P. H. Dederichs, and V. I. Anisimov. Corrected atomic limit in the local-density approximation and the electronic structure of d impurities in Rb. *Phys. Rev. B*, 50:16861–16871, Dec 1994.

[38] Vladimir I Anisimov, F Aryasetiawan, and A I Lichtenstein. First-principles calculations of the electronic structure and spectra of strongly correlated systems: the LDA + U method. *Journal of Physics: Condensed Matter*, 9(4):767, 1997.

[39] Walter Metzner and Dieter Vollhardt. Correlated lattice fermions in $d = \infty$ dimensions. *Phys. Rev. Lett.*, 62:324–327, Jan 1989.

[40] Antoine Georges and Gabriel Kotliar. Hubbard model in infinite dimensions. *Phys. Rev. B*, 45:6479–6483, Mar 1992.

[41] Antoine Georges, Gabriel Kotliar, Werner Krauth, and Marcelo J. Rozenberg. Dynamical mean-field theory of strongly correlated fermion systems and the limit of infinite dimensions. *Rev. Mod. Phys.*, 68:13–125, Jan 1996.

[42] G. Kotliar, S. Y. Savrasov, K. Haule, V. S. Oudovenko, O. Parcollet, and C. A. Marianetti. Electronic structure calculations with dynamical mean-field theory. *Rev. Mod. Phys.*, 78:865–951, Aug 2006.

[43] Gerald D. Mahan. *Many-Particle Physics*. Plenum, New York, N.Y., 2nd edition, 1993.

[44] W. John Negele and Henri Orland. *Quantum Many-Particle Systems*. Advanced Books Classics. Perseus Books, New York, N.Y., 1998.

[45] Henrik Bruus and Karsten Flensberg. *Many-body quantum theory in condensed matter physics*. Oxford university press, 2002.

[46] R. Mattuck. *A Guide to Feynman Diagrams in the Many-Body Problem*. Dover Science Books. Dover Publications, inc, New York, 1992.

[47] Gordon Baym and N. David Mermin. Determination of thermodynamic Green's functions. *Journal of Mathematical Physics*, 2(2):232–234, 1961.

[48] C. Titchmarsh. *The Theory of Functions*. Fundamental Theories of Physics. Oxford University Press, London, England, 1939.

[49] Andrea Damascelli, Zahid Hussain, and Zhi-Xun Shen. Angle-resolved photoemission studies of the cuprate superconductors. *Rev. Mod. Phys.*, 75:473–541, Apr 2003.

[50] G. Kotliar and D. Vollhardt. Strongly correlated materials: Insights from dynamical mean-field theory. *Physics Today*, 57(3):53–59, March 2004.

[51] J. Kolorenč, Alexander I. Poteryaev, and Alexander I. Lichtenstein. Valence-band satellite in ferromagnetic nickel: LDA+DMFT study with exact diagonalization. *Phys. Rev. B*, 85:235136, Jun 2012.

[52] I. Di Marco, J. Minár, S. Chadov, M. I. Katsnelson, H. Ebert, and A. I. Lichtenstein. Correlation effects in the total energy, the bulk modulus, and the lattice constant of a transition metal: Combined local-density approximation and dynamical mean-field theory applied to Ni and Mn. *Phys. Rev. B*, 79:115111, Mar 2009.

[53] Y. O. Kvashnin, O. Grånäs, I. Di Marco, M. I. Katsnelson, A. I. Lichtenstein, and O. Eriksson. Exchange parameters of strongly correlated materials: Extraction from spin-polarized density functional theory plus dynamical mean-field theory. *Phys. Rev. B*, 91:125133, Mar 2015.

[54] S. Keshavarz, Y. O. Kvashnin, I. Di Marco, A. Delin, M. I. Katsnelson, A. I. Lichtenstein, and O. Eriksson. Layer-resolved magnetic exchange interactions of surfaces of late $3d$ elements: Effects of electronic correlations. *Phys. Rev. B*, 92:165129, Oct 2015.

[55] Antoine Georges. Strongly correlated electron materials: Dynamical mean field theory and electronic structure. *AIP Conference Proceedings*, 715(1):3–74, 2004.

[56] Michał Karski, Carsten Raas, and Götz S. Uhrig. Single-particle dynamics in the vicinity of the Mott-Hubbard metal-to-insulator transition. *Phys. Rev. B*, 77:075116, Feb 2008.

[57] Michel Caffarel and Werner Krauth. Exact diagonalization approach to correlated fermions in infinite dimensions: Mott transition and superconductivity. *Phys. Rev. Lett.*, 72:1545–1548, Mar 1994.

[58] Mats Granath and Johan Schött. Signatures of coherent electronic quasiparticles in the paramagnetic Mott insulator. *Phys. Rev. B*, 90:235129, Dec 2014.

[59] F. M. F. de Groot, J. C. Fuggle, B. T. Thole, and G. A. Sawatzky. 2p x-ray absorption of 3d transition-metal compounds: An atomic multiplet description including the crystal field. *Phys. Rev. B*, 42:5459–5468, Sep 1990.

[60] F. Aryasetiawan, K. Karlsson, O. Jepsen, and U. Schönberger. Calculations of Hubbard $U$ from first-principles. *Phys. Rev. B*, 74:125106, Sep 2006.

[61] M. Karolak, G. Ulm, T. Wehling, V. Mazurenko, A. Poteryaev, and A. Lichtenstein. Double counting in LDA+DMFT - the example of NiO. *Journal of Electron Spectroscopy and Related Phenomena*, 181(1):11 – 15, 2010. Proceedings of International Workshop on Strong Correlations and Angle-Resolved Photoemission Spectroscopy 2009.

[62] Autumn School on Correlated Electrons, Julich (Germany), 15 Sep 2014 - 19 Sep 2014. *DMFT at 25: Infinite Dimensions*, volume 4 of *Modeling and Simulation*, Jülich, Sep 2014. Forschungszentrum Julich Zentralbibliothek, Verlag.

[63] M. T. Czyżyk and G. A. Sawatzky. Local-density functional and on-site correlations: The electronic structure of $La_2CuO_4$ and $LaCuO_3$. *Phys. Rev. B*, 49:14211–14228, May 1994.

[64] A. I. Liechtenstein, V. I. Anisimov, and J. Zaanen. Density-functional theory and strong interactions: Orbital ordering in Mott-Hubbard insulators. *Phys. Rev. B*, 52:R5467–R5470, Aug 1995.

[65] Kristjan Haule. Exact double counting in combining the dynamical mean field theory and the density functional theory. *Phys. Rev. Lett.*, 115:196403, Nov 2015.

[66] I. I. Mazin and V. I. Anisimov. Insulating gap in FeO: Correlations and covalency. *Phys. Rev. B*, 55:12822–12825, May 1997.

[67] Joseph Hugel and Mohamed Kamal. Electronic ground state of MnO, FeO, CoO and NiO within the LSDA + U approximation. *Solid State Communications*, 100(7):457 – 461, 1996.

[68] A. Schrön, C. Rödl, and F. Bechstedt. Crystalline and magnetic anisotropy of the $3d$-transition metal monoxides MnO, FeO, CoO, and NiO. *Phys. Rev. B*, 86:115134, Sep 2012.

[69] I. V. Solovyev, A. I. Liechtenstein, and K. Terakura. Is Hund's second rule responsible for the orbital magnetism in solids? *Phys. Rev. Lett.*, 80:5758–5761, Jun 1998.

[70] Samara Keshavarz Hedayati. *Magnetism in Transition Metal Systems: Interplay between structure, dimensionality and electron correlation*. PhD thesis, Uppsala University, 2018.

[71] Olle Eriksson, Anders Bergman, Lars Bergqvist, and Johan Hellsvik. *Atomistic Spin Dynamics*. Oxford University Press, Oxford, 2017.

[72] A.I. Liechtenstein, M.I. Katsnelson, V.P. Antropov, and V.A. Gubanov. Local spin density functional approach to the theory of exchange interactions in ferromagnetic metals and alloys. *Journal of Magnetism and Magnetic Materials*, 67(1):65 – 74, 1987.

[73] M. I. Katsnelson and A. I. Lichtenstein. First-principles calculations of magnetic interactions in correlated systems. *Phys. Rev. B*, 61:8906–8912, Apr 2000.

[74] S. V. Halilov, H. Eschrig, A. Y. Perlov, and P. M. Oppeneer. Adiabatic spin dynamics from spin-density-functional theory: Application to Fe, Co, and Ni. *Phys. Rev. B*, 58:293–302, Jul 1998.

[75] Hongjun Xiang, Changhoon Lee, Hyun-Joo Koo, Xingao Gong, and Myung-Hwan Whangbo. Magnetic properties and energy-mapping analysis. *Dalton Trans.*, 42:823–853, 2013.

[76] Samara Keshavarz, Johan Schött, Andrew J. Millis, and Yaroslav O. Kvashnin. Electronic structure, magnetism, and exchange integrals in transition-metal oxides: Role of the spin polarization of the functional in DFT+$U$ calculations. *Phys. Rev. B*, 97:184404, May 2018.

[77] Jinghua Guo. Electronic properties of hydrogen storage materials with photon-in/photon-out soft-x-ray spectroscopy. *Journal of Physics and Chemistry of Solids*, 69(9):2223 – 2226, 2008. Study of Matter Under Extreme Conditions 2007.

[78] Piter S. Miedema, Peter Ngene, Ad M. J. van der Eerden, Dimosthenis

Sokaras, Tsu-Chien Weng, Dennis Nordlund, Yuen S. Au, and Frank M. F. de Groot. In situ X-ray Raman spectroscopy study of the hydrogen sorption properties of lithium borohydride nanocomposites. *Phys. Chem. Chem. Phys.*, 16:22651–22658, 2014.

[79] Xiaosong Liu, Dongdong Wang, Gao Liu, Venkat Srinivasan, Zhi Liu, Zahid Hussain, and Wanli Yang. Distinct charge dynamics in battery electrodes revealed by in situ and operando soft x-ray spectroscopy. *Nature Communications*, 4:2568, 10 2013.

[80] Jacinto Sa. *High-Resolution XAS/XES: Analyzing Electronic Structures of Catalysts*. CRC Press, 2017.

[81] B. M. Weckhuysen. *In-situ Spectroscopy of Catalysts*. American Scientific Publishers, 2004.

[82] Grant Bunker. *Introduction to XAFS: A Practical Guide to X-ray Absorption Fine Structure Spectroscopy*. Cambridge University Press, 2010.

[83] John Fuggle and John Inglesfield. *Unoccupied Electronic States*. Springer-Verlag, 1992.

[84] Frank de Groot and Akio Kotani. *Core Level Spectroscopy of Solids*. CRS Press, 2008.

[85] Joachim Stohr. *NEXAFS Spectroscopy*. Springer Series in Surface Sciences 25, 1996.

[86] Pedro F. Tavares, Simon C. Leemann, Magnus Sjostrom, and Ake Andersson. The MAX IV storage ring project. *Journal of Synchrotron Radiation*, 21:862–877, 2014.

[87] Frank de Groot. Multiplet effects in x-ray spectroscopy. *Coordination Chemistry Reviews*, 249(1):31 – 63, 2005. Synchrotron Radiation in Inorganic and Bioinorganic Chemistry.

[88] A. Beer. *Annalen der Physik und Chemie*, 86:78–88, 1852.

[89] Luuk J. P. Ament, Michel van Veenendaal, Thomas P. Devereaux, John P. Hill, and Jeroen van den Brink. Resonant inelastic x-ray scattering studies of elementary excitations. *Rev. Mod. Phys.*, 83:705–767, Jun 2011.

[90] V. Chakarian and Y. U. Idzerda. Total electron yield method in x-ray absorption spectroscopy: A closer look at the saturation/self-absorption effects (abstract). *Journal of Applied Physics*, 81(8):4709–4709, 1997.

[91] K. Fauth. How well does total electron yield measure x-ray absorption in nanoparticles? *Applied Physics Letters*, 85(15):3271–3273, 2004.

[92] V. J. Keast, A. J. Scott, R. Brydson, D. B. Williams, and J. Bruley. Electron energy-loss near-edge structure - a tool for the investigation of electronic structure on the nanometre scale. *Journal of Microscopy*, 203(2):135–175.

[93] Zechao Wang, Amir H. Tavabi, Lei Jin, Ján Rusz, Dmitry Tyutyunnikov, Hanbo Jiang, Yutaka Moritomo, Joachim Mayer, Rafal E. Dunin-Borkowski, Rong Yu, Jing Zhu, and Xiaoyan Zhong. Atomic scale imaging of magnetic circular dichroism by achromatic electron microscopy. *Nature Materials*, 17(3):221–225, 2018.

[94] B. T. Thole, P. Carra, F. Sette, and G. van der Laan. X-ray circular dichroism as a probe of orbital magnetization. *Phys. Rev. Lett.*, 68:1943–1946, Mar 1992.

[95] Paolo Carra, B. T. Thole, Massimo Altarelli, and Xindong Wang. X-ray circular dichroism and local magnetic fields. *Phys. Rev. Lett.*, 70:694–697, Feb

1993.

[96] W. Kohn. Nobel lecture: Electronic structure of matter—wave functions and density functionals. *Rev. Mod. Phys.*, 71:1253–1266, Oct 1999.

[97] Robert Duane Cowan. *The Theory of Atomic Structure and Spectra*. University of California Press, 1981.

[98] J. Schwitalla and H. Ebert. Electron core-hole interaction in the x-ray absorption spectroscopy of 3*d* transition metals. *Phys. Rev. Lett.*, 80:4586–4589, May 1998.

[99] A. L. Ankudinov, A. I. Nesvizhskii, and J. J. Rehr. Dynamic screening effects in x-ray absorption spectra. *Phys. Rev. B*, 67:115120, Mar 2003.

[100] A. I. Nesvizhskii and J. J. Rehr. *L*-edge XANES of 3*d*-transition metals. *Journal of Synchrotron Radiation*, 6(3):315–316, May 1999.

[101] C. J. Ballhausen. *Introduction to Ligand Field Theory*. McGraw-Hill, New York, 1962.

[102] Robert Laskowski and Peter Blaha. Understanding the $L_{2,3}$ x-ray absorption spectra of early 3*d* transition elements. *Phys. Rev. B*, 82:205104, Nov 2010.

[103] J. Vinson, J. J. Rehr, J. J. Kas, and E. L. Shirley. Bethe-Salpeter equation calculations of core excitation spectra. *Phys. Rev. B*, 83:115106, Mar 2011.

[104] Hidekazu Ikeno, Frank M F de Groot, Eli Stavitski, and Isao Tanaka. Multiplet calculations of L 2,3 x-ray absorption near-edge structures for 3d transition-metal compounds. *Journal of Physics: Condensed Matter*, 21(10):104208, 2009.

[105] O. Šipr, J. Minár, A. Scherz, H. Wende, and H. Ebert. Many-body effects in x-ray absorption and magnetic circular dichroism spectra within the LSDA+DMFT framework. *Phys. Rev. B*, 84:115102, Sep 2011.

[106] Atsushi Hariki, Takayuki Uozumi, and Jan Kuneš. LDA+DMFT approach to core-level spectroscopy: Application to 3*d* transition metal compounds. *Phys. Rev. B*, 96:045111, Jul 2017.

[107] Atsushi Hariki, Mathias Winder, and Jan Kuneš. Continuum charge excitations in high-valence transition-metal oxides revealed by resonant inelastic x-ray scattering. *Phys. Rev. Lett.*, 121:126403, Sep 2018.

[108] M. W. Haverkort, M. Zwierzycki, and O. K. Andersen. Multiplet ligand-field theory using Wannier orbitals. *Phys. Rev. B*, 85:165113, Apr 2012.

[109] Nanna Holmgaard List, Joanna Kauczor, Trond Saue, Hans Jorgen Aagaard Jensen, and Patrick Norman. Beyond the electric-dipole approximation: A formulation and implementation of molecular response theory for the description of absorption of electromagnetic field radiation. *The Journal of Chemical Physics*, 142(24):244111, 2015.

[110] Anant Dixit and M. Alouani. Ab initio calculations of x-ray magnetic circular dichroism spectra within the projector augmented wave method: An implementation into the VASP code. *Computer Physics Communications*, 207:136 – 144, 2016.

[111] Y. Lu, M. Höppner, O. Gunnarsson, and M. W. Haverkort. Efficient real-frequency solver for dynamical mean-field theory. *Phys. Rev. B*, 90:085102, Aug 2014.

[112] Johann Lüder, Johan Schött, Barbara Brena, Maurits W. Haverkort, Patrik Thunström, Olle Eriksson, Biplab Sanyal, Igor Di Marco, and Yaroslav O.

Kvashnin. Theory of $L$-edge spectroscopy of strongly correlated systems. *Phys. Rev. B*, 96:245131, Dec 2017.

[113] Patrik Thunström, Igor Di Marco, and Olle Eriksson. Electronic entanglement in late transition metal oxides. *Phys. Rev. Lett.*, 109:186401, Oct 2012.

[114] A. E. Bocquet, T. Mizokawa, K. Morikawa, A. Fujimori, S. R. Barman, K. Maiti, D. D. Sarma, Y. Tokura, and M. Onoda. Electronic structure of early 3d-transition-metal oxides by analysis of the 2p core-level photoemission spectra. *Phys. Rev. B*, 53:1161–1170, Jan 1996.

[115] J. Zaanen, G. A. Sawatzky, and J. W. Allen. Band gaps and electronic structure of transition-metal compounds. *Phys. Rev. Lett.*, 55:418–421, Jul 1985.

[116] P. Novák, K. Knížek, and J. Kuneš. Crystal field parameters with Wannier functions: Application to rare-earth aluminates. *Phys. Rev. B*, 87:205139, May 2013.

[117] Maurits W. Haverkort. Quanty for core level spectroscopy - excitons, resonances and band excitations in time and frequency domain. *Journal of Physics: Conference Series*, 712(1):012001, 2016.

[118] M. Haverkort. Quanty - a quantum many body script language. `http://www.quanty.org/`, 2017.

[119] Impurity model. `https://github.com/JohanSchott/impurityModel`. Accessed: 2018-10-10.

[120] John B. Goodenough. Spin-orbit-coupling effects in transition-metal compounds. *Phys. Rev.*, 171:466–479, Jul 1968.

[121] T. Haupricht, R. Sutarto, M. W. Haverkort, H. Ott, A. Tanaka, H. H. Hsieh, H.-J. Lin, C. T. Chen, Z. Hu, and L. H. Tjeng. Local electronic structure of $Fe^{2+}$ impurities in MgO thin films: Temperature-dependent soft x-ray absorption spectroscopy study. *Phys. Rev. B*, 82:035120, Jul 2010.

[122] Maurits Haverkort. *Spin and orbital degrees of freedom in transition metal oxides and oxide thin films studied by soft x-ray absorption spectroscopy*. PhD thesis, Universität zu Köln, 2005.

[123] B. Gilbert, B. H. Frazer, A. Belz, P. G. Conrad, K. H. Nealson, D. Haskel, J. C. Lang, G. Srajer, and G. De Stasio. Multiple scattering calculations of bonding and x-ray absorption spectroscopy of manganese oxides. *The Journal of Physical Chemistry A*, 107(16):2839–2847, 2003.

[124] T. J. Regan, H. Ohldag, C. Stamm, F. Nolting, J. Lüning, J. Stöhr, and R. L. White. Chemical effects at metal/oxide interfaces studied by x-ray-absorption spectroscopy. *Phys. Rev. B*, 64:214422, Nov 2001.

[125] F M F de Groot, M Abbate, J van Elp, G A Sawatzky, Y J Ma, C T Chen, and F Sette. Oxygen 1s and cobalt 2p x-ray absorption of cobalt oxides. *Journal of Physics: Condensed Matter*, 5(14):2277, 1993.

[126] D. Alders, L. H. Tjeng, F. C. Voogt, T. Hibma, G. A. Sawatzky, C. T. Chen, J. Vogel, M. Sacchi, and S. Iacobucci. Temperature and thickness dependence of magnetic moments in NiO epitaxial films. *Phys. Rev. B*, 57:11623–11631, May 1998.

[127] Ján Rusz, Somnath Bhowmick, Mattias Eriksson, and Nikolaj Karlsson. Scattering of electron vortex beams on a magnetic crystal: Towards atomic-resolution magnetic measurements. *Phys. Rev. B*, 89:134428, Apr 2014.

[128] Zhong et al. Achromatic atomic-plane resolved electron energy-loss spectroscopy at oxide interfaces. Ongoing project with preliminary experimental results.

[129] P. A. van Aken and B. Liebscher. Quantification of ferrous/ferric ratios in minerals: new evaluation schemes of Fe $L_{2,3}$ electron energy-loss near-edge spectra. *Physics and Chemistry of Minerals*, 29(3):188–200, Apr 2002.

[130] Peter Staar, Bart Ydens, Anton Kozhevnikov, Jean-Pierre Locquet, and Thomas Schulthess. Continuous-pole-expansion method to obtain spectra of electronic lattice models. *Phys. Rev. B*, 89:245114, Jun 2014.

[131] Abdul-Majid Wazwaz. *Linear and Nonlinear Integral Equations*. Springer Science and Business Media, Heidelberg, Dordrecht, London, New York, 2011.

[132] Rainer Kress. *Linear Integral equations*, volume 82. Springer Verlag, Berlin Heidelberg, 1989.

[133] Khaldoon Ghanem. Stochastic mode sampling (SMS) – an efficient approach to the analytic continuation problem. Ms, RWTH Aachen, 2013. RWTH Aachen, Masterarbeit, 2013.

[134] Andreas Dirks, Philipp Werner, Mark Jarrell, and Thomas Pruschke. Continuous-time quantum Monte Carlo and maximum entropy approach to an imaginary-time formulation of strongly correlated steady-state transport. *Phys. Rev. E*, 82:026701, Aug 2010.

[135] Olivier Parcollet, Michel Ferrero, Thomas Ayral, Hartmut Hafermann, Igor Krivenko, Laura Messio, and Priyanka Seth. TRIQS: A toolbox for research on interacting quantum systems. *Computer Physics Communications*, 196:398 – 415, 2015.

[136] Lewin Boehnke, Hartmut Hafermann, Michel Ferrero, Frank Lechermann, and Olivier Parcollet. Orthogonal polynomial representation of imaginary-time Green's functions. *Phys. Rev. B*, 84:075145, Aug 2011.

[137] O. Gunnarsson, M. W. Haverkort, and G. Sangiovanni. Analytical continuation of imaginary axis data using maximum entropy. *Phys. Rev. B*, 81:155107, 2010.

[138] Kendall E. Atkinson. *An introduction to Numerical Analysis*. John Wiley & Sons, New York, 1989.

[139] G. Dahlquist and Åke Börck. *Numerical Methods in Scientific Computing, Volume I.* Society for Industrial and Applied Mathematics, 2008.

[140] C. L. Lawson and R. J. Hanson. *Solving Least Squares Problems*. Society for Industrial and Applied Mathematics Philadelphia, Philadelphia, 1995.

[141] E. Anderson, Z. Bai, C. Bischof, S. Blackford, J. Demmel, J. Dongarra, J. Du Croz, A. Greenbaum, S. Hammarling, A. McKenney, and D. Sorensen. *LAPACK Users' Guide*. Society for Industrial and Applied Mathematics, Philadelphia, PA, third edition, 1999.

[142] Carlos Beltran. Estimates on the condition number of random rank-deficient matrices. *Journal of Numerical Analysis*, 31, 2011.

[143] Andreï Nikolaevitch Tikhonov. *Numerical methods for the solution of ill-posed problems*. Mathematics and its applications. Kluwer Academic Publishers, Dordrecht, Boston, 1995.

[144] P. C. Hansen. The L-curve and its use in the numerical treatment of inverse

problems. In *in Computational Inverse Problems in Electrocardiology, ed. P. Johnston, Advances in Computational Bioengineering*, pages 119–142. WIT Press, 2000.

[145] John Skilling. *Maximum Entropy and Bayesian Methods*, volume 36 of *Fundamental Theories of Physics*. Springer, 1988.

[146] R. N. Silver, D. S. Sivia, and J. E. Gubernatis. Maximum-entropy method for analytic continuation of quantum Monte Carlo data. *Phys. Rev. B*, 41:2380–2389, Feb 1990.

[147] Mark Jarrell and J.E. Gubernatis. Bayesian inference and the analytic continuation of imaginary-time quantum Monte Carlo data. *Physics Reports*, 269(3):133 – 195, 1996.

[148] R. K. Bryan. Maximum entropy analysis of oversampled data problems. *European Biophysics Journal*, 18(3):165–174, 1990.

[149] J. E. Gubernatis, Mark Jarrell, R. N. Silver, and D. S. Sivia. Quantum Monte Carlo simulations and maximum entropy: Dynamics from imaginary-time data. *Phys. Rev. B*, 44:6011–6029, Sep 1991.

[150] Sebastian Fuchs, Thomas Pruschke, and Mark Jarrell. Analytic continuation of quantum Monte Carlo data by stochastic analytical inference. *Phys. Rev. E*, 81:056701, May 2010.

[151] Eva Pavarini, Erik Koch, Frithjof Anders, and Mark (Eds. ) Jarrell. *Correlated electrons: from models to materials*, volume 2 of *Schriften des Forschungszentrums Julich. Reihe Modeling and simulation*. Forschungszentrum Julich GmbH, Julich, 2012. Record converted from JUWEL: 18.07.2013.

[152] C. Raas and S. G. Uhrig. Spectral densities from dynamic density-matrix renormalization. *The European Physical Journal B - Condensed Matter and Complex Systems*, 45(3):293–303, 2005.

[153] Johan Schött. Analytic continuation of electronic Green's functions from imaginary to real time using maximum entropy. `http://publications.lib.chalmers.se/records/fulltext/211758/211758.pdf`, 2014.

[154] A. S. Mishchenko, N. V. Prokof'ev, A. Sakamoto, and B. V. Svistunov. Diagrammatic quantum Monte Carlo study of the Fröhlich polaron. *Phys. Rev. B*, 62:6317–6336, Sep 2000.

[155] Anders W. Sandvik. Stochastic method for analytic continuation of quantum Monte Carlo data. *Phys. Rev. B*, 57:10287–10290, 1998.

[156] K. S. D. Beach. Identifying the maximum entropy method as a special limit of stochastic analytic continuation. *eprint arXiv:cond-mat/0403055*, March 2004.

[157] Johan Nordström, Johan Schött, Inka L.M. Locht, and Igor Di Marco. A GPU code for analytic continuation through a sampling method. *SoftwareX*, 5:178 – 182, 2016.

[158] Johan Nordström. GPU parallelization of the Mishchenko method for solving fredholm equations of the first kind. `http://www.diva-portal.org/smash/get/diva2:819483/FULLTEXT01.pdf`, 2015.

[159] G. A. Baker. *Essentials of Padé Approximants*. Academic Press, New York, 1975.

[160] George A. Baker and Peter Graves-Morris. *Padé Approximants*. Cambridge

University Press, second edition, 1996. Cambridge Books Online.

[161] K. S. D. Beach, R. J. Gooding, and F. Marsiglio. Reliable Padé analytical continuation method based on a high-accuracy symbolic computation algorithm. *Phys. Rev. B*, 61:5147–5157, Feb 2000.

[162] H. J. Vidberg and J. W. Serene. Solving the Eliashberg equations by means of N-point Padé approximants. *J. Low Temp. Phys.*, 29:179–192, 1977.

[163] Andreas Östlin. *Electronic structure studies and method development for complex materials*. PhD thesis, KTH, Applied Material Physics, 2015.

[164] Ž. Osolin and R. Žitko. Padé approximant approach for obtaining finite-temperature spectral functions of quantum impurity models using the numerical renormalization group technique. *Phys. Rev. B*, 87:245135, Jun 2013.

[165] A. Östlin, L. Chioncel, and L. Vitos. One-particle spectral function and analytic continuation for many-body implementation in the exact muffin-tin orbitals method. *Phys. Rev. B*, 86:235107, Dec 2012.

[166] D. Sokolovski, E. Akhmatskaya, and S. K. Sen. Extracting S-matrix poles for resonances from numerical scattering data: Type-II Padé reconstruction. *Computer Physics Communications*, 182:448–466, February 2011.

[167] Johan Schött, Inka L. M. Locht, Elin Lundin, Oscar Grånäs, Olle Eriksson, and Igor Di Marco. Analytic continuation by averaging Padé approximants. *Phys. Rev. B*, 93:075104, Feb 2016.

[168] O. Gunnarsson, M. W. Haverkort, and G. Sangiovanni. Analytical continuation of imaginary axis data for optical conductivity. *Phys. Rev. B*, 82:165125, 2010.

[169] M. Nakata. The MPACK (MBLAS/MLAPACK): A multiple precision arithmetic version of BLAS and LAPACK. `http://mplapack.sourceforge.net`.

[170] J. Schött, E. G. C. P. van Loon, I. L. M. Locht, M. I. Katsnelson, and I. Di Marco. Comparison between methods of analytical continuation for bosonic functions. *Phys. Rev. B*, 94:245140, Dec 2016.

[171] Manuel Guidon. Thesis, ETH Zurich. `https://www2.math.ethz.ch/rw/alumni/thesis/Guidon_Manuel_Diplomarbeit.pdf`.

[172] Guntram Fischer, Markus Däne, Arthur Ernst, Patrick Bruno, Martin Lüders, Zdzislawa Szotek, Walter Temmerman, and Wolfram Hergert. Exchange coupling in transition metal monoxides: Electronic structure calculations. *Phys. Rev. B*, 80:014408, Jul 2009.

[173] Adam Jacobsson, Biplab Sanyal, Marjana Ležaić, and Stefan Blügel. Exchange parameters and adiabatic magnon energies from spin-spiral calculations. *Phys. Rev. B*, 88:134427, Oct 2013.

[174] I. V. Solovyev and K. Terakura. Effective single-particle potentials for MnO in light of interatomic magnetic interactions: Existing theories and perspectives. *Phys. Rev. B*, 58:15496–15507, Dec 1998.

[175] R Logemann, A N Rudenko, M I Katsnelson, and A Kirilyuk. Exchange interactions in transition metal oxides: the role of oxygen spin polarization. *Journal of Physics: Condensed Matter*, 29(33):335801, 2017.

[176] L. Chioncel, L. Vitos, I. A. Abrikosov, J. Kollár, M. I. Katsnelson, and A. I. Lichtenstein. *Ab initio* electronic structure calculations of correlated systems: An EMTO-DMFT approach. *Phys. Rev. B*, 67:235106, Jun 2003.

[177] J. Minár, L. Chioncel, A. Perlov, H. Ebert, M. I. Katsnelson, and A. I. Lichtenstein. Multiple-scattering formalism for correlated systems: A KKR-DMFT approach. *Phys. Rev. B*, 72:045125, Jul 2005.

[178] W. Pfaff, B. Hensen, H. Bernien, S. B. van Dam, M. S. Blok, T. H. Taminiau, M. J. Tiggelman, R. N. Schouten, M. Markham, D. J. Twitchen, and R. Hanson. Unconditional quantum teleportation between distant solid-state quantum bits. *Science*, 2014.

[179] China's 'artificial sun' sets world record with 100 second steady-state high performance plasma. `https://phys.org/news/2017-07-china-artificial-sun-world-steady-state.html`. Accessed: 2018-10-09.

[180] C. Lanczos. An iteration method for the solution of the eigenvalue problem of linear differential and integral operators. *Journal of Research of the National Bureau of Standards*, 45, Oct 1950.

[181] J. Jaklič and P. Prelovšek. Lanczos method for the calculation of finite-temperature quantities in correlated systems. *Phys. Rev. B*, 49:5065–5068, Feb 1994.

[182] Alexander Weiße, Gerhard Wellein, Andreas Alvermann, and Holger Fehske. The kernel polynomial method. *Rev. Mod. Phys.*, 78:275–306, Mar 2006.

[183] R. Lehoucq, D. Sorensen, and C. Yang. *ARPACK Users' Guide*. Society for Industrial and Applied Mathematics, 1998.

[184] Paolo Giannozzi, Giuseppe Grosso, Saverio Moroni, and Giuseppe Pastori Parravicini. The ordinary and matrix continued fractions in the theoretical analysis of hermitian and relaxation operators. *Applied Numerical Mathematics*, 4(2):273 – 295, 1988.

[185] Jeppe Olsen, Björn O. Roos, Poul Jorgensen, and Hans Jorgen Jensen. Determinant based configuration interaction algorithms for complete and restricted configuration interaction spaces. *The Journal of Chemical Physics*, 89(4):2185–2192, 1988.

[186] Xin Wang, Emanuel Gull, Luca de' Medici, Massimo Capone, and Andrew J. Millis. Antiferromagnetism and the gap of a Mott insulator: Results from analytic continuation of the self-energy. *Phys. Rev. B*, 80:045101, Jul 2009.

[187] C. E. Creffield, E. G. Klepfish, E. R. Pike, and Sarben Sarkar. Spectral weight function for the half-filled Hubbard model: A singular value decomposition approach. *Phys. Rev. Lett.*, 75:517–520, Jul 1995.

[188] E.T. Jaynes. *The Maximum Entropy Formalism*. MIT Press, Cambridge, 1978.

[189] Jr. Grandy C.R. Smith. *Maximum Entropy and Bayesian Methods in Inverse Problems*, volume 14 of *Fundamental Theories of Physics*. Springer, 1985.

[190] I. S. Krivenko and A. N. Rubtsov. Analytic continuation of quantum Monte Carlo data: Optimal stochastic regularization approach. *eprint arXiv:cond-mat/0612233*, December 2006.

[191] K. Vafayi and O. Gunnarsson. Analytical continuation of spectral data from imaginary time axis to real frequency axis using statistical sampling. *Phys. Rev. B*, 76:035115, Jul 2007.

[192] H. S. Wall. *Analytic Theory of Continued Fractions*. AMS Chelsea Publishing, New York, 1948.

[193] H. S. Wall and M. Wetzel. Contributions to the analytic theory of J-fractions.

*Trans. Am. Math. Soc.*, 55, 1944.

[194] Ansgar Liebsch and Hiroshi Ishida. Temperature and bath size in exact diagonalization dynamical mean field theory. *Journal of Physics: Condensed Matter*, 24(5):053201, 2012.

[195] P. Brouwer. Lecture notes from course: Theory of many-particle systems, page654, Cornell University, 2005.

[196] P. Fazekas. *Lecture Notes on Electron Correlation and Magnetism*. World Scientific Publishing Co. Pte. Ltd., 1999.

[197] F Aryasetiawan and O Gunnarsson. The GW method. *Reports on Progress in Physics*, 61(3):237, 1998.

[198] P. W. Anderson. Localized magnetic states in metals. *Phys. Rev.*, 124:41–53, Oct 1961.

[199] N. F. Mott. The basis of the electron theory of metals, with special reference to the transition metals. *Proceedings of the Physical Society. Section A*, 62(7):416, 1949.

[200] A I Liechtenstein, M I Katsnelson, and V A Gubanov. Exchange interactions and spin-wave stiffness in ferromagnetic metals. *Journal of Physics F: Metal Physics*, 14(7):L125, 1984.

[201] Emanuel Gull, David R. Reichman, and Andrew J. Millis. Bold-line diagrammatic Monte Carlo method: General formulation and application to expansion around the noncrossing approximation. *Phys. Rev. B*, 82:075109, Aug 2010.

[202] N. Blümer. Numerically exact Green's functions from Hirsch-Fye quantum Monte Carlo simulations. arXiv:0712.1290, 2007.

[203] Emanuel Gull, Andrew J. Millis, Alexander I. Lichtenstein, Alexey N. Rubtsov, Matthias Troyer, and Philipp Werner. Continuous-time Monte Carlo methods for quantum impurity models. *Rev. Mod. Phys.*, 83:349–404, 2011.

[204] P. Thunström, I. Di Marco, A. Grechnev, S. Lebègue, M. I. Katsnelson, A. Svane, and O. Eriksson. Multiplet effects in the electronic structure of intermediate-valence compounds. *Phys. Rev. B*, 79:165104, Apr 2009.

[205] Mats Granath and Hugo U. R. Strand. Distributional exact diagonalization formalism for quantum impurity models. *Phys. Rev. B*, 86:115111, Sep 2012.

[206] V. V. Mazurenko and V. I. Anisimov. Weak ferromagnetism in antiferromagnets: $\alpha-\mathrm{Fe_2O_3}$ and $\mathrm{La_2CuO_4}$. *Phys. Rev. B*, 71:184434, May 2005.

[207] Patrik Fazekas. *Electron Correlation and Magnetism*. World Scientific Publishing Co. Pte. Ltd., Singapore, 1999.

[208] F. D. M. Haldane. Model for a quantum hall effect without landau levels: Condensed-matter realization of the "parity anomaly". *Phys. Rev. Lett.*, 61:2015–2018, Oct 1988.

[209] G.H. Jonker and J.H. Van Santen. Ferromagnetic compounds of manganese with perovskite structure. *Physica*, 16(3):337 – 349, 1950.

[210] J.G. Bednorz and K.A. Müller. Possible high-Tc superconductivity in the Ba-La-Cu-O system. *Zeitschrift für Physik B Condensed Matter*, 64(2):189–193, 1986.

[211] Alexei Grechnev, I. Di Marco, M. I. Katsnelson, A. I. Lichtenstein, John Wills, and Olle Eriksson. Theory of bulk and surface quasiparticle spectra for Fe, Co,

and Ni. *Phys. Rev. B*, 76(3):035107, 2007.

[212] O. Grånäs, I. Di Marco, P. Thunström, L. Nordström, O. Eriksson, T. Björkman, and J.M. Wills. Charge self-consistent dynamical mean-field theory based on the full-potential linear muffin-tin orbital method: Methodology and applications. *Computational Materials Science*, 55(0):295 – 302, 2012.

[213] Philipp Werner, Armin Comanac, Luca de' Medici, Matthias Troyer, and Andrew J. Millis. Continuous-time solver for quantum impurity models. *Phys. Rev. Lett.*, 97:076405, Aug 2006.

[214] Philipp Werner and Andrew J. Millis. Hybridization expansion impurity solver: General formulation and application to kondo lattice and two-orbital models. *Phys. Rev. B*, 74:155107, Oct 2006.

[215] A. Papoulis. *Probability and Statistics*. Prentice-Hall, New York, 1990.

[216] C. Johnson R. Horn. *Matrix Analysis*. Cambridge University Press, 1985.

[217] S. Hufner. *Photoelectron Spectroscopy*. Springer, Berlin, 2003.

[218] P. Goodman and A. F. Moodie. Numerical evaluations of *N*-beam wave functions in electron scattering by the multi-slice method. *Acta Crystallographica Section A*, 30(2):280–290, Mar 1974.

# Acta Universitatis Upsaliensis

*Digital Comprehensive Summaries of Uppsala Dissertations from the Faculty of Science and Technology* 1729

Editor: The Dean of the Faculty of Science and Technology

A doctoral dissertation from the Faculty of Science and Technology, Uppsala University, is usually a summary of a number of papers. A few copies of the complete dissertation are kept at major Swedish research libraries, while the summary alone is distributed internationally through the series Digital Comprehensive Summaries of Uppsala Dissertations from the Faculty of Science and Technology. (Prior to January, 2005, the series was published under the title “Comprehensive Summaries of Uppsala Dissertations from the Faculty of Science and Technology”.)

Distribution: publications.uu.se
urn:nbn:se:uu:diva-362834

ACTA
UNIVERSITATIS
UPSALIENSIS
UPPSALA
2018